KFKI-2003-01/G
REPORT

Z. HÓZER,
I. NAGY,
P. WINDBERG,
M. BALASKÓ,
L. MATUS,
O. PROKOPIEV,
A. PINTÉR,
M. HORVÁTH,
GY. GYENES,
A. CZITROVSZKY,
A. NAGY,
P. JANI

CODEX-B4C EXPERIMENT:
CORE DEGRADATION TEST WITH BORON CARBIDE CONTROL ROD

Hungarian Academy of Sciences
CENTRAL
RESEARCH
INSTITUTE FOR
PHYSICS

BUDAPEST

CODEX-B4C EXPERIMENT:
CORE DEGRADATION TEST WITH BORON CARBIDE CONTROL ROD

Zoltán Hózer, Imre Nagy, Péter Windberg,
Márton Balaskó, Lajos Matus, Oleg Prokopiev,
Anna Pintér, Márta Horváth, György Gyenes

KFKI Atomic Energy Research Institute
H-1525 Budapest, P.O.Box 49, Hungary
Hozer@sunserv.kfki.hu

Aladár Czitrovszky, Attila Nagy, Péter Jani
Research Institute for Solid State Physics and Optics
H-1525 Budapest, P.O.Box 49, Hungary

ABSTRACT

Z. Hózer, I. Nagy, P. Windberg, M. Balaskó, L. Matus, O. Prokopiev, A. Pintér, M. Horváth, Gy. Gyenes, A. Czitrovszky, A. Nagy, P. Jani : CODEX-B4C EXPERIMENT: CORE DEGRADATION TEST WITH BORON CARBIDE CONTROL ROD

The CODEX-B4C bundle test has been successfully performed on 25th May 2001 in the framework of the COLOSS project of the EU 5th FWP. The high temperature degradation of a VVER-1000 type bundle with B_4C control rod was investigated with electrically heated fuel rods. The experiment was carried out according to a scenario selected in favour of methane formation. Degradation of control rod and fuel bundle took place at temperatures ~2000 °C, cooling down of the bundle was performed in steam atmosphere. The gas composition measurement indicated no methane production during the experiment. High release of aerosols was detected in the high temperature oxidation phase. The on-line measured data are collected into a database and are available for code validation and development.

KIVONAT

Hózer Z., Nagy I., Windberg P., Balaskó M., Matus L., Prokopiev O., Pintér A., Horváth M., Gyenes Gy., Czitrovszky A., Nagy A., Jani P.: A CODEX-B4C KÍSÉRLET: ZÓNASÉRÜLÉSES MÉRÉS BÓR-KARBID SZABÁLYOZÓ RÚDDAL

A CODEX-B4C kísérletet 2001 május 25-én hajtottuk végre az Európai Unió 5-ös Keretprogramjának COLOSS propjektjében. B_4C szabályozórúddal ellátott VVER-1000 típusú köteg magas hőmérsékletű tönkremenetelét vizsgáltuk elektromosan fűtött fűtőelem rudakkal. A méréshez olyan körülményeket választottunk ki, amik elősegíthették a metán képződést. A kísérlet során ~2000 °C hőmérsékletet értünk el, és ez a szabályozó rúd és a fűtőelem rudak sérülését idézte elő. A gázösszetétel mérés nem mutatott metánképződést. A kísérlet magas hőméréskletű oxidációs szakaszában intenzív aeroszol kibocsátást tapasztaltunk. A mért adatokból elektronikus adatbázist hoztunk létre, ami felhasználható kód validációs és modellfejlesztési célokra.

Contents

1. INTRODUCTION **8**

2. THE CODEX FACILITY **9**

3. THE CODEX EXPERIMENTAL PROGRAMME **13**

4. THE CODEX-B4C COMMISSIONING TEST **13**

5. THE CODEX-B4C TEST **14**

6. EXPERIMENTAL RESULTS **16**

7. EXPERIMENTAL DATABASE **17**

8. EXAMINATION OF BUNDLE **20**

- 8.1 RADIOGRAPHY 20
- 8.2 BUNDLE CROSS SECTIONS 21
  - *8.2.1 Elevation 50 mm 21*
  - *8.2.2 Elevation 75 mm 21*
  - *8.2.3 Elevation 100 mm 22*
  - *8.2.4 Elevation 125 mm 22*
  - *8.2.5 Elevation 150 mm 22*
  - *8.2.6 Elevation 175 mm 22*
  - *8.2.7 Elevation 200 mm 23*
  - *8.2.8 Elevation 235 mm 23*
  - *8.2.9 Elevation 335 mm 23*
  - *8.2.10 Elevation 410 mm 24*
  - *8.2.11 Elevation 460 mm 24*
  - *8.2.12 Elevation 535 mm 24*
  - *8.2.13 Elevation 555 mm 25*
- 8.3 OXIDE LAYER THICKNESS MEASUREMENTS 25
- 8.4 CONTROL ROD MELT INVESTIGATION 26
  - *8.4.1 Elevation 125 mm 27*
  - *8.4.2 Elevation 200 mm 28*
  - *8.4.3 Elevation 235 mm 28*
  - *8.4.4 Elevation 460 mm 29*

9. EXAMINATION OF AEROSOL SAMPLES **31**

- 9.1 AEROSOL SAMPLES AND APPLIED METHODS 31
- 9.2 MORPHOLOGY OF THE AEROSOL PARTICLES 32
- 9.3 ED STUDIES OF THE AEROSOL SAMPLES 33
- 9.4 MASS SPECTROMETRIC ANALYSIS 35
  - *9.4.1 Precipitation on top of cooler 35*
  - *9.4.2 Precipitation on Ni collector plate in top area of cooler 35*
  - *9.4.3 Deposits on the impactor filters 35*

10. CONCLUSIONS **37**

ACKNOWLEDGMENTS **39**

REFERENCES **40**

List of tables

Table 1 Main characteristics of the CODEX-B4C bundle 10
Table 2 Temperature measurements 11
Table 3 Thermocouple (TC) characteristics 12
Table 4 Measurements of system parameters 12
Table 5 Main characteristics of CODEX test matrix 13
Table 6 Parameters of the CODEX-B4C commissioning test experimental database 14
Table 7 Main events and actions of CODEX-B4C test 16
Table 8 List of parameters available in the CODEX-B4C experimental database...........19
Table 9 Valve positions during the CODEX-B4C test 20
Table 10 Results of oxide layer thickness measurements....................26
Table 11 Elemental composition of various grains in sample No. 125 28
Table 12 Elemental composition of some grains in sample No. 200....................28
Table 13 Elemental composition of some grains in sample No. 235....................29
Table 14 Results of some quantitative EDX measurements....................29
Table 15 Results of the quantitative EDX analysis for some W-containing grains 30
Table 16 Results of the quantitative EDX analysis for Zr-Nb containing grains.............30
Table 17 Impactor valve positions during the CODEX-B4C test 31
Table 18 Results of aerosol impactor examination....................37

List of figures

Fig. 1 Scheme of the CODEX facility 41
Fig. 2 Horizontal cross section of the CODEX-B4C bundle 42
Fig. 3 Main geometrical parameters of the CODEX-B4C bundle 42
Fig. 4 Connections for aerosol sampling 43
Fig. 5 Test section of the CODEX facility 43
Fig. 6 Absorber rod of the CODEX-B4C bundle 44
Fig. 7 Central rod of the CODEX-B4C bundle 44
Fig. 8 Location of thermocouples and pyrometers in the CODEX-B4C bundle 45
Fig. 9 Placement of temperature measurements in the central rod 46
Fig. 10 Placement of temperature measurements on the heated rods 47
Fig. 11 Placement of temperature measurements on the shroud 48
Fig. 12 Placement of temperature measurements on the heat shields 49
Fig. 13 Placement of coolant temperature measurements 50
Fig. 14 Electrical power in the CODEX-B4C commissioning test 51
Fig. 15 Argon flowrate in the CODEX-B4C commissioning test 51
Fig. 16 Heated rod temperatures in the CODEX-B4C commissioning test 52
Fig. 17 Steel temperatures in the heat shield in the CODEX-B4C commissioning test ..52
Fig. 18 Electric power during the total recorded period 53
Fig. 19 Steam flowrate during the total recorded period 53
Fig. 20 Argon flowrate during the total recorded period 54
Fig. 21 Heated rod temperature during the total recorded period 54
Fig. 22 Main phases of the CODEX-B4C test 55
Fig. 23 C70: Central rod temperature at 70 mm 55
Fig. 24 C495: Central rod temperature at 495 mm 56
Fig. 25 GP150: Guide tube - central rod gap temperature at 150 mm 56
Fig. 26 GP300: Guide tube - central rod gap temperature at 300 mm 57
Fig. 27 GP450: Guide tube - central rod gap temperature at 450 mm 57
Fig. 28 GD495: Guide tube temperature at 495 mm 58
Fig. 29 SP545: Spacer temperature at 545 mm 58
Fig. 30 H70: Heated rod temperature at 70 mm 59
Fig. 31 H150: Heated rod temperature at 150 mm 59
Fig. 32 H300: Heated rod temperature at 300 mm 60
Fig. 33 H4501: Heated rod temperature at 450 mm, No. 1. 60
Fig. 34 H4502: Heated rod temperature at 450 mm, No. 2. 61
Fig. 35 H535: Heated rod temperature at 535 mm 61
Fig. 36 SH50: Shroud temperature at 50 mm 62
Fig. 37 SH150: Shroud temperature at 150 mm 62
Fig. 38 SH300: Shroud temperature at 300 mm 63
Fig. 39 SH450: Shroud temperature at 450 mm 63
Fig. 40 SH540: Shroud temperature at 540 mm 64
Fig. 41 HS70: Steel heat shield temperature at 70 mm 64
Fig. 42 HS150: Steel heat shield temperature at 150 mm 65
Fig. 43 HS300: Steel heat shield temperature at 300 mm 65
Fig. 44 HS450: Steel heat shield temperature at 450 mm 66
Fig. 45 HS540: Steel heat shield temperature at 540 mm 66
Fig. 46 OS70: Outside shield temperature at 70 mm 67
Fig. 47 OS150: Outside shield temperature at 150 mm 67

Fig. 48 OS300: Outside shield temperature at 300 mm....68
Fig. 49 OS450: Outside shield temperature at 450 mm....68
Fig. 50 OS540: Outside shield temperature at 540 mm....69
Fig. 51 PYR300: Pyrometer temperature at 300 mm....69
Fig. 52 PYR465: Pyrometer temperature at 465 mm....70
Fig. 53 TWATER: Water temperature in steam generator....70
Fig. 54 TSTEAM: Steam generator outlet temperature....71
Fig. 55 TIN1: Gas inlet temperature in the inlet junction....71
Fig. 56 TIN2: Gas inlet temperature at the bundle....72
Fig. 57 TOUT1: Gas outlet temperature in the outlet junction....72
Fig. 58 TCOOL: Gas temperature at the cooler inlet....73
Fig. 59 TOUTC: Gas temperature at the cooler outlet....73
Fig. 60 TAMB: Ambient air temperature....74
Fig. 61 PSYS: System pressure....74
Fig. 62 STEAM: Steam flow....75
Fig. 63 ARGON: Argon flow....75
Fig. 64 POWER: Electric power....76
Fig. 65 H2CON: Hydrogen concentration....76
Fig. 66 CH4CON: Methane concentration....77
Fig. 67 COCON: Carbon-monoxide concentration....77
Fig. 68 CO2CON: Carbon-dioxide concentration....78
Fig. 69 ARCON: Argon concentration....78
Fig. 70 MSFLOW: Mass flow at the mass spectrometer....79
Fig. 71 H2: Hydrogen flowrate....79
Fig. 72 CH4: Methane flowrate....80
Fig. 73 CO: Carbon-monoxide flowrate....80
Fig. 74 CO2: Carbon-dioxide flowrate....81
Fig. 75 Gas flowrates in the CODEX-B4C test....81
Fig. 76 API1: Concentration of 0,1-0,3 μm aerosols, internal counter....82
Fig. 77 API2: Concentration of 0,3-0,5 μm aerosols, internal counter....82
Fig. 78 API3: Concentration of 0,5-1,0 μm aerosols, internal counter....83
Fig. 79 API4: Concentration of 1-3 μm aerosols, internal counter....83
Fig. 80 API5: Concentration of 3-5 μm aerosols, internal counter....84
Fig. 81 API6: Concentration of 5-10 μm aerosols, internal counter....84
Fig. 82 API7: Concentration of >10 μm aerosols, internal counter....85
Fig. 83 APE1: Concentration of 0,3-0,5 μm aerosols, external counter....85
Fig. 84 APE2: Concentration of 0,5-1,0 μm aerosols, external counter....86
Fig. 85 APE3: Concentration of 1-3 μm aerosols, external counter....86
Fig. 86 APE4: Concentration of 3-5 μm aerosols, external counter....87
Fig. 87 APE5: Concentration of 5-10 μm aerosols, external counter....87
Fig. 88 APE6: Concentration of >10 μm aerosols, external counter....88
Fig. 89 Correlation between steam flowrate and aerosol particle concentration....88
Fig. 90 View of the upper part of the CODEX-B4C bundle....89
Fig. 91 View of the CODEX-B4C bundle with shroud....90
Fig. 92 View of the CODEX-B4C bundle without shroud....90
Fig. 93 Arrangement of X-ray radiography equipment during the CODEX-B4C test....91
Fig. 94 View of the top of the CODEX facility with X-ray radiography equipment....91
Fig. 95 X-ray radiography view of the upper part of the CODEX-B4C....92

Fig. 96 X-ray radiography view of the upper part of the CODEX-B4C........................93
Fig. 97 X-ray radiography of the CODEX-B4C bundle after the experiment...............94
Fig. 98 Bundle cross sections (left column) and view of the control rod......................95
Fig. 99 Bundle cross sections (left column) and view of the control rod......................96
Fig. 100 Bundle cross sections (left column) and view of the control rod....................97
Fig. 101 Layered oxide scale on heated rod No.4 at 125 mm elevation..........................98
Fig. 102 Oxide layer on heated rod Nr.6 at 175 mm elevation......................................98
Fig. 103 Thinning of stainless steel cladding of B_4C at 200 mm elevation.....................99
Fig. 104 A heated rod cut at 335 mm elevation. (No.3.) 99
Fig. 105 A heated rod cut at 335 mm elevation. (No.6.) 100
Fig. 106 Partly oxidized pellet at 410 mm elevation (Rod No.4.)................................100
Fig. 107 Oxidized control rod guide tube at 410 mm elevation. 101
Fig. 108 Heated rod No.3 at 535 mm elevation...101
Fig. 109 Chemical interactions between cladding, pellet...102
Fig. 110 Rod average oxide layer thickness on zirconium cladding 102
Fig. 111 Ratio of the molten material volume to the total..103
Fig. 112 EDX spectrum taken from the molten metall..103
Fig. 113 EDX spectrum for Fe-Cr-Ni rich aggregate at 460 mm elevation 104
Fig. 114 EDX spectrum for an aggregate with steel components................................104
Fig. 115 Scheme of impactor sampler 105
Fig. 116 Digital SEM images of various collectors at small magnification................106
Fig. 117 Digital SEM images for two collector samples No. 5B and 5D, resp. 107
Fig. 118 Digital SEM images of aerosols settled on collectors...................................107
Fig. 119 Typical digital SEM image of the aerosol..108
Fig. 120 U-rich particles (smaller and larger ones) 108
Fig. 121 Results of the standardless EDS analysis of U-rich 109
Fig. 122 Typical example for U-rich aerosol particle...109
Fig. 123 Results of the standardless EDS analysis of typical W-rich..........................110
Fig. 124 Typical results of standardless EDS analysis 110
Fig. 125 Results of the standardless EDS analysis for typical Fe-Cr-Mn 111
Fig. 126 Typical digital BE image taken from the Ni impaction plate showing 111
Fig. 127 Mass increase of impactors during the sampling 112

1. INTRODUCTION

During a severe accident the degradation of the core materials starts with the degradation of control rod materials, which have lower melting points than the fuel rods with zirconium cladding. Boron-carbide (B_4C) control rods or blades are used in different BWR and PWR type reactors, including the Russian design VVER-1000. In the framework of the COLOSS project of the EU 5th FWP several experimental programs with different scales (fragments, pellets, rods and bundles) were performed to study the impact of B_4C effect on core degradation and gas production. The main concern here was to identify the impact of B_4C on core liquefaction and the formation of CH_4.

The CODEX-B4C experiment was completed in May 2001 using an electrically heated VVER-1000 type bundle with a central B_4C control rod. The experimental conditions were to simulate a severe accident scenario in a VVER-1000 type reactor. The low temperature control rod degradation period was extended in order to produce more details of degradation process. The high temperature escalation above 2000 ^{o}C was performed in steam atmosphere without additional power increase. Slow cooling down took place in steam atmosphere. The test objectives were to provide experimental data on the following points:

- the impact of B_4C on the gas production (in particular H_2, CO, CO_2 and CH_4) and aerosols in conditions as representative as possible for a VVER-1000 reactor core under severe accident conditions,
- the impact of B_4C on the degradation of surrounding fuel rods and structures.

The test indicated no CH_4 formation under high temperature oxidation of B_4C pellets. The loss of geometry started with the melting of the steel cladding of the control rod and it accelerated the fuel rod degradation process. High release of aerosols was observed during the oxidation of core components in steam, the aerosol release correlated with steam flowrate. Temporary heat-up was observed in the cool-down phase as a result of local oxidation. The first visual examination of the bundle showed strong oxidation and degradation of shroud and control and fuel rods. The recorded on-line data were collected into an experimental database and are available for model development and code validation purposes.

The present report describes the main features of the facility and presents the on-line collected data, furthermore summarizes the results of post-test examination of the bundle and aerosol impactors.

2. THE CODEX FACILITY

The current configuration of the CODEX (COre Degradation EXperiment) integral test facility represents the geometrical arrangement of a VVER-1000 reactor fuel assembly and has been constructed of VVER materials. A schematic view of the facility is shown in Fig. 1. The basic part of the facility is the test section comprising a seven rod bundle of 600 mm heated length. The rods are arranged in hexagonal geometry (Fig. 2 and 3), the external diameter of the cladding is 9,13 mm. The six peripheral rods are electrically heated by tungsten bars. The 3,0 mm diameter bars in the heated rods are surrounded with ring-shaped UO_2 pellets - 3,6% enrichment of U^{235} - and enclosed in industrially fabricated Zr1%Nb alloy cladding. The central rod is a boron-carbide rod in steel cladding with Zr guide tube and is not heated (Fig. 6). The diameter of the hole in the pellet equals to 3,3 mm, while the external pellet diameter is 7,57 mm.

Pt covered Mo wires of 1,2 mm external diameter in spiral form are used for the connection of the W bars to the electrodes (Fig. 7). Water cooled jackets are used to cool the bottom and the top of the electrodes. The rods are filled up with argon, their internal pressure is 1,2 bar.

The rods in the bundle are fixed by three spacer grids, which are made of Zr1%Nb alloy. The spacers are located at elevations of 55 mm, 300 mm and 555 mm. The bundle is placed into a hexagonal shroud. The shroud material is Zr2.5%Nb alloy. The shroud has no perforations and it is surrounded by several thermal insulation layers of ZrO_2 (13 mm thickness), Al_2O_3 (92 mm external diameter), stainless steel (98 mm and 106 mm internal and external diameters) and mineral cotton (50 mm thickness). Between Al_2O_3 and stainless steel layers a small air gap compensates the thermal expansion. The cross section of bundle is given in Fig. 2. The test section inlet and outlet junctions for the coolant gas are at 0 and 650 mm elevations, respectively (Fig. 5). Two observation windows make possible the temperature measurements at 300 and 465 mm elevations by pyrometers. An additional window at 550 mm is used for video recording.

In the standard configuration of the facility the steam generator and superheater section of the facility provide argon and steam inlet flow for the test section during heating-up and cooling-down phases (Fig. 1). The 4 kW superheater and 6 kW steam generator powers produce high coolant temperatures (~600^{o}C) for the experiments. In the CODEX-B4C test very low steam flowrate was foreseen and for this reason direct injection of room temperature water into the superheater was applied with manual regulation. The steam generator was in stand by conditions during the test, but was not used for steam supply.

The coolant gas leaving the upper part of the test section flows through a steam condenser and enters the off gas system with filters. The coolant cools down, the steam condenses and the water is collected at the bottom of cooler-condenser unit. The high surface molecule-filters prevent release of aerosol particles, only noncondensable gases are released during the test into the exhaust system.

The gas concentration was measured in the off-gas system - behind the filters - using a quadropole mass spectrometer. The system was calibrated before the test and prepared for the on-line acquisition of H, CH_4, CO, CO_2 concentration in the Ar flow with 30 s scanning time.

Bundle type	VVER-1000
Number of rods	7
Number of heated rods	6
Number of unheated rods with B_4C	1
Pitch size	12,75 mm
Fuel rod cladding external diameter	9,13 mm
Fuel rod cladding internal diameter	7,72 mm
Fuel rod cladding material	Zr1%Nb
B_4C rod cladding external diameter	9,1 mm
B_4C rod cladding internal diameter	8,1 mm
B_4C rod cladding material	stainless steel
Guide tube external diameter	13,6 mm
Guide tube internal diameter	11,7 mm
Guide tube material	Zr1%Nb
Heater material	W
Heater bar diameter	3 mm
Pellets in heated rods	UO_2
External diameter of UO_2 pellets	7,57 mm
Internal diameter of UO_2 pellets	3,3 mm
External diameter of B_4C pellets	7,57 mm
Internal diameter of B_4C pellets	3,3 mm
Height of UO_2 pellets	10-13 mm
Height of B_4C pellets	10-13 mm
Heated length with UO_2 pellets	600 mm
UO_2 enrichment	3,6%
Material of spacer grids	Zr1%Nb
Number of spacer grids	3
Positions of spacer grids (center)	45 mm, 300 mm, 555 mm
Height of spacer grids	30 mm
Shroud material	Zr2%Nb
Shroud thickness	2 mm
Internal key size of shroud	37,4 mm
Length of shroud	600 mm

Table 1 Main characteristics of the CODEX-B4C bundle

Temperature	TC material/type	Position	Placement

measurement		[mm]	
C70	NiCr/NiAl	70	central rod
C495	W5%Re/W26%Re	495	central rod
GP150	NiCr/NiAl	150	guide tube - central rod gap
GP300	NiCr/NiAl	300	guide tube - central rod gap
GP450	NiCr/NiAl	450	guide tube - central rod gap
GD495	NiCr/NiAl	495	guide tube
SP545	W5%Re/W26%Re	545	spacer
H70	NiCr/NiAl	70	Heated rod
H150	NiCr/NiAl	150	Heated rod
H300	W5%Re/W26%Re	300	Heated rod
H4501	W5%Re/W26%Re	450	Heated rod No. 1.
H4502	W5%Re/W26%Re	450	Heated rod No. 2.
H535	W5%Re/W26%Re	535	Heated rod
SH50	NiCr/NiAl	50	Shroud
SH150	NiCr/NiAl	150	Shroud
SH300	W5%Re/W20%Re	300	Shroud
SH450	Pt/Pt13%Rh	450	Shroud
SH540	Pt/Pt13%Rh	540	Shroud
HS70	NiCr/NiAl	70	Steel heat shield
HS150	NiCr/NiAl	150	Steel heat shield
HS300	NiCr/NiAl	300	Steel heat shield
HS450	NiCr/NiAl	450	Steel heat shield
HS540	NiCr/NiAl	540	Steel heat shield
OS70	NiCr/NiAl	70	Outside shield
OS150	NiCr/NiAl	150	Outside shield
OS300	NiCr/NiAl	300	Outside shield
OS450	NiCr/NiAl	150	Outside shield
OS540	NiCr/NiAl	540	Outside shield
PYR300	pyrometer	300	Bundle/observation window
PYR465	ratio pyrometer	465	Bundle/observation window
TWATER	NiCr/NiAl		Steam generator
TSTEAM	NiCr/NiAl		Steam generator outlet
TIN1	NiCr/NiAl	0	Inlet junction
TIN2	NiCr/NiAl	0	Bundle
TOUT1	Pt/Pt13%Rh	630	Outlet junction
TCOOL	NiCr/NiAl		Cooler inlet
TOUTC	NiCr/NiAl		Cooler outlet
TAMB	NiCr/NiAl		Containment vessel

Table 2 Temperature measurements

In the CODEX-B4C experiment two laser airborne particle counters were applied. The aerosol sampling head of the inner instrument was connected to the top of the facility using a ~0.5 m long copper tube (Fig. 4). The outer sampling instrument was connected to the same point of the facility using a ~1.5m long copper tube. The sampling sites were connected to the top of the cooler, before the outlet gas entered the cooler tube section. Of course, the gas temperature was substantially lower, than at the escape from the bundle, but even in this area it was rather high. Impactors for later elemental analysis of aerosol were also connected to the upper part of the cooler. The sampling took place with 60 s period using magnetic valves.

Dynamic radiography was applied in the test making use of X-ray source and four imaging plates. The plates were moved into the view position in selected time periods and were expected to indicate the structural changes of the bundle during the test.

The main experimental parameters were collected by the data acquisition system. The values of input voltage and current, coolant flow rate, coolant inlet and outlet temperatures, water levels, system pressure, gas concentration, aerosol particle flow characteristics and rod temperatures were measured during the test (Table 4). Several high temperature thermocouples were built into the control and fuel rods, shroud, insulation layers at different elevations and two optical pyrometers were mounted in the test section (Figures 8-13 and Tables 2-4).

TC	1. (W1)	2. (W2)	3. (Pt)	4. (Ni)
type	W5%Re-W26%Re	W5%Re-W20%Re	Pt-Pt13%Rh	NiCr-NiAl
insulation	HfO_2	HfO_2	Al_2O_3	MgO_2
shroud	tantalum, niobium	niobium	zirconium	stainless steel
external diameter	2.3 mm	2.3 mm	1.5 mm	0.8 mm

Table 3 Thermocouple (TC) characteristics

Parameter	Device	Placement
Argon flowrate	calibrated flowmeter	gas supply system
Steam flowrate	calibrated pump	superheater
Gas concentration	mass spectrometer	gas off system
Steam generator level	DP transducer, 75 mbar/4-20 mA	steam generator
Condensate water level	DP transducer , 75 mbar/4-20 mA	condensate tank
Power	analog multiplier using shunt current and total voltage	rail of power supply
System pressure	P transducer, 6 bar/4-20 mA	Argon inlet junction

Table 4 Measurements of system parameters

3. THE CODEX EXPERIMENTAL PROGRAMME

In the AEKI an experimental programme was initiated focusing on the high temperature behaviour of VVER fuel and core materials. The interactions of Zr1%Nb cladding with UO_2 pellet, stainless steel spacer and boron steel absorber were studied in small scale separate effect tests [1][2]. On the basis of the experience gained in these tests the CODEX integral test facility was constructed to continue this work under more prototypic conditions.

The CODEX experimental programme consisted of seven tests until today. First the capabilities of the facility were demonstrated carrying out the CODEX-1 experiment with Al_2O_3 pellets. In the second experiment CODEX-2 the high temperature conditions in steam atmosphere lead to partial damage of the bundle, and the further core melting was stopped by slow cooling down in inert gas environment [3][4]. The CODEX-3/1 and CODEX-3/2 experiments were performed with quick water cooling [5][6]. Air ingress conditions were investigated in 9-rod PWR type bundle configuration in the CODEX-AIT-1 and CODEX-AIT-2 experiments within the OPSA project of the 4th FWP [7]. The last test was performed with a B_4C control rod. The main characteristics of the test matrix are given in Table 5.

Test	Bundle type	Pellet	Year	Test type
CODEX-1	7-rod VVER	Al_2O_3	1995	scoping test
CODEX-2	7-rod VVER	UO_2	1995	escalation and slow cooling down
CODEX-3/1	7-rod VVER	UO_2	1996	water quench at 1150 °C
CODEX-3/2	7-rod VVER	UO_2	1997	water quench at 1500 °C
CODEX-AIT-1	9-rod PWR	UO_2	1998	air ingress
CODEX-AIT-2	9-rod PWR	UO_2	1999	steam oxidation and air ingress
CODEX-B4C	7-rod VVER	UO_2,B_4C	2001	control rod degradation

Table 5 Main characteristics of CODEX test matrix

4. THE CODEX-B4C COMMISSIONING TEST

The commissioning test with the CODEX-B4C bundle was carried out on 29th March 2001. The test showed the operability of the main technological systems and data acquisition. The list of recorded parameters is summarised in Table 6.

The commissioning test included a stepwise increase of power up to a final peak value of 4 kW in inert gas atmosphere (Fig. 14 and Fig. 15). The temperatures on the fuel rods rised above 1100 °C (Fig. 16). Continuous temperature increase was observed in the heat shield (Fig. 17). Thermocouple SH450 failed before the test and the temperatures were too low for pyrometers PYR300 and PYR465. The measured data were collected and used for the evaluation of heat losses.

Name	Definition	Unit
C495	Central rod temperature at 495 mm	^oC
GP150	Guide tube - central rod gap temperature at 150 mm	^oC
GP300	Guide tube - central rod gap temperature at 300 mm	^oC
GP450	Guide tube - central rod gap temperature at 450 mm	^oC
GD495	Guide tube temperature at 495 mm	^oC
SP545	Spacer temperature at 545 mm	^oC
H70	Heated rod temperature at 70 mm	^oC
H150	Heated rod temperature at 150 mm	^oC
H300	Heated rod temperature at 300 mm	^oC
H4501	Heated rod temperature at 450 mm, No. 1.	^oC
H4502	Heated rod temperature at 450 mm, No. 2.	^oC
H535	Heated rod temperature at 535 mm	^oC
SH50	Shroud temperature at 50 mm	^oC
SH150	Shroud temperature at 150 mm	^oC
SH300	Shroud temperature at 300 mm	^oC
SH450	Shroud temperature at 450 mm	^oC
SH540	Shroud temperature at 540 mm	^oC
HS70	Steel temperature in heat shield at 70 mm	^oC
HS150	Steel temperature in heat shield at 150 mm	^oC
HS300	Steel temperature in heat shield at 300 mm	^oC
HS450	Steel temperature in heat shield at 450 mm	^oC
HS540	Steel temperature in heat shield at 540 mm	^oC
OS70	Outside shield temperature at 70 mm	^oC
OS150	Outside shield temperature at 150 mm	^oC
OS300	Outside shield temperature at 300 mm	^oC
OS450	Outside shield temperature at 450 mm	^oC
OS540	Outside shield temperature at 540 mm	^oC
PYR300	Pyrometer temperature at 300 mm	^oC
PYR465	Pyrometer temperature at 465 mm	^oC
TIN1	Coolant inlet temperature in the inlet junction	^oC
TIN2	Coolant inlet temperature at the bundle	^oC
TOUT1	Coolant outlet temperature in the outlet junction	^oC
TCOOL	Coolant outlet temperature in the cooler	^oC
TAMB	Ambient air temperature	^oC
PSYS	System pressure	bar
ARGON	Argon flowrate	g/s
POWER	Total electrical power of the heater rods	W

Table 6 Parameters of the CODEX-B4C commissioning test experimental database

5. THE CODEX-B4C TEST

The test conditions of CODEX-B4C experiment were selected on the basis of pre-test calculations [8],[9],[10] and were to simulate a severe accident scenario and emphasize the role of the control rod in the degradation process. The test included five main phases (see Fig. 22):

0-13646 s, preheating period
Low (500 W) electric power and ~600 °C inlet argon temperature were the main conditions for this period. Stable temperature distribution was reached, which was characterized with 500~600 °C values through the total length of the test section.

13640-15600 s, power ramp
The electric power was increased from 500 W to 2560 W (Fig. 64). The initial increase rate was 2 W/s, and it was decreased later to reach a smooth heat-up history. Steam injection was started at 13640 s with a flowrate of ~0.1 g/s (Fig. 62).

15600-16830 s, control rod degradation period
At the beginning of this period the temperature in the upper part of the bundle reached ~1500 °C (Fig. 24, 28 and 29). This temperature was stabilised with the help of manual steam flowrate regulation between 0.0-0.5 g/s (Fig. 62). At this temperature the melting of the steel cladding was expected. The gas measurement shows that some H_2 production took place during this plateau (Fig. 71), but it seemed that the guide tube remained intact and it prevented the B_4C from strong oxidation.

16830-17050 s, bundle degradation period
The argon flowrate was reduced from ~3 g/s to ~1,3 g/s (Fig. 63) and the steam flowrate was increased to 0,5 g/s (Fig. 62) in order to initiate temperature escalation. CO formation started about 3 minutes before the escalation (Fig. 73) and it could be considered as time of control rod failure (16600 s). At about 16900 s 2000 °C temperature was reached in the upper part of the bundle (Fig. 29, 32, 33-35). After the escalation phase the H_2 production increased together with CO (Figures 71 and 75). CO_2 appeared with some delay and no CH_4 was detected (Figures 72, 74 and 75).

17050-21705 s, cool-down period
The power was switched off (Fig. 64), but the coolant conditions were not changed at the initiation of cooling down (Fig. 62 and 63). This resulted in slow temperature decrease in the lower and central part of the bundle (e.g. Fig. 23). However the temperature measurements in the upper part indicated some temperature increase (Fig. 28-29) , which was probably the result of local oxidation. During the cool-down period the gas production continued and the aerosol impactors indicated maximum release that time. Steam injection was stopped and cold argon was injected for final cool-down.

A short summary on the main events of the test is given in Table 7.

Time [s]	Event
0	Start of Ar injection, 2,3 g/s
1200	Increase of electric power up to 500 W

13640	Start of steam injection, 0,1 g/s
13646	Start of power increase with 2 W/s
14000	Start of H_2 production
15600	1500 ^oC reached in the upper part of the bundle
15600	2560 W power constant
15610	Start of steam flowrate regulation
16830	Argon flowrate reduction to 1,3 g/s
16850	Steam flowrate increase to 0,5 g/s, end of steam flowrate regulation
16600	Start of CO production, sign of control rod failure
16908	2000 ^oC reached in the upper part of the bundle
17050	Switch off power
18708	Stop of steam injection
18884	Temperatures below 700 ^oC in the upper part of the bundle
20858	Injection of cold Ar
21705	End of data collection

Table 7 Main events and actions of CODEX-B4C test

6. EXPERIMENTAL RESULTS

The test conditions of CODEX-B4C experiment were selected to simulate a severe accident scenario and emphasize the role of the control rod in the degradation process. The preheating period served to establish a stable temperature distribution in the bundle and in the test section without chemical interactions and changes in the geometry of the rods. The power ramp simulated the heat-up of the bundle as a consequence of loss of heat removal from the reactor core and the power production due to decay heat. After the power ramp the further temperature increase was artificially delayed with the regulation of steam flowrate and so an extended time window was available for the degradation of control rod before the beginning of fuel rod degradation. The steam starving conditions established in this period were supposed to create hydrogen rich atmosphere and in this manner to facilitate methane formation. The escalation period was initiated without further power increase, only the coolant parameters were changed. After reaching the desired degree of bundle degradation slow cooling down was applied in steam atmosphere. This last phase covered wide temperature range and provided possibility for the investigation of gas production.

The temperatures increased until the initiation of cool-down. The highest temperatures were reached in the upper part of the bundle (~450 mm, Fig. 28, 33-34), but 2000 ^oC was seen at 300 mm elevation as well (Fig. 32). After switching off electric power some local temperature peaks were observed, probably as results of local oxidation and/or relocation processes. The temperatures measured in the gap between the central steel cladding and the guide tube were significantly lower than the surrounding heated rod temperatures (Fig. 25-27), these measurements correlated with the coolant temperatures more than with the rod temperatures. The maximum temperature ~2300-2400 ^oC was reached on the guide tube at 495 mm elevation (Fig. 28) and on the heated rods at 450 mm (Fig. 33-34). On the guide tube a second temperature peak with the same magnitude was also detected during the cool-down phase (Fig. 28).

Shroud temperature rised above 1600 °C at 450 mm (Fig. 39). The maximum temperature in the steel shield was 800 °C (Fig. 44) and on the outside shield 160 °C (Fig. 46). The maximum temperature measured by the pyrometer was ~1900 °C (Fig. 52). The inlet gas temperature was ~600 °C until the escalation period, then this value started to decrease due to the increased steam flowrate (Fig. 55). The highest outlet gas temperature was ~1200 °C (Fig. 57).

The gas measurement with mass spectrometer indicated hydrogen, methane, carbon-monoxide and carbon-dioxide. Significant hydrogen production was seen as a common result of Zr and B_4C oxidation in steam (Fig. 71). The peak of hydrogen generation was related to the temperature escalation, the maximum H_2 production was ~40 mg/s and the total integrated H mass was about 25 g. The methane measurement showed very low values, practically below the detection limit (Fig. 72). As a conclusion no methane formation was observed. Both CO and CO_2 production was detected, the appearance of CO_2 was delayed compared to CO (Fig. 73-74 and 75). The maximum production rate was 16 mg/s for CO and 4 mg/s for CO_2. The integrated mass of CO and CO_2 showed that 40% of the original B_4C was oxidized during the test. Additionally to the on-line gas concentration measurements three gas balloons were filled during the test and analyzed later. The comparison of on-line data with the results of balloon examination showed good agreement.

Dynamic X-ray radiography application showed some sequence of mechanical changes in the rod structure (see chapter 8.1).

The two particle counters indicated high release of aerosols when steam was available in the coolant (Figures 76-88). The number of particles increased after the beginning of steam injection. The steam supply was interrupted at ~14300 s for a short time and it resulted in a characteristic decrease of particle numbers (Fig. 62 and e.g. Fig 83). Dramatic increase was observed when the bundle temperature reached 1500 °C (e.g. Fig. 80). The typical number of particles in each measured range was close to 10^6. The oscillating behaviour of the measured values was in direct correlation with the steam supply, which was in manual regulation mode. With no steam flow the number of particles decreased, while with available steam flow sharply increased (Fig. 89). It indicates that there was a strong correlation between the oxidation phenomena and the production of particles. The particle counters showed the start of the decrease of particle flow before the escalation period and it continued during cool-down.

The visual observation of the bundle indicated strong degradation. In the upper part the melting of the central rod produced some chemical compositions, which sticked together the rods (Fig. 90). The external surface of the shroud seemed to survive heavy oxidation (Fig. 91). The rod in the lower part was also oxidised and fragmented (Fig. 92). The shroud was very brittle and could be removed easily from the bundle. However after visual observation of the rods the shroud was put back to its original position and the structure was fixed with epoxy.

7. EXPERIMENTAL DATABASE

The experimental data were collected for code validation purposes into a database, which covers 27105 s time period with 1 s frequency. The frequency of gas composition measurements and particle counter recording was different (30 s, 10 s, 5 s) and for this reason the database has the appropriate values in the recorded points only. The parameters are listed in Table 8 and plotted in Figures 23-72 and 74-88 for the period of 13500-18500 s. The position of gas supply and impactor valves recorded during the test is summarized in Table 9.

The database is presented in a large ASCII type file. The first column of the matrix contains the time. The "0" experimental time was set to real time 13:50:24, 25th May 2001. Each variable listed in Table 8 is given in a separate column in the file. The order of variables is the same as listed in the table. The commissioning test database has a similar structure, but the number of recorded variables is less (Table 6). The database includes some results of the metallographic bundle examination as well (see chapter 8.2).

Name	Unit	Definition
Time	s	Time
C70	^{o}C	Central rod temperature at 70 mm
C495	^{o}C	Central rod temperature at 495 mm
GP150	^{o}C	Guide tube - central rod gap temperature at 150 mm
GP300	^{o}C	Guide tube - central rod gap temperature at 300 mm
GP450	^{o}C	Guide tube - central rod gap temperature at 450 mm
GD495	^{o}C	Guide tube temperature at 495 mm
SP545	^{o}C	Spacer temperature at 545 mm
H70	°C	Heated rod temperature at 70 mm
H150	°C	Heated rod temperature at 150 mm
H300	°C	Heated rod temperature at 300 mm
H4501	°C	Heated rod temperature at 450 mm, No. 1.
H4502	°C	Heated rod temperature at 450 mm, No. 2.
H535	°C	Heated rod temperature at 535 mm
SH50	°C	Shroud temperature at 50 mm
SH150	°C	Shroud temperature at 150 mm
SH300	°C	Shroud temperature at 300 mm
SH450	°C	Shroud temperature at 450 mm
SH540	°C	Shroud temperature at 540 mm
HS70	°C	Steel heat shield temperature at 70 mm
HS150	°C	Steel heat shield temperature at 150 mm
HS300	°C	Steel heat shield temperature at 300 mm
HS450	°C	Steel heat shield temperature at 450 mm
HS540	°C	Steel heat shield temperature at 540 mm
OS70	°C	Outside shield temperature at 70 mm
OS150	°C	Outside shield temperature at 150 mm
OS300	°C	Outside shield temperature at 300 mm
OS450	°C	Outside shield temperature at 450 mm
OS540	°C	Outside shield temperature at 540 mm

PYR300	°C	Pyrometer temperature at 300 mm
PYR465	°C	Pyrometer temperature at 465 mm
TWATER	°C	Water temperature in steam generator
TSTEAM	°C	Steam generator outlet temperature
TIN1	°C	Gas inlet temperature in the inlet junction
TIN2	°C	Gas inlet temperature at the bundle
TOUT1	°C	Gas outlet temperature in the outlet junction
TCOOL	°C	Gas temperature at the cooler inlet
TOUTC	°C	Gas temperature at the cooler outlet
TAMB	°C	Ambient air temperature
PSYS	bar	System pressure
STEAM	g/s	Steam flow
ARGON	g/s	Argon flow
POWER	W	Electric power
H2CON	% vol	Hydrogen concentration
CH4CON	% vol	Methane concentration
COCON	% vol	Carbon-monoxide concentration
CO2CON	% vol	Carbon-dioxide concentration
ARCON	% vol	Argon concentration
MSFLOW	g/s	Mass flow at the mass spectrometer
H2	mg/s	Hydrogen flowrate
CH4	mg/s	Methane flowrate
CO	mg/s	Carbon-monoxide flowrate
CO2	mg/s	Carbon-dioxide flowrate
API1	particle/l	Concentration of 0,1-0,3 μm aerosols, internal counter
API2	particle/l	Concentration of 0,3-0,5 μm aerosols, internal counter
API3	particle/l	Concentration of 0,5-1,0 μm aerosols, internal counter
API4	particle/l	Concentration of 1-3 μm aerosols, internal counter
API5	particle/l	Concentration of 3-5 μm aerosols, internal counter
API6	particle/l	Concentration of 5-10 μm aerosols, internal counter
API7	particle/l	Concentration of >10 μm aerosols, internal counter
APE1	particle/l	Concentration of 0,3-0,5 μm aerosols, external counter
APE2	particle/l	Concentration of 0,5-1,0 μm aerosols, external counter
APE3	particle/l	Concentration of 1-3 μm aerosols, external counter
APE4	particle/l	Concentration of 3-5 μm aerosols, external counter
APE5	particle/l	Concentration of 5-10 μm aerosols, external counter
APE6	particle/l	Concentration of >10 μm aerosols, external counter

Table 8 List of parameters available in the CODEX-B4C experimental database

Valve	Opening time [s]	Closing time [s]	Period
Impactor No. 1	15068	15128	Power ramp
Impactor No. 2	16193	16253	Control rod degradation
Impactor No. 3	16254	16314	Control rod degradation
Impactor No. 4	16315	16375	Control rod degradation
Impactor No. 5	16898	16958	Bundle rod degradation
Impactor No. 6	16959	17019	Bundle rod degradation
Impactor No. 7	17020	17080	Bundle rod degradation
Impactor No. 8	17081	17141	Cool-down
Impactor No. 9	17142	17202	Cool-down
Impactor No. 10	18073	18133	Cool-down
Argon flow, normal	0	20858	from preheating to cool-down
Argon flow, safety	20858	-	Final cool-down

Table 9 Valve positions during the CODEX-B4C test

8. EXAMINATION OF BUNDLE

The post-test examination of the bundle started with X-ray radiography of the total bundle length. After it horizontal cross sections were prepared and metallographic analysis was performed. The last step of bundle examination was the SEM analysis of samples taken from the melt in the central rod of the bundle.

8.1 Radiography

During the planning of CODEX-B4C experiment it was decided to observe the effect of fuel bundle degradation phenomena by in-situ X-ray Radiography (XR). A special arrangement was designed for this aim, as it is shown in Fig. 93. The source was a MXR-300 type portable X-ray generator with an available collimator, the detector screens were BAS MS 20×25 cm type radiation luminescence imaging plates (IP) shown in Fig. 94. The reader of the IP was BAS 1800 type contributed by AIDA reconstruction software. Primary the unavoidable background radiation was measured by a model experiment after the danger zone and the escaping way were indicated. The IP-s were shielded by lead bricks regarding their radiation sensitivity. The X-ray generator and the IP-s were cooled avoiding the heating effects of the test section inside the covered ZR-6 vessel. The necessary exposure time was 60 seconds at 280 kV and 3 mA.

In the ZR-6 vessel several pictures were taken before, during and after the test. Figures 95 and 96 show the sequence of pictures. We were able to produce four pictures immediately from the beginning of temperature escalation phase by a remote controlled exposure transporter (at 16176, 16800 s, 16900 s and 17000 s experimental time). The pictures show the upper part of the bundle, the elevation of the pyrometer observation window seen on the right side was 465 mm, and the horizontal wire seen in the picture was a thermocouple. No structural change was seen in the first four pictures taken between cold state and 1530 ^{o}C. The first sign of degradation was seen at 16800 s (1600 ^{o}C): a small droplet of molten material was moving down on the left side fuel rod. The step by step degradation above 1800 ^{o}C can be followed in the next pictures. At higher temperatures the heavy oxidation of Zr shroud could be observed, the oxide scale was peeling off from its original position and a multilayer structure was formed on the surface. At high temperature some fragments could be seen as well between the fuel rods. The fuel rods in picture taken in the cool-down phase at 20400 s were very close to each other, probably due to the failure of the upper spacer grid.

Later useful information was offered about the damage of rod structure giving a map of the total length of the bundle, as it is shown in Figure 97. The upper part of the bundle showed heavy degradation, missing pieces of shroud could be seen close to the top. The lower part seemed intact. These pictures were taken at the dynamic radiography station at the Budapest Research Reactor.

8.2 Bundle cross sections

After the experiment the degraded bundle was fixed with epoxy and cut at numerous elevations to get cross sections for metallographic investigations. Photos were made from the polished surfaces for studying them to clear up the high temperature processes performed during the test. The UO_2 pellets were kept roughly in their original position by the tungsten heater bars, while strong degradation took place in the central control rod.

The elevations from the bottom of the bundle where the polished cross sections were made for studies are the followings: 50, 75, 100, 125, 150, 175, 200, 235, 335, 410, 460, 535 and 555 mm. More than 250 pictures of metallographic investigation have been collected into the CODEX-B4C post-test examiantion database, which is available in electronic form (individual *pdf* file for each cross section). The database includes the macro view of each bundle at each cross section, the enlarged view of each rod and some interesting parts of the fuel and control rods, showing important details of bundle degradation. In the present report only part of the database is shown and commented in the next chapters.

8.2.1 Elevation 50 mm

At this elevation a spacer grid was located (Fig. 98). The ceramic rods with double channels for thermocouples could be recognized. At some places molten material filled up the space between fuel rod and spacer plates (see for instance at the rod in the left side upper corner). Larger debris pieces have not appeared for the spacer hold them up. The original shape of the bundle was preserved. (The deformed shroud view has only technical reason; the surface was not ground sufficiently to get a plan surface on the whole cut.)

8.2.2 Elevation 75 mm

At this elevation the structure of the bundle was also perfectly preserved (Fig. 98). The thickness of oxide layers did not affect the total view. At this height being not far above the spacer grid a substantial amount of debris and molten phase could be seen between the rods. The ceramic double tubes could also be seen perfectly. The boron-carbide in central rod had a hole for a thermocouple placed in from the bottom side.

8.2.3 Elevation 100 mm

Even at this elevation the original structure of the bundle remained intact (Fig. 98). The debris particles stopped between the rods were large, it seemed that they were pieces from the shroud oxidized fully at the top region of the bundle, because they are flat oxide plates.

In the control rod the molten material has been flown down to this height between the steel cladding of boron carbide and the Zr1%Nb guide tube and solidified between two ceramic thermocouple tubes with double holes. The SEM-EDX analyses resulted in large iron content proving that it was from the melted higher part of steel cladding tube. The average thickness of oxide layer at this height was found to be 5 μm, it could be seen only slightly in the picture.

8.2.4 Elevation 125 mm

The debris between the rods appeared at the same side as at elevation 100 mm (Fig. 98). It seemed the debris pieces here were also from the shroud as before. In the absorber rod at this elevation also molten metal was flown down between the steel cladding tube of boron carbide and the guide tube. The molten metal phase was between the same two thermocouples inlet ceramic rod as at 100 mm elevation.

The oxide layers at this elevation were usually thicker than 20 μm. At all rods the oxide phases were layered to 5-7 μm thickness. According to earlier experiences this phenomena appeared when the oxidation temperature did not exceed 1000 °C. A picture of a layered oxide is shown in Fig. 101. It was made from the heated rod No. 4 from a site, where the outer oxide layer was separated from the others.

8.2.5 Elevation 150 mm

The main feature of the picture is, that the number of debris was very few (Fig. 98). One piece near to the central rod was from the upper spacer with oxide on both side and α-Zr(O) layer in the middle. Ratio of their thicknesses was 1:1:1. A second interesting character had the molten metal between the stainless steel envelope of boron carbide and the guide tube. At this height it was flowed around the full circle of the gap (see Fig. 98). The oxide layer formed during the steam oxidation was not layered as at the previous elevation but formed a tight phase on the surface of zirconium alloy.

8.2.6 Elevation 175 mm

The bundle had the original geometry at this elevation too (Fig. 99). The main conclusions drawn from this picture of the cross section are the followings: the debris was between the heated rods in the right side bottom corner, it fell down from the top part of shroud broken down just at this side. The molten metal phase in the gap of central rod was substantially less than at elevation 150 mm (about 1/4 of total circle as can be seen in Fig. 99). The eutectic molten material thinnered the steel cladding of B_4C. The oxide layers on the heated and control rods were tight, homogenous phases as shown in Fig. 102 indicating high temperature (> 1000 °C).

8.2.7 Elevation 200 mm

The original geometry has been maintained (Fig. 99). The break on the shroud in the righ side of the cross section was formed at cutting with the diamond disc. The debris pieces appeared between heated rods in the same right side corner, as at the elevation 175 mm. The white area between rod No. 5. and the shroud was a part from ZrO_2 heat isolation wool and the shroud stuck together at the top part of the bundle. Beside it a piece from heavily oxidized shroud could be seen as well.

The molten metal phase formed at upper part of control rod has been flowed further down but it wetted the steel cladding of B_4C and at some places thinnered it (see Fig. 103). Presumably the high temperature at this level accelerated the eutectic melting enough resulting in substantial thinning of the steel tube. The oxide phases on the zirconium alloy surfaces were not layered. In the vicinity of one of the two thermocouple inlet appeared about 1/8 circumference filled with eutectic. At an another place a small molten metal bridge has been formed, where the steel tube thickness has been reduced to half of the original value.

8.2.8 Elevation 235 mm

The bundle structure was near to the original shape but the control rod was slightly damaged (Fig. 99). The shroud has been broken up at the same edge as at previous cuts. (The shroud was welded at this corner, that is why the strength of the shroud material was lower enough to became broken during the slicing process.) Only two debris pieces can be seen. Both the Zr1%Nb guide tube and the steel cladding of absorber material has been thinnered at the gap side by the eutectic material flowing down. The gap was filled with eutectic metal on 1/8 circumference only.

The outer oxide layers on Zr1%Nb tubes were spalled off at some places, however the main part of the oxide was a solid, not layered phase.

8.2.9 Elevation 335 mm

The bundle full diameter cross section (see Fig. 99) showed different extent of deformations on the components of the bundle. At this elevation no debris pieces could be seen. The shroud was more or less intact except the break between the heated rods No.3. and No.4. like at cuts of lower elevations.

The cladding of heated rods were strongly oxidized and only zirconium oxide and α-Zr(O) phases could be seen without the layer with low oxygen content forming β-phase at high temperature (>863 °C). The volume expansion of oxide compared to the metal phase increased the circumference of cladding resulting gaps between the uranium dioxide pellets and the inner surface of cladding tubes. (Fig. 104) At the heated rod in the right side of the cross section a thermocouple inlet tube was near to its outer surface. Molten metal was stuck between the cladding surface and thermocouple cladding by surface tension effect. In Fig. 99 an outer thin oxide layer had been separated from the main oxide phase. Similar effect was seen on other rods as well. Presumably the external oxide layer was formed at ~1500 ^{o}C (control rod degradation phase), while the thick oxide on the metallic surfaces was result of oxidation during the escalation phase (~2000 ^{o}C).

As regard the control rod it could clearly be seen, that the steel cladding disappeared and the boron carbide pellet diameter substantially reduced (Fig. 99). It was reacted by the steam accessible after the melting of steel cladding tube.

8.2.10 Elevation 410 mm

At elevation 410 mm the bundle was heavily damaged (Fig. 99). Large part of the shroud was deformed. Its shape remained slightly better in the vicinity of heated rods No.1 and 2. Presumably the streaming gas was slower at this side, because at lower elevations debris were up to higher level as could be seen at 125 mm (Fig. 98) and resulted in lower streaming rate.

The cladding of heated rods remained full circle at 4 cases, but two of them were broken up where the opened control rod guide tube touched them. The damage was more severe at rod No. 4. which opened certainly earlier and some part of uranium dioxide pellet has been oxidized as well (Fig. 107). Their Zr1%Nb cladding materials were oxidized in full thickness at each heated rod. Molten metal appeared both in the pellet-cladding and the tungsten-pellet gap.

At the control rod the oxidized and opened up Zr1%Nb guide tube remained only (Fig. 99). Because this tube has been oxidized both on their outer and inner surface, it has been broken into two layers when the oxide phases met each other. The closely equal thickness of the two layers indicated, that the oxide formation rates were the same on both sides as shown in Fig. 106. The symmetrical oxide scale indicated that the guide tube opened in the early phase of the experiment and during the high temperature escalation the steam had access to the internal surface as well.

8.2.11 Elevation 460 mm

At this elevation the damage of the bundle was not stronger than at 410 mm (Fig. 100). The heated rods had their oxidized cladding on the original position except those two, where the opened absorber guide tube hurt the rigid oxide layer of the rods. The guide tube has been fully oxidized and it looked like at the 410 mm elevation. However the shroud was more damaged and has been broken into small pieces. Certainly the debris at the bottom of the bundle was originated mainly from this and higher elevation shroud.

8.2.12 Elevation 535 mm

At this height the upper spacer was built in (Fig. 100). It resulted in a stronger damage than at lower and higher levels. The mechanical force of the spacer kept the rigid oxidized zirconium alloy claddings around the uranium dioxide pellets. Some interactions of pellet, eventually oxidation was found only on the heated rod at the top of the cross section (Fig.108) Even the heavily oxidized guide tube has been fixed in its original position, of course without boron carbide pellet and steel cladding. The fully oxidized shroud has been broken up at many places.

8.2.13 Elevation 555 mm

The highest level cut has been prepared at 50 mm lower than the top of the bundle (Fig. 100). The damage of heated rods and the central control rod was slightly less than at lower elevations. Only the shroud ruined more heavily here than at lower levels. Certainly the broken pieces of shroud were falling down resulting large part of debris inside and outside the bundle. The uranium dioxide pellets and around them the fully oxidized cladding were fixed by the tungsten heaters. Chemical interaction was found only at heated rods in the top of the cross section, where the metal envelope of thermocouple inlet accessory resulted in eutectic interaction with the zirconium cladding and some extent with the UO_2 pellet (Fig. 109). Even the guide tube was fully oxidized, it remained in the central position with enlarged diameter but with full circle with deformed shape. Similar splitting to two layers could be seen as at lower elevations (Fig. 100).

8.3 Oxide layer thickness measurements

The oxide layer thickness on zirconium alloy tubes has been determined by optical microscopy. Separate measurements were taken on each rod. Up to five positions were measured to determine the average values for rod with large variation of oxide scale thickness. Above 410 mm level full oxidation of claddings has been found and no oxide layer measurements were taken. The results are shown in Table 10 and summarized in Fig. 110.

elevation [mm]	rod No.	oxide layer thickness in position No.1 [μm]	oxide layer thickness in position No.2 [μm]	oxide layer thickness in position No.3 [μm]	oxide layer thickness in position No.4 [μm]	oxide layer thickness in position No.5 [μm]	rod average [μm]	cross section average oxide layer thickness [μm]
50		2					2	**2**
75		4					4	**4**
100		5					5	**5**
125	1	22	21				21.5	**17.4**
	2	18	27				22.5	
	3	5	4				4.5	
	4	33	29				31.0	
	5	22	22				22.0	
	6	5					5.0	
	7	14	16				15.0	
150		23	25				24.0	**24**
175	1	25	26	30			27.0	**34.1**
	2	36	34	36	38		36.0	
	3	42	39	42			41.0	
	4	36	32	32	6		26.5	
	5	45	43	29	32		37.3	
	6	35	37	33			35.0	
	7	36					36.0	

200	1	43	45	52			46.7	**36.8**
	2	40	37	40			39.0	
	3	32	23	32			29.0	
	4	35	39	38			37.3	
	5	45	37	40	25	30	35.4	
	6	30	34	31			31.7	
	7	37	39	39			38.3	
235	1	39	42	40			40.3	**49.2**
	2	54	50				52.0	
	3	49	62				55.5	
	4	58	61				59.5	
	5	27	31	30			29.3	
	6	54	51	58			54.3	
	7	50	55	55			53.3	
335	1	165	147	202	212		181.5	**231.0**
	2	260	244	246			250.0	
	3	193	202	198	185		194.5	
	4	275	224	216			238.3	
	5	221	244	240			235.0	
	6	262	184	226	216	240	225.6	
	7	352	352	173			292.3	
410	1	805					805	**982.0**
	2	989					989	
	3	1011					1011	
	4	989					989	
	5	750					750	
	6	1068					1068	
	7	1262					1262	

Table 10 Results of oxide layer thickness measurements

We performed some model calculations regarding the oxide layer thicknesses using the time-temperature scenario during the test. The calculated and estimated data were close to each other indicating not more than 100°C temperature difference between the measured and calculated values.

8.4 Control rod melt investigation

The boron carbide remained in its original position below 335 mm. No boron carbide pellets could be seen in the elevations above this position, so ~45% of the original B_4C rod disappeared during the test. It is in good agreement with the results calculated from the released CO and CO_2 content, which resulted that ~40 % of B_4C inventory has been oxidized by steam. The volume of the melt in the lower part of the control rod was estimated on the basis of metallographic examinations as ~3.5 cm^3. Fig. 111 shows the axial variation of the volume filled up by the melt in the gap. At 235 mm the melt almost completely closed the gap.

Small size samples (filings) were taken from the gap between the control rod and guide tube, where molten material was observed at lower elevations. In the upper part of the bundle red-yellow surfaces were observed, which were suspected to be originated from the control rod. For this reason samples from an upper cross section were taken as well, here the control rod and guide tube were damaged, so the sampling was applied to the guide tube surface. The filings were originated from the following places:

- cross section at 125 mm elevation, gap between stainless steel cladding and guide tube
- cross section at 200 mm elevation, gap between stainless steel cladding and guide tube
- cross section at 235 mm elevation, gap between stainless steel cladding and guide tube
- cross section at 460 mm elevation, guide tube surface

Scanning electron microscopy (SEM) and energy disperse microanalysis (EDX) were applied to study the elemental composition of filings. The aim of our studies was to get information on the presence or absence of control rod components in small sized samples gained by rasping and to analyze the elemental composition of the selected samples. We wanted to analyze the samples in as received state, due to the fact, that any evaporated layer influences the quantity of elements with low atomic number. First we made preliminary study to get overall information on the elemental composition, and then we used an EDX system with thin window. This instrument is able to detect from ${}_{5}B$ to ${}_{92}U$, however the detection limit is worse (about one order of magnitude) for light elements than for medium or higher atomic number of elements. We analyzed generally whole grains or aggregates of the samples, but in some cases when the grains exhibited strong electric charging, we tried to analyze at some selected spots of the grains.

The applied instruments were the followings:

1. Philips SEM 505 type scanning electron microscope used at 20 kV and with a few nA beam current.
2. LINK AN 10/55S type energy disperse microanalyser suitable for detecting elements between ${}_{11}Na$ and ${}_{92}U$ with a few tenth of mass % detection limit.
3. Oxford EDX with thin window attached to JEOL Superprobe 733 electron beam microanalyser. We used 10 kV and/or 15 kV accelerating voltages and 3 nA beam current.

8.4.1 Elevation 125 mm

The most frequently found element at this elevation was zirconium, besides chromium, iron, nickel, oxygen, carbon could be detected. It might be supposed that some amount of niobium was also present in the Zr-rich grains. The results of the quantitative EDX analysis are shown in Table 11. It can be seen from the table that the deviation of the quantity of a given element was rather high for small amounts. There was variation in the elemental composition of the grains of the filings, however it seemed that there were three main types:

1. Zr-rich grains: as accompanying component elements Fe and Ni, at some cases small amounts of O or/and C could be present.
2. Cr-Zr-Fe containing grains with some amounts of O and C
3. Zr-O-C containing grain (rarely found).

We could not find boron in the analyzed grains, but carbon was present in some of them. The oxygen content of the filings was generally very low, only a few m %, except to the grain, which had high amount of C and Zr.

No. of grain	C (m %)	O (m %)	Cr (m %)	Fe (m %)	Ni (m %)	Zr (m %)	Nb (m %)
1	2.1 ±2.8	6.3 ±1	0	2.4 ±4.1	0	89.1 ±4.6	0
2	0	0	0	5.3 ±1.9	5 ±1.1	85 ±2.4	4.8 ±1.5
3	0	1.7 ±0.4	0	7.2 ±1.8	5.1 ±1.1	81.5 ±2.3	4.6 ±1.5
4	0	2.8 ±0.5	0	12.5 ±2.3	9.7 ±1.4	75 ±2.3	0
5	14.8 ±2.3	3.9 ±1.1	6 ±9	6.8 ±2.9	0	68.5 ±7.2	0
6	0	6.8 ±1.1	0	16.3 ±3.4	8.9 ±2	68 ±3.3	0
7*	0.2 ±1.4	4.3 ±1	43.4 ±5.5	9.1 ±3.4	0	41.5 ±4.3	0
8	13 ±1.7	2.9 ±0.8	21.7±5.8	10.7 ±2.6	0	51.7 ±4.2	0
9	6.9 ±1	3.5 ±0.7	46.9 ±4	18.7 ±2.9	0	24 ±2	0
10	31.1 ±8.7	26 ±4.7	0	0	0	43 ±6.5	0

Table 11 Elemental composition of various grains in sample No. 125

Note: * Grain No. 7 had 1.5 ±0.4 m % Ca as impurity.

8.4.2 Elevation 200 mm

The results of the quantitative EDX analysis are shown in Table 12. It could be established from the table, that there were Zr-rich grains with small amounts (lower than 3 m %) of O except one grain with higher amount of O. In grains with lower amounts of Zr we could find Fe and Cr or Ni or both of them. In such grains there was only small amount of O. Boron could not been found, carbon was suspected in one case, but the deviation of its possible quantity was very high.

8.4.3 Elevation 235 mm

EDX spectrum characteristic to this sample is shown in Fig. 112, while the results of the quantitative EDX analysis are summarized in Table 13. We could see the increase of the Zr compared to the other samples. The amount of the C and that of the O were also relatively low, B could not been found. In some grains Fe, Cr or Ni were enriched beside Zr. Probably these filings were originated mostly from the guide tube having only small amount of O. Fe, Cr and Ni were originated from the control rod stainless steel cladding.

No. of grain	O (m %)	Cr (m%)	Fe (m %)	Ni (m %)	Zr (m %)
1	2.3 ±0.5	0	0	0	97.7 ±0.5
2	2.6 ±0.8	0	0	0	97.8 ±3
3	2.2 ±0.5	0	2.9 ±2.2	0	95 ±2.2
4	2.3 ±0.5	0	8.8 ±2.3	0	88.9 ±2.3
5	2.3 ±1.1	9.6 ±8.6	6.4 ±3.1	0	81.7 ±8.3
6	20.8 ±3.8	0	0	0	79.2 ±3.8
7	2.6 ±1	6.7 ±8.2	13.7±3	0	77 ±7.3
8	2.3 ±0.8	7.1 ±6.7	16.4 ±2.7	5.7 ±1.4	68.4 ±5.4
9	2.6 ±0.4	0	20.2 ±2	9.8 ±1.4	67.4 ±2
10	4.4 ±1.2	11.1 ±9.3	31.7 ±4.3	0	52.8 ±6

Table 12 Elemental composition of some grains in sample No. 200

No. of grain	C (m %)	O (m %)	Cr (m %)	Fe (m %)	Zr (m %)
1	0	2.1±1.3	0	0	98±1.3
2	0	2.1±0.6	0	0	97.9±0.6
3*	0	2.4±0.5	0	0	91.7±1.7
4	0	6.7±0.9	0	5.2±3.1	88.1±3
5	1.2±1.7	1.7± 0.9	21.6± 5.8	0	75.5±5.8
6	2.4±2.3	5.5±0.8	0	0	92.1±2.4
7	0	4.1±0.6	0	0	95.9±0.6
8	0	3.9±0.7	0	0	96.1±0.7
9	0	0	0	5.5±3.2	94.5±3.2
10	0	6±1.4	0	0	96.4±5

Table 13 Elemental composition of some grains in sample No. 235
Note: * This grain probably contained 5.9±1.7 m % Nb.

8.4.4 Elevation 460 mm

In this sample we found several Fe-Cr-Ni rich grains, however there were a lot of Zr mostly in oxidized state. One grain proved to be rich in U. As accompanying elements Zr, O and probably C were present. C could originate from the adhesive tape despite to the fact that we tried to magnify the details to be analyzed as much as possible.

Table 14 summarizes the results of the quantitative EDX analysis which was done at 15 kV accelerating voltage and by using 3 nA beam current. Fig. 113 shows EDX spectrum typical for an aggregate containing the components of steel. We found some grains, where W and sometimes Mo could also be detected.

Table 15 contains the results of the quantitative EDX analysis for some examples of such grains, while Figure 114 shows the EDX spectrum for one of them. It can be seen from the data in Table 15, that the elemental composition of these grains or aggregates of grains showed significant variation among the various grain. It is obvious because the larger grains were aggregates, not individual grains. The O content was rather low in these grains, they were probably metallic ones.

Element (m %)	1. grain	2.grain	3.grain
C	6.50±0.71	3.45±0.59	1,87±0.43
O	9.15±0.56	4.76±0.51	2.18±0.37
Cr	12.19±0.54	13.11±0.5	15.06±0.54
Mn	1.52±0.44	0	1.68±0.43
Fe	44.06±0.99	47.45±0.94	60.97±1.03
Ni	8.22±0.75	7.7±0.72	11.55±0.77
Zr	22.36±0.89	23.52±0.84	4.19±0.57
Mo	0	0	1.96±0.36

Table 14 Results of some quantitative EDX measurements
in grains containing steel components

Element (m %)	1.grain	2.grain	3.grain
C	1.73±0.38	3.24±0.48	1.33±0.4
O	0	2.40±0.40	4.02±0.46
Cr	4.77±0.39	13.94±0.51	5.43±0.39
Mn	0	1.23±0.4	0
Fe	36.47±0.78	54.24±0.96	16.93±0.65
Ni	3.11±0.62	9.94±0.73	3.35±0.62
Mo	0	2.58±0.55	0
Zr	0	0	5.09±0.76
W	53.92±0.85	12.43±0.65	63.85±1.0

Table 15 Results of the quantitative EDX analysis for some W-containing grains

We found some grains, which had some amounts of Fe and Cr, but more amounts of Zr and Nb. Table 16 summarizes the results of the quantitative EDX analysis for such grains.

Element (m %)	1.grain	2.grain
C	12.06±1.11	14.02±1.1
O	17.84±1.0	18.93±0.99
Cr	1.59±0.36	4.94±0.42
Fe	10.81±0.67	3.69±0.49
Zr	27.77±1.18	38.12±1.21
Nb	29.93±1.25	20.31±1.18

Table 16 Results of the quantitative EDX analysis for Zr-Nb containing grains

The grain enriched in U contained Zr, O and probably C. We found a lot of grains with high amounts of Zr and O, in some cases small amounts of Fe was also present. These grains were probably ZrO_2.

By summarizing the results of control rod melt measurements, we could state the followings:

- The melt in the gap between the guide tube and control rod contained mainly Zr and some stainless steel components.
- High content of steel components was found in the sample taken from 460 mm position. These elements were enriched in grains or aggregates, which contained more or less amounts of Zr and in some cases also Nb.
- Tungsten was found in some grains together with some components of steel.
- We could not find boron in these filings.
- Oxygen was present mostly together with Zr, probably in form of zirconium oxide.
- The component elements of the steel were probably mostly in metallic form, because such grains contained only small amount of oxygen.

9. EXAMINATION OF AEROSOL SAMPLES

Aerosol samples were taken during the test using 10 impactors (Table 17). The samples were analyzed to determine the elemental composition of collected materials. Additional samples were taken from the top of the cooler, close to the outlet junction of the test section.

Valve	Opening time [s]	Closing time [s]	Period
Impactor No. 1	15068	15128	Power ramp
Impactor No. 2	16193	16253	Control rod degradation
Impactor No. 3	16254	16314	Control rod degradation
Impactor No. 4	16315	16375	Control rod degradation
Impactor No. 5	16898	16958	Bundle rod degradation
Impactor No. 6	16959	17019	Bundle rod degradation
Impactor No. 7	17020	17080	Bundle rod degradation
Impactor No. 8	17081	17141	Cool-down
Impactor No. 9	17142	17202	Cool-down
Impactor No. 10	18073	18133	Cool-down

Table 17 Impactor valve positions during the CODEX-B4C test

9.1 Aerosol samples and applied methods

Two stage impactors were used in the experiment constructed in similar way as in the CODEX-AIT-1 experiment [11]. They had two collector plates and one quartz fiber filter (see Fig. 115). The two plates were applied for studies made by scanning electron microscope, while the fiber filter was used for spark source mass spectrometry. Ten impactors were used as specified in Table 17. Besides the impactors an impaction plate made of nickel was also applied for aerosol collection. The precipitate found on the top of the cooler unit was also investigated. Therefore the following types of aerosol samples were studied:

1. collector samples,
2. filters,
3. Ni impaction plate,
4. precipitate on the top of the cooler.

Samples for microscopic studies were used as received. No carbon or other material was necessary to evaporate to the surface of them. However electric charging was found sometimes especially for highly packed collector plates.

For morphological studies (size, shape of the particles and their aggregates) a Philips SEM 505 type of scanning electron microscope (SEM) was used. Generally 20 kV accelerating voltage and a few times 10^{-10} - 10^{-9} A specimen current were applied. Backscattered electron images were produced by a Centaurus backscattered detector produced by K. E. Development Limited. Digital secondary (SE) and/or backscattered (BE) images were stored in a computer with a resolution of 512x512 pixels. Elemental analysis of individual aerosol particles and aggregates of them was performed by an energy disperse microanalyser (EDX) - a LINK AN 10/55S type was used.

Spark source mass spectrometric (SSMS) method was used for the elemental analyses of some samples in frame of post-test investigations. We have in our laboratory an AEI-MS702R type double focusing mass spectrometer. The high sensitivity of the instrument made it possible to measure elemental concentrations down to 10 ppbw even from samples containing not more than 0.01 μg of the isotopes to be investigated. The basic principle of the method is, that between two solid samples a spark is generated by pulsed high frequency high voltage, in the spark the material of sample is evaporated and ionized. The ions are accelerated by some 10 kV-s and are separated according to their mass by electrical and magnetic deflection fields. The mass separated ions are detected by sensitive electronic ion current measurement or by appropriate photoplates. If the detector is a photoplate after development the optical density of lines are measured by appropriate microdensitometer. Even if the method is sophisticated and time consumable, the extreme high sensitivity determination of many elements in one run made it economic. The sample pair for a measurement ought to be two pieces of solid rods with 1-2 mm diameter and 10 mm lengths. At metals it can be worked out from the samples. The inorganic powder samples are mixed with ultrahigh purity graphite and pressed to dimension mentioned before. A further advantage of simple sample preparation, that it needs no chemical processing with high purity chemicals and laboratories. The samples to be investigated in frame of the present work however contained substantial amount of boric acid components. They have a large vapor pressure at higher temperature and during the sparking it would destroy the electrode. It had to be eliminated before the sample preparation. It was achieved by evaporating twice 10 ml abs. ethanol from the sample. In this case the boric acid compounds are going away as triethylborate. The high purity ethanol does not contain any metallic components with disturbing effect.

9.2 Morphology of the aerosol particles

There were a lot of aerosol particles and aggregates at almost every collector plates. SEM images made at small magnification prove this statement. In Fig. 116 digital SEM images for some aerosol samples can be seen. At the beginning of aerosol collection - i.e. in the preheating period - a lot of Zr-rich fibers were found. They are originating probably from the insulating material of the bundle. At the high temperature region of the experiment individual aerosol particles and aggregates were found. The bigger structures - Zr-rich and silicate fibers and aggregates of various aerosol particles - were settled on collector plates marked by B, while the smaller ones - mostly individual particles were found on the surfaces of collectors marked by D. This is illustrated by the backscattered electron images of impactor samples No. 5 (see Fig. 117).

The image made from aerosol sample No. 5B shows mostly fiber-like structures with very few individual aerosol particles. It can also be recognized that the surfaces of the fibers are covered by small particles – probably ZrO_2. The image made of aerosol collector No. 5D shows much less fibers and larger amount of individual aerosol particles. The size of the individual aerosol particles was less than 5 μm, generally between 1 and 3 μm. The shape of them was globular and slightly elongated. Regions less bright than the individual particles were aggregates of small particles.

In the cooling-down phase of the test the amount of aerosols was increased. There were large areas and platelets composed of smaller particles. This is illustrated by digital SEM images made from aerosol samples No. 8 D and 9D, respectively (see Fig. 118).

The individual particle size is not easy to establish due to the high degree of aggregation. However in some parts it can be done - the individual aerosol particle size was generally between 1 and 3 μm, but there were somewhat larger particles, too.

The SEM studies of the Ni impaction plate (three pieces cut from the plate) revealed that there were a lot of aerosol particles settled mostly in form of layered platelets, as it can be seen in the digital SEM image of Fig. 119.

9.3 ED studies of the aerosol samples

Uranium was found on collector No. 5 sampling during the cooling down phase of the test. Uranium was present in form of individual particles with a size varying between 1 and 10 μm. The smaller U-rich particles had globular shape, while the larger ones were elongated. Their length was in the range of 5-10 μm, while the width was about 3-5 μm. Typical U-rich particles are shown in Fig. 120.

The image seen on the right hand side of Fig. 120 has six uranium rich particles with elongated forms. The greatest number of U-rich aerosol particles was found on collector No. 5B, but they were found also in the cooling down period. Results of the standardless quantitative analysis are shown in Fig. 121.

Uranium was found also on the surface of the Ni impaction plate. There were small sized (about 1-2 μm) U-rich particles with some larger ones. Typical example is shown in Fig. 122.

From the other elements wolfram and zirconium were found in the largest quantities. Wolfram was present in small particles formed as lamellas during cooling down. They were present in larger amount on the surfaces of collector plates marked by D. Results of the standardless quantitative analysis of typical W-rich aerosol particles can be seen in Fig. 123. The elements detected in W-rich particles/aggregates are: Zr or Nb and in smaller quantities U, Cr, Mn and Fe.

W Ta, Zr, Nb and U were also detected. In some particles Ta was the main component, while in others it was found together with Zr and some amount of U. Typical results of standardless EDS analysis can be seen in Figure 124.

Zirconium was present in several forms, namely:

1. long fibers: mostly in the pre-heating period
2. individual particles: from the high temperature region of the test
3. accompanying element of W present in large lamellas on the Ni plate.

Mo was detected in some particles generally alone, sometimes with Si coming probably from the plate covering the collectors. Mo was found in the high temperature region and also in the cooling down phase of the experiment.

Nb was found together with Ta or W and Zr. These aerosol particles were found in the cooling down phase of the experiment. Nb is originated probably from the cladding or shroud.

Component elements of the stainless steel (Fe, Cr, Mn, Ni) were detected frequently as elements accompanying some others like Ta, W, Zr, U, sometimes Fe-Cr or Cr-Mn-Fe-rich particles. Results of the standardless EDS analysis for typical aerosol particles are shown in Figure 125.

On the surface of the Ni impaction plate the following elements were detected: W, Zr, Ta, U, Fe, Cr, Mn. Digital SEM images showing some of these elements are presented in Figures 119, 122 and 126. The most frequently found element was the W, which was present probably in oxide form, too. It was detected also in the small dark regions between brighter ones of the BE images of the Ni impaction plate.

The large lamellas were enriched in W. It is originated probably from the thermocouples and from the heating rods. This latter could be proved by the presence of small amount of U.

9.4 Mass spectrometric analysis

The following samples have been investigated with mass spectrometric analysis:

- precipitation on top of cooler,
- Ni collector plate in top of cooler,
- precipitations on filters of impactor.

9.4.1 Precipitation on top of cooler

After the experiment about 10 g light blue precipitation was found on the top plate of the cooler of outlet gas. The chemical analysis resulted, that it contained:

- 75 % boric acid,
- 1 % Zr, 0.7% Fe, 0.5 % Al, 0.2 % Si, 0.2 % W
- 40 mg U (in 10 g)

The metallic elements in the 2nd row are given as % of metallic elements. Of course all of them were in oxide form. The boric acid component (certainly as HBO_2) originated from the oxidation of boron carbide, the Zr and Fe from construction material of bundle, the Al and Si from thermal isolation at the top of bundle, the W from tungsten heating rods. Even some Re and Rh appeared from the thermocouples.

The 40 mg uranium, presumably escaped in the form of UO_3 represent ca $3.8*10^{-3}$ N liter uranium oxide species. The amount of gas streaming through the bundle in the high temperature escalation phase was 660 N liter. (7.5 minutes with flowing rate of 1.5 g/s argon and 0.5 g/s steam or hydrogen after the chemical conversion.) It results an average of $5.8*10^{-6}$ bar partial pressures of UO_X species. This vapor pressure in the hydrogen-steam atmosphere can be formed at the range of 1600-1700 °C. The highest temperature in the bundle was at about 2000 °C. Certainly the vapor pressure of UO_X species was reduced for this value at the top area of the bundle. No thermocouple measurement was at that height.

9.4.2 Precipitation on Ni collector plate in top area of cooler

The Ni collector plate was placed in the upper space of the cooler, just opposite to the outlet tube of bundle unit. It was a 0.1 mm thick sheet placed on the internal wall of the tube like cooler top. The gas leaving the bundle left precipitations on this plate. Two pieces of about 15x15 mm dimensions were cut out from the plate and rolled up to 2 mm thick electrodes. They were used for the spark source investigations. The sparking was made between the ends of electrodes resulting ions from the material of the Ni plate and the precipitations. The Ni-64 line was used as reference inner standard, it is a low abundance isotope and could be applied for this purpose. Extrapolating for the whole surface of Ni plate the whole amount of uranium was found to be 0.1 mg.

9.4.3 Deposits on the impactor filters

The sampler impactors were used mainly in the escalation. The impactors were weighted before and after the test. Each sampling was performed over 1 minute by pumping through 1 liter of gas from the top area of cooler. The samplers No. 2, 3 and 4 were activated just after each other in the period of control rod degradation, while those of from No. 5 to 9 during the bundle degradation and cool-down. The first and the last samplers were activated before and after the main phase of the test. The increase of their masses is plotted in Fig 127. The large weight increase at Sampler 10 is originated certainly from the fact, that the bundle was at high temperature enough to feed the cooling gas with the very volatile metaboric acid.

The mass increases were substantial. Large part of deposits was boron compounds, certainly HBO_2. No effort was made to make an exact identification of their chemical form, but on basic chemical knowledge and their behavior in some chemical processes during sample preparation satisfactorily support this assumption. During the sample preparation for SSMS investigations the boric acid compounds had to be eliminated. The sample preparation was performed as described in chapter 9.1. The results are summarized in Table 18.

The most important results are the uranium concentrations. The amount of uranium carried in oxide form by the gas leaving the bundle and collected on Ni plate and on impactor collectors both resulted about 0.1 mg total uranium for the outlet gas. (This regards only for the gas or fine aerosol component. The sample gas flow was about 1% of the total gas flow of argon, steam and other gas components leaving the bundle). The results calculated from samplers' uranium content were extrapolated by using the sampling gas volumes and the total gas stream. It is interesting, that the uranium mass collected by the Ni plate in the top of the cooler was about the same value as that, calculated from the impactor results on the way mentioned. It seems so, that the Ni plate collected the molecular and fine aerosol fraction of uranium oxides. Moreover the amount of uranium mentioned above was in good correlation with a calculated value of uranium oxides volatilized. The oxygen partial pressure necessary for the calculation was assessed from the thermal dissociation of water assuming, that hydrogen was also present from the H_2O - B_4C reaction. The hydrogen generated by the steam - boron carbide reaction was taken into account as well.

The 0.1 mg U in the UO_X species – if they were in gas form – represents 1.10^{-5} Nliter of them, in the 660 liter carrier gas their average partial pressure was ca $1.5*10^{-8}$ bar. The outlet gas temperature was found to be 1200 °C. Even if we calculate with a low conversion of steam to hydrogen (<10 %) the oxygen partial pressure from the water thermal dissociation is too low to explain this UO_X partial pressure. (The $P(O_2)$ ought to be above 10^{-8} bar, the steam dissociation could result less than 10^{-10} bar at this temperature.) Certainly at the higher temperature area formed larger UO_X partial pressure do not equilibrated to the 1200 °C value. Aerosols with small dimensions may be responsible for the higher uranium transportation. 40 mg U was measured in the precipitate and 0.1 mg U on the Ni plate. The integrated values of the U content in the outlet gas was estimated as 0.008 mg, considering the U content on the impactors, the total flowrate and the operating period of impactors No. 7-8-9. According to the above values most of the released U deposited on the cooler surface (~500 ^oC) and only very small amount reached the room temperature impactors and the environment.

Sample No.							
	4	**5**	**6**	**7**	**8**	**9**	**10**
Element	[μg]	[μg]	[μg]	[μg]	[μg]	[μg]	[μg]
Al			800	80	120	37	22

Si			2600		8000	8200	
K		4	12	5	60	3	1.3
Ca		5	80	20	9	6	3
Cr	40	31	220	65	150	170	35
Mn	4	105	600	100	200	50	9
Fe	11	50	600	190	280	73	26
Ni	1.6	5	35	20	40	35	23
Cu	1.8	4	25	18	35	30	5.5
Zn	23	4	3	17	2.5	80	12
Zr	130	1.5	7	3	3	18	4.5
Nb		2	20	10	18	20	2
Mo					0.5		
Sn		1.2	20	9	55	38	2.5
Cs		0.3			2		
Ba		5	0.4	0.4	6	+	0.3
Ce					0.2		0.2
Nd		4	3	2	4	+	3
Hf						5	
W		1	40	14	110	360	2.5
U				0.03	0.1	0.2	

Table 18 Results of aerosol impactor examination

10. CONCLUSIONS

The CODEX-B4C experiment provided important information on the behaviour of VVER fuel and control rods under severe accident conditions [12], [13]. The experimental conditions were to simulate a severe accident scenario in a VVER-1000 type reactor. The low temperature control rod degradation period was extended in order to produce more details of degradation process. The high temperature escalation above 2000 ^{o}C was performed in steam atmosphere without additional power increase. Slow cooling down took place in steam atmosphere.

The test indicated no CH_4 formation under high temperature oxidation of B_4C pellets. The loss of geometry started with the melting of the steel cladding of the control rod and it accelerated the fuel rod degradation process. High release of aerosols was observed during the oxidation of core components in steam, the aerosol release correlated with steam flowrate. Temporary heatup was observed in the cooldown phase as a result of local oxidation. The first visual examiantion of the bundle showed strong oxidation and degradation of shroud and the control and fuel rods.

The recorded on-line data have been collected into an experimental database and are available for model development and code validation purposes. The database includes the commissioning test results as well, which could be used for estimation of system heat losses.

The post-test examination of the CODEX-B4C experiment focused on two items:

- detailed investigation of the bundle, including radiography, metallography of 13 horizontal cross sections, analysis of the control rod degradation,
- study of released aerosol samples collected on impactors and cooler internals, including SEM, EDX and SSMS analysis.

The in-situ radiography application indicated that the degradation of the bundle took place mainly in the high temperature (~2000 ^{o}C) period of the test. However the fuel rods remained in their original position.

Red – iron-oxide containing – melt was seen between the fuel rods, forming blockage in the channels and fixing the rods to each other. This *sticking effect* was not observed in earlier CODEX tests without large steel components in the bundle, in which more intense fragmentation was seen. The oxidized shroud was very brittle in the upper half of the bundle and could be removed easily from the bundle. After visual examination it was taken back and filled up with epoxy together with the bundle.

According to metallographic examination the Zr cladding and shroud in the upper part of the bundle were completely oxidized. This observation explains the escalation during the cool-down phase: the temperature started to decrease only after the complete oxidation of the high temperature Zr in steam atmosphere.

The control rod completely disappeared above 335 mm elevation, which means that ~45% of the B_4C was missing. Most of the B_4C was oxidized, as ~40% of equivalent carbon was found in the released CO and CO_2. Part of the stainless steel cladding melted and dissolved part of the Zr guide tube. The total volume of the relocated melt in the lower part of the control rod was ~3,5 cm^3 and contained steel and cladding components. The mass of dissolved Zr at ~1500 ^{o}C was estimated as 1-2 times of molten steel. No boron was found in the melt.

Detailed studies were performed on various aerosol samples collected in the experiment. Large amount of blue precipitates was observed on the top of the cooler, containing mainly boron released as a results of control rod oxidation. Uranium containing particles were found on impactors activated during the high temperature region of the test. Uranium was found on the surface of the Ni impaction plate as well. U release was proportional to partial pressure of UO_3, the total U release was about 40 mg. Beside uranium a lot of tungsten, zirconium furthermore iron, chromium, nickel, tantalum, molybdenum, niobium, yttrium, hafnium were detected in form of small particles and/or aggregates of them. Results gained by SEM + EDX and SSMS were found to correlate with each other.

ACKNOWLEDGMENTS

The CODEX-B4C test was performed in the COLOSS (Core Loss During a Severe Accident) project of the Fifth Framework Programme with the financial support of the European Commission (contract number FIKS-CT-1999-00002).

REFERENCES

[1] L. Maróti,"VVER Fuel under Extreme Conditions", Transactions of TOPFUEL '95, vol. 1., 1995, pp. 253-264

[2] L. Maróti, "Chemical Interaction between VVER Core Components under Accidental Conditions", Nucl. Eng. and Design vol. 172, 1997, pp. 73-81

[3] Z. Hózer, L. Maróti, B. Tóth, P. Windberg,"VVER-440 Core Degradation Experiment" Proceedings of NURETH-8, Vol. 2, Kyoto, 1997, pp. 605-611.

[4] Z. Hózer, L. Maróti, I. Nagy, P. Windberg: CODEX-2 Experiment: Integral VVER-440 Core Degradation Test, KFKI-2000-02/G, 2000

[5] Z. Hózer , L. Maróti ,P. Windberg, "Quenching of High Temperature VVER Bundle", Proceedings of NURETH-9 on CD, San Francisco, 1999, ISBN 0-89448-650-0

[6] L. Maróti, I. Nagy, P. Windberg: Quenching of Highly Oxidized VVER Type 7-Rod Bundle, 3rd Quench Workshop, Karslruhe, 3-5 December 1997

[7] Sheperd I, B. Adroguer B, Buchmann M, Gleisberg O, Haste T, Hofmann P, Hózer Z, Hummel R, Kaltofen R, Knorr J, Kourti N, Leonardi M, Oriolo F, Schneider R, Maróti L, Matus L, Schanz G, Windberg P. Oxidation Phenomena in Severe Accidents, Proceedings of FISA-99, Luxemburg 29 November - 1 December 1999, pp. 193-201

[8] A Volchek, Yu Zvonarev: Pre-test calculations of the CODEX bundle tests with ICARE/CATHARE code, SAM-COLOSS-P04, NSI RRC KI 2283, March 2001

[9] Gy Gyenes: Pre-test calculation of the CODEX-B4C test, SAM-COLOSS-P013, Budapest May 2001

[10] E. Virtanen: Pre-test calculation of CODEX-B4C test, SAM-COLOSS-P014, June 2001

[11] Z. Hózer, P. Windberg, I. Nagy, L. Maróti, L. Matus, M. Horváth, A. Pintér, A. Czitrovszky, P. Jani: CODEX-AIT-1 Experiment: Core Degradation Under Air Ingress, KFKI-2002-02/G,

[12] B. Adroguer et al.: Core Loss During a Severe Accident (COLOSS), Proceedings of FISA-2001, pp. 247-260, Belgium 2002, ISBN 92-894-3455-4

[13] B. Adroguer et al.: Core loss during a severe accident (COLOSS), Nucl. Eng. Design, 221 (2003) pp. 55-76

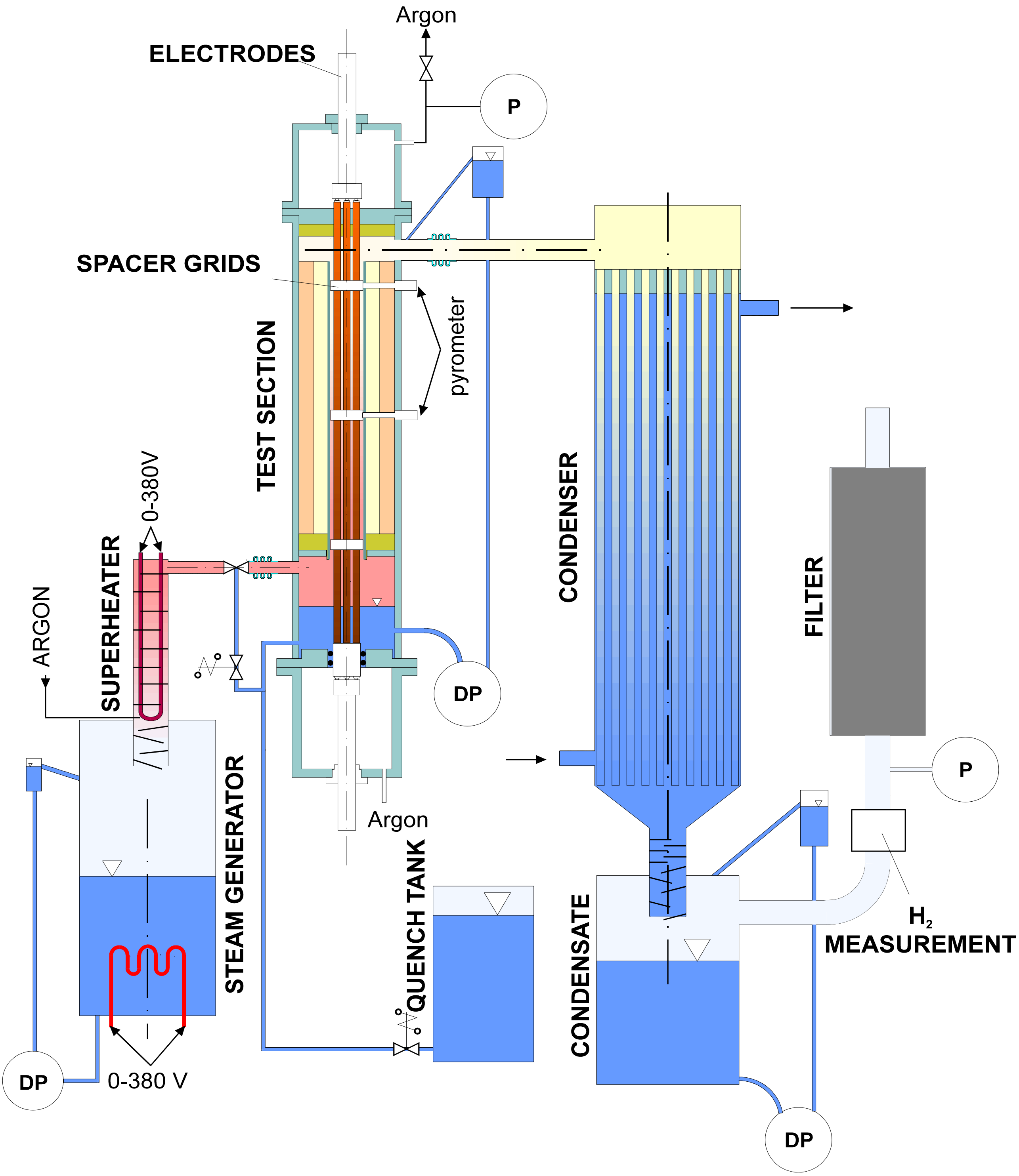

Fig. 1 Scheme of the CODEX facility

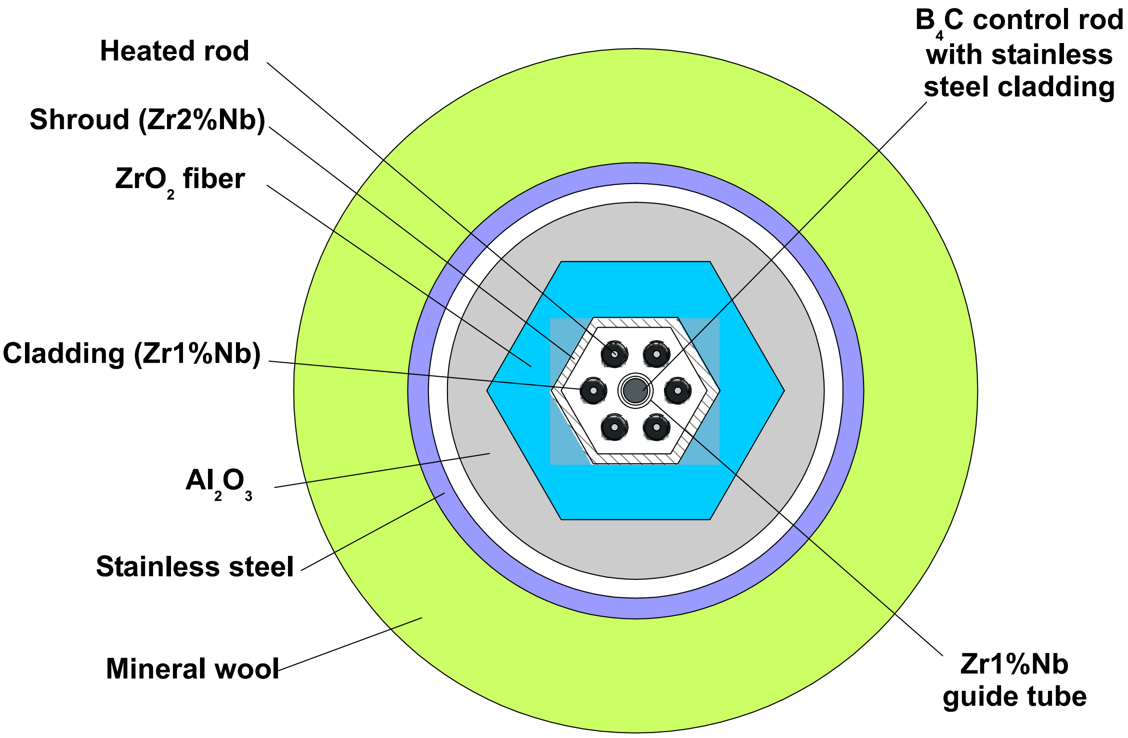

Fig. 2 Horizontal cross section of the CODEX-B4C bundle

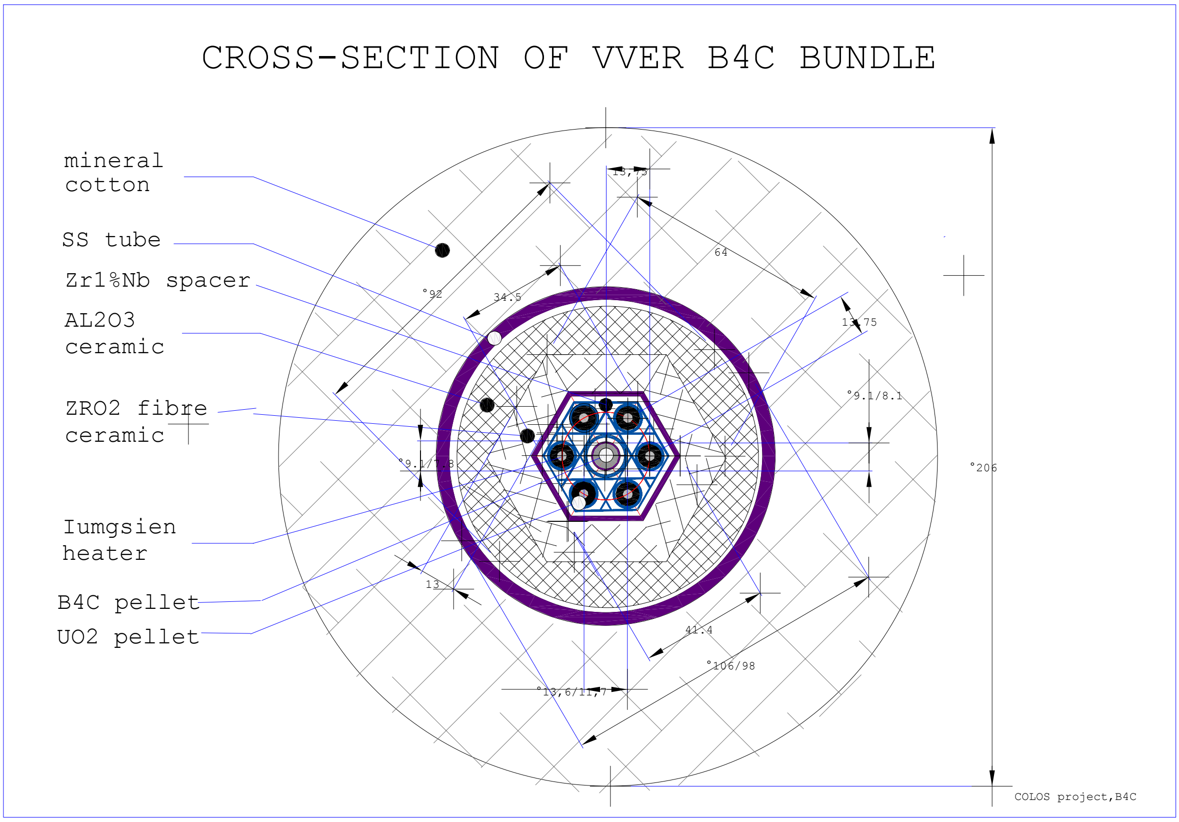

Fig. 3 Main geometrical parameters of the CODEX-B4C bundle

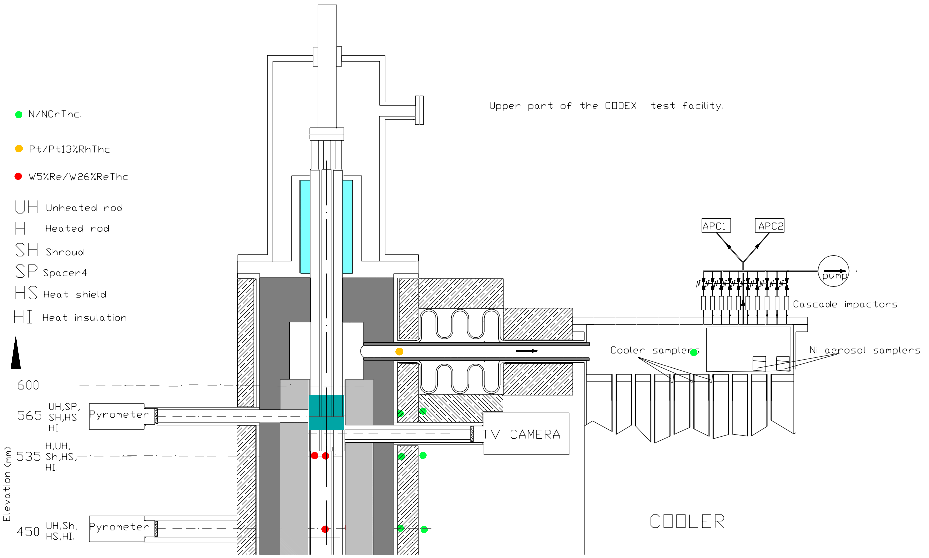

Fig. 4 Connections for aerosol sampling

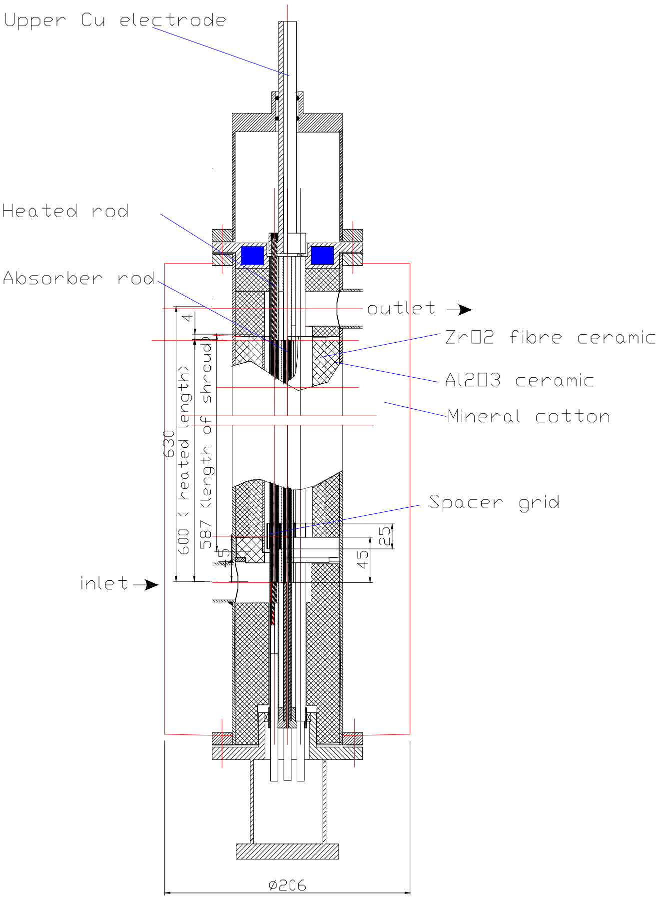

Fig. 5 Test section of the CODEX facility

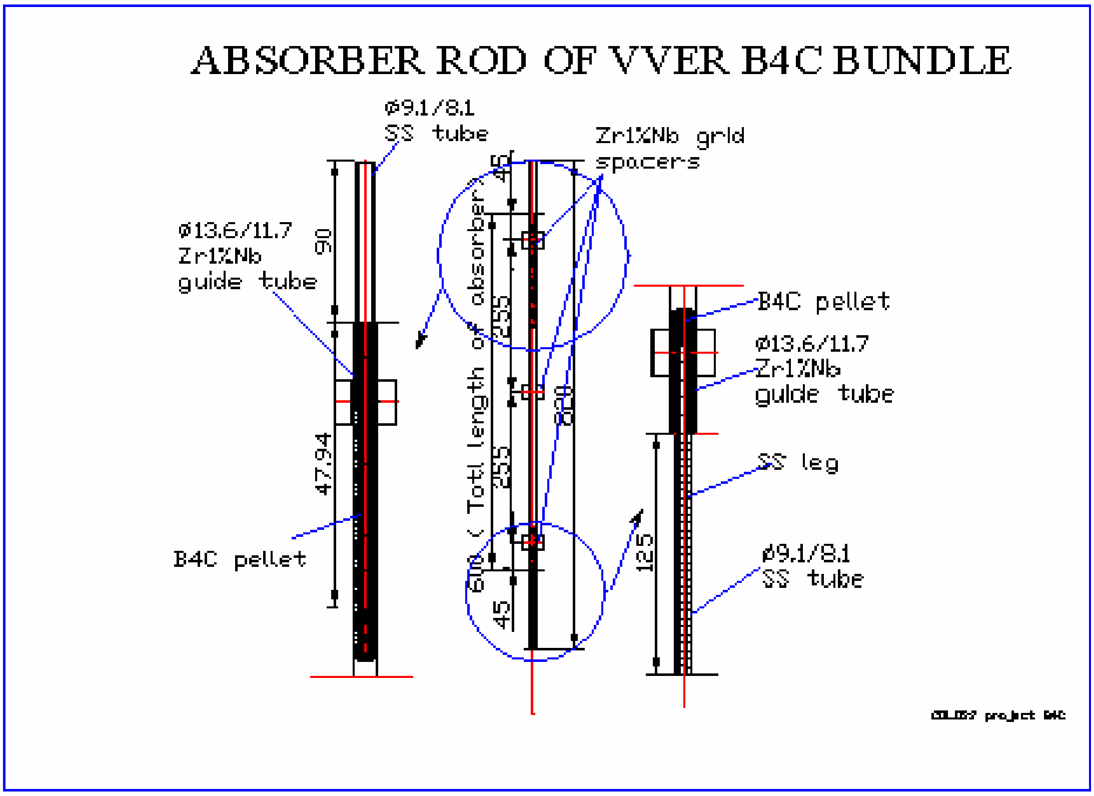

Fig. 6 Absorber rod of the CODEX-B4C bundle

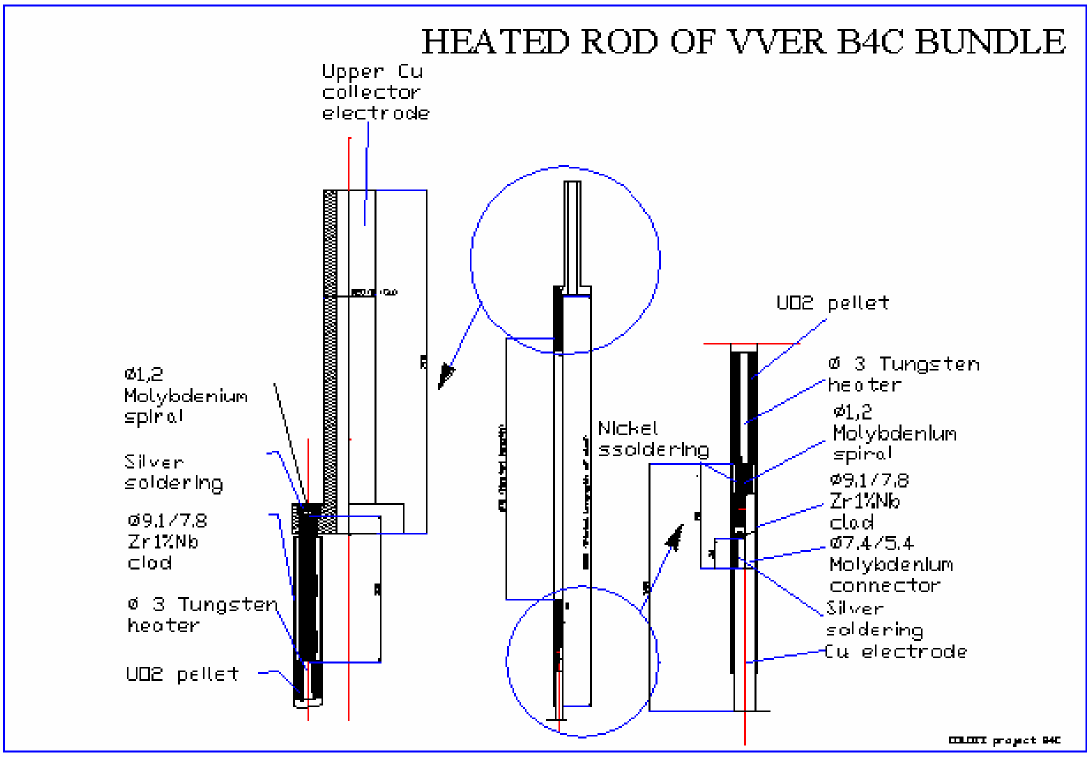

Fig. 7 Central rod of the CODEX-B4C bundle

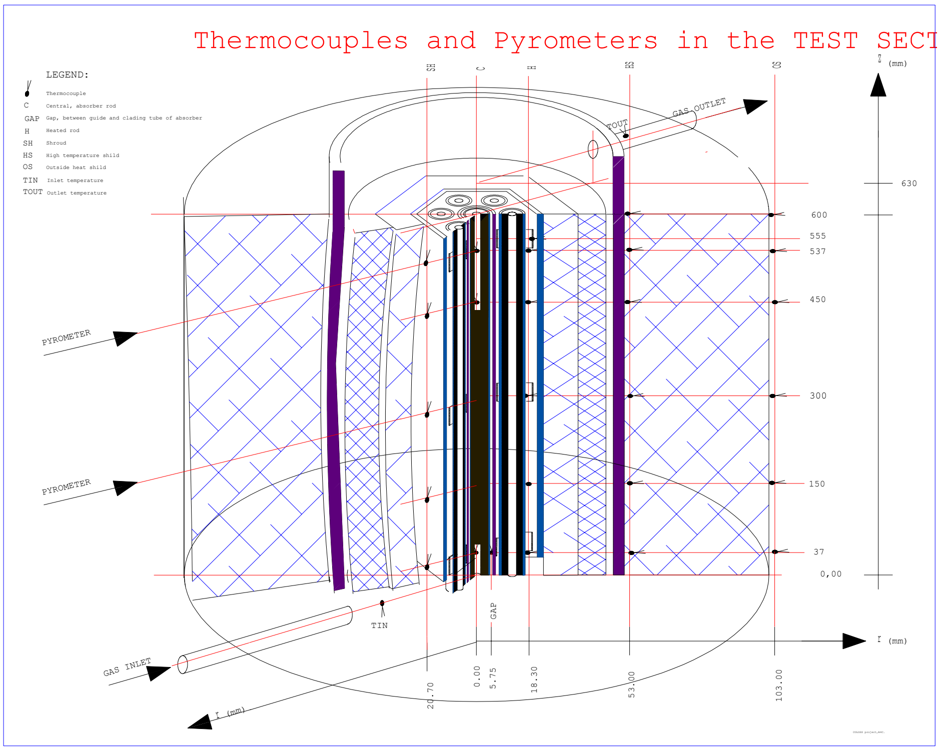

Fig. 8 Location of thermocouples and pyrometers in the CODEX-B4C bundle

TEMPERATURE MEASUREMENTS
in central **B4C filled rod** and in the **gap**
and on the **guide tube** of CODEX-B4C
bundle

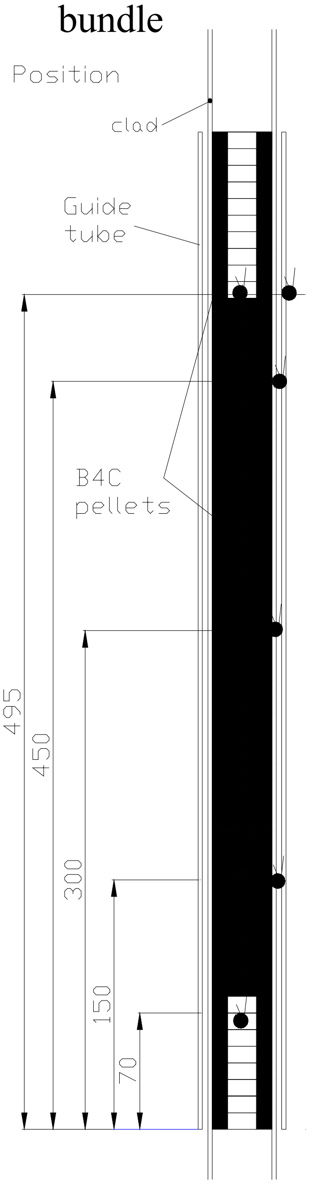

Position	Type of thermocouples	Identification
495	WRe26%/W5%Re,Cr/Al	C495, GD495 (on guide tube)
450	Cr/Al	GP450 (in the gap)
300	Cr/Al	GP300
150	Cr/Al	GP150
70	Cr/Al	C70

TCentrodB4C

Fig. 9 Placement of temperature measurements in the central rod

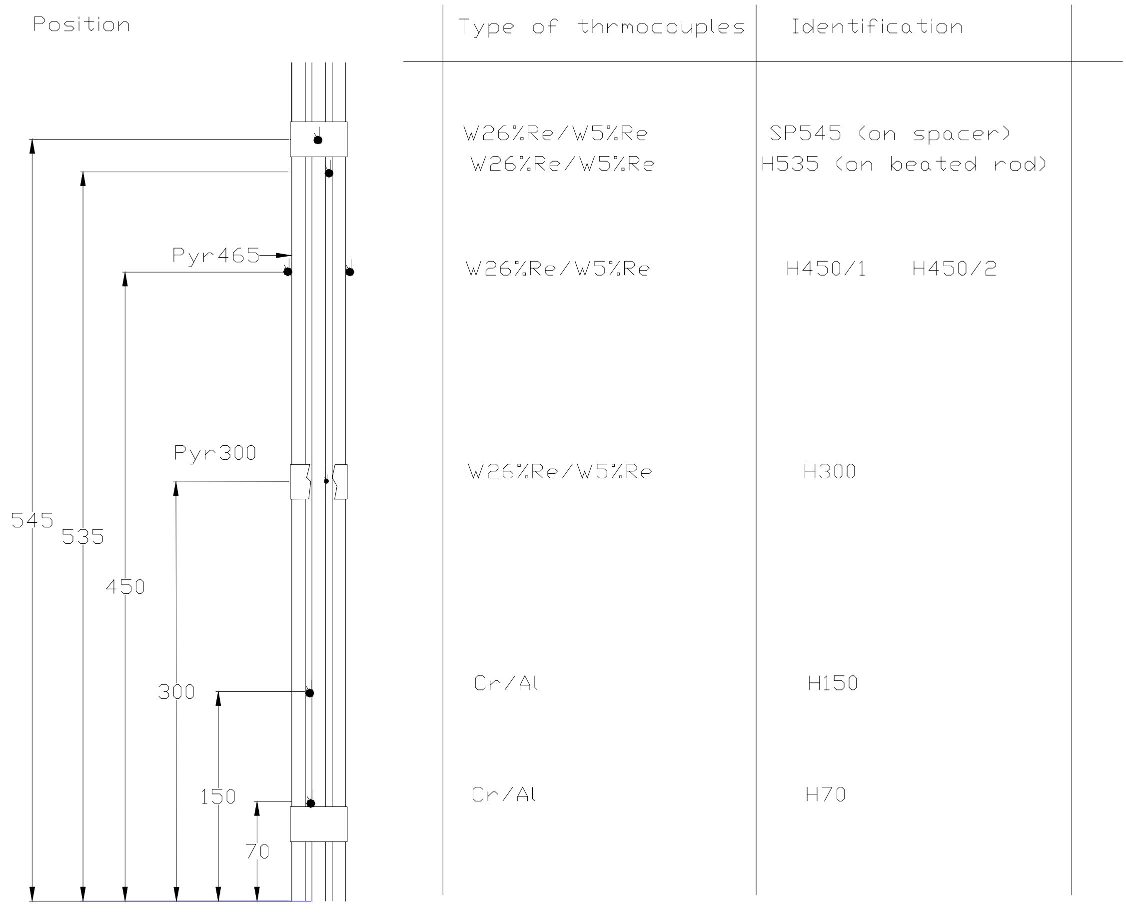

TEMPERATURE MEASSUREMENTS
on **heated rods** of CODEX-B4C bundle

Type of thrmocouples	Identification
W26%Re/W5%Re	SP545 (on spacer)
W26%Re/W5%Re	H535 (on beated rod)
W26%Re/W5%Re	H450/1 H450/2
W26%Re/W5%Re	H300
Cr/Al	H150
Cr/Al	H70

Fig. 10 Placement of temperature measurements on the heated rods

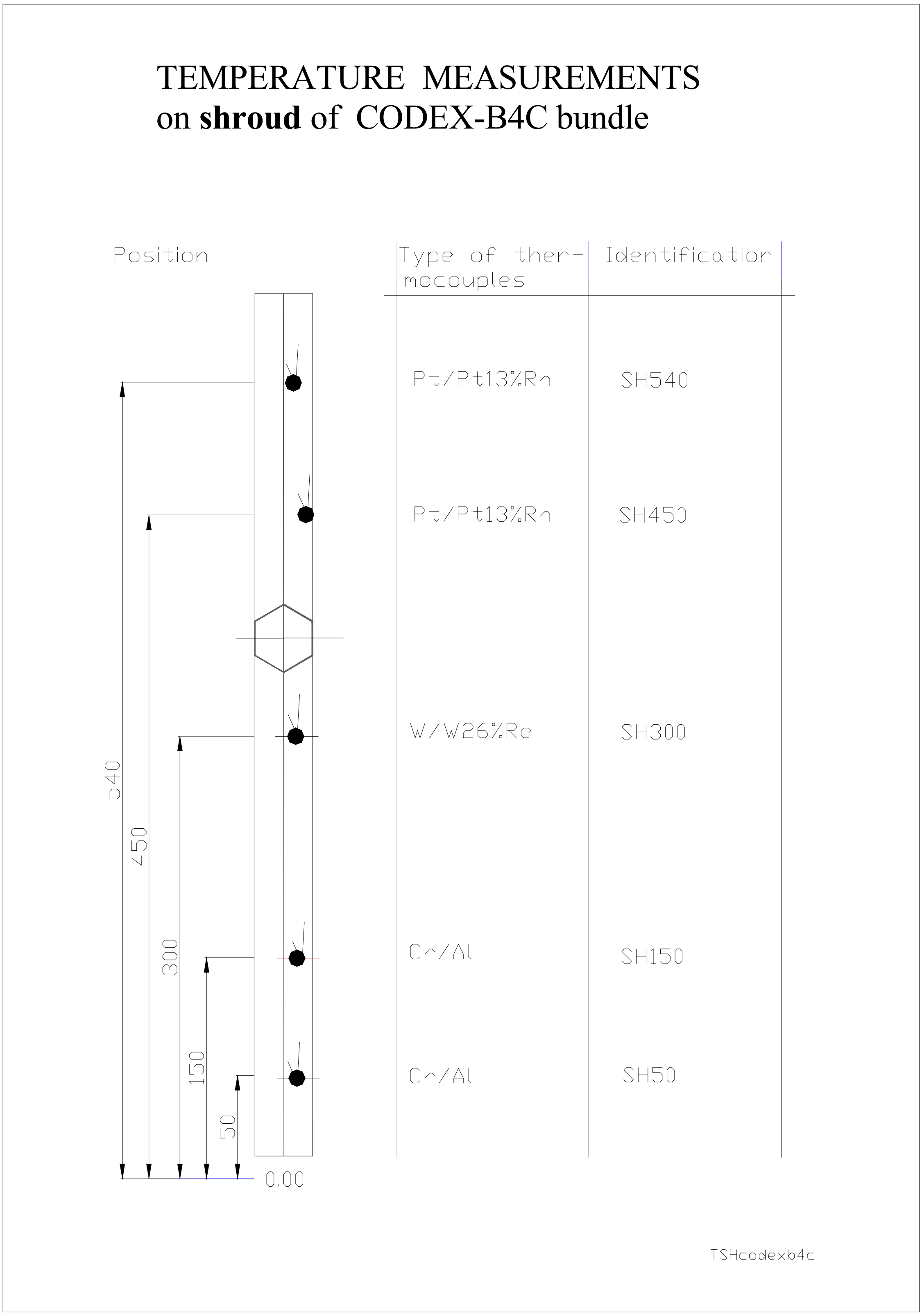

TEMPERATURE MEASUREMENTS
on **shroud** of CODEX-B4C bundle

Position	Type of thermocouples	Identification
540	Pt/Pt13%Rh	SH540
450	Pt/Pt13%Rh	SH450
300	W/W26%Re	SH300
150	Cr/Al	SH150
50	Cr/Al	SH50

Fig. 11 Placement of temperature measurements on the shroud

TEMPERATURE MEASUREMENTS
on **heat shield** and **outside of heat shield**
of CODEX-B4C bundle

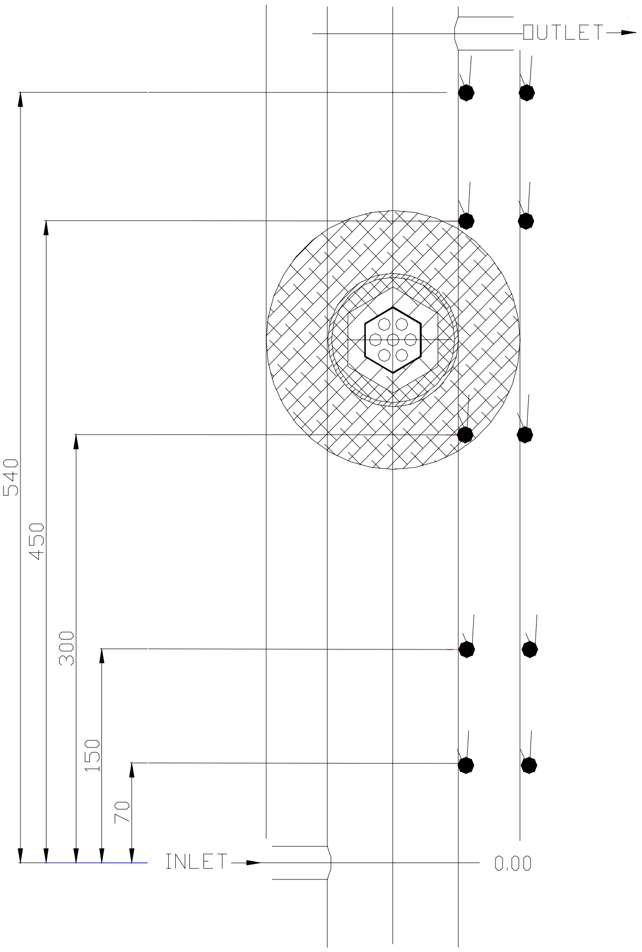

Type of thermocouples	Identification
Cr/Al, Cr/Al	HS540 OS540
Cr/Al, Cr/Al	HS450 OS450
Cr/Al, Cr/Al	HS300 OS300
Cr/Al, Cr/Al	HS150 OS150
Cr/Al, Cr/Al	HS70 OS70

THScodexb4c

Fig. 12 Placement of temperature measurements on the heat shields

TEMPERATURE MEASUREMENTS
of **system gas flow** of CODEX-4C bundle

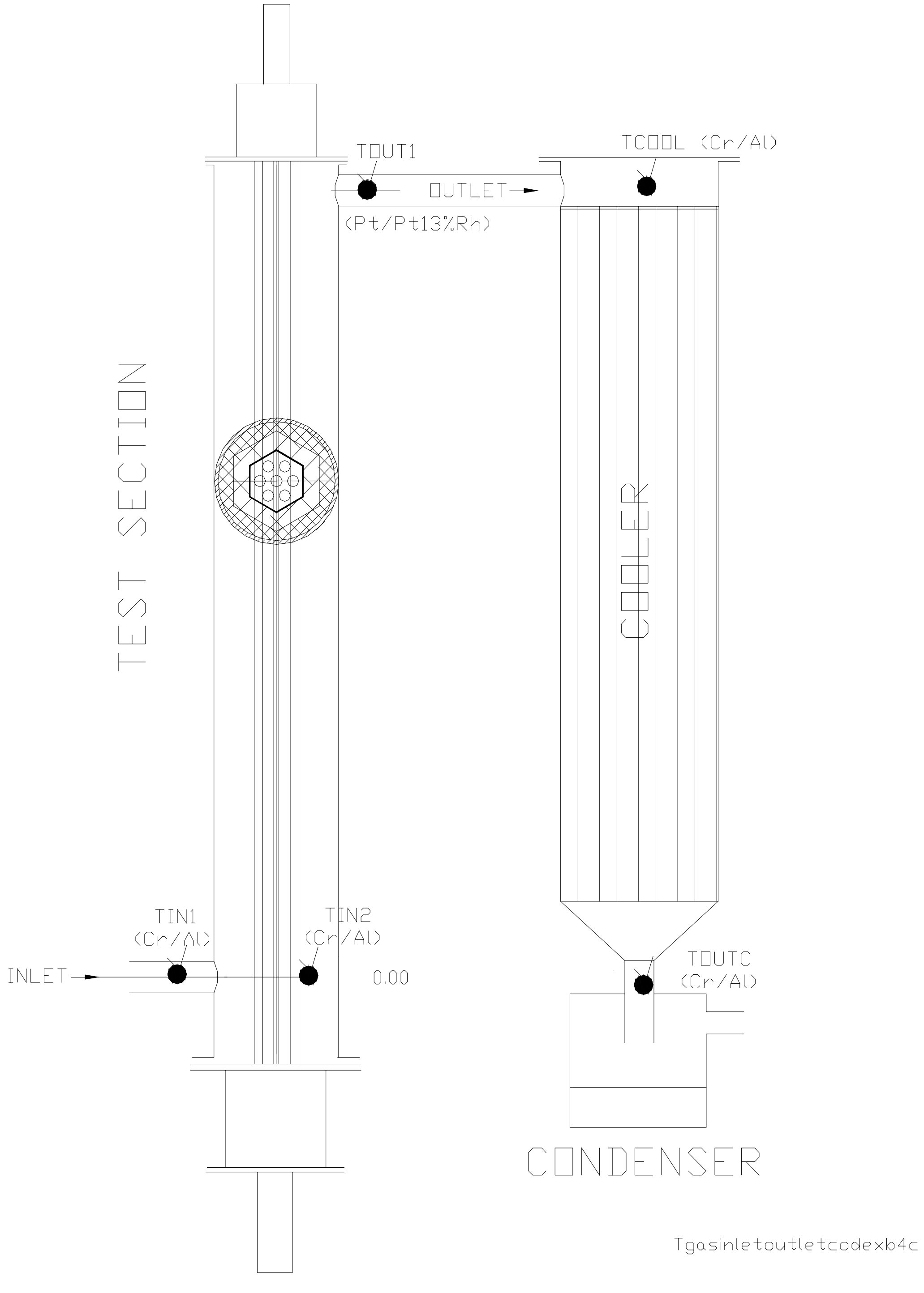

Fig. 13 Placement of coolant temperature measurements

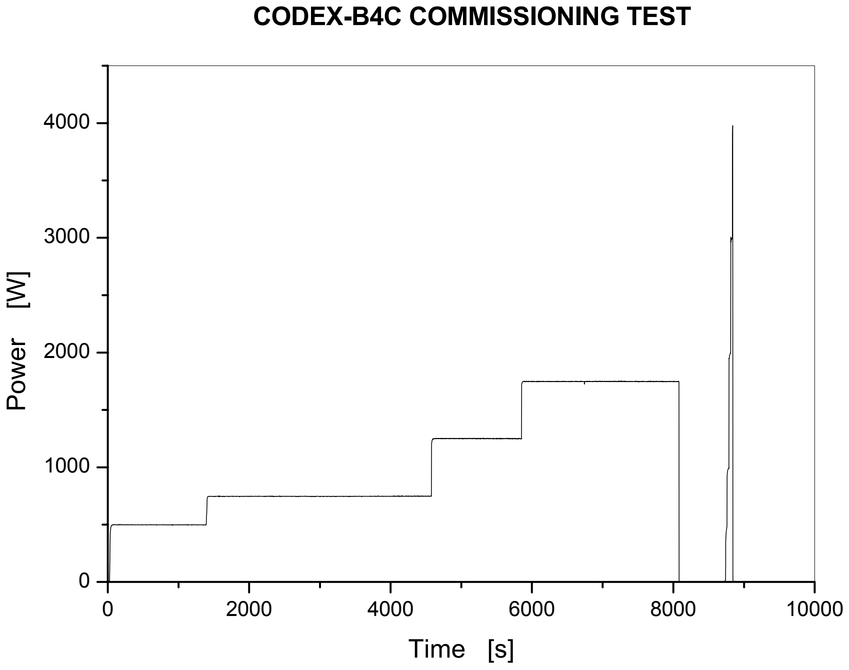

Fig. 14 Electrical power in the CODEX-B4C commissioning test

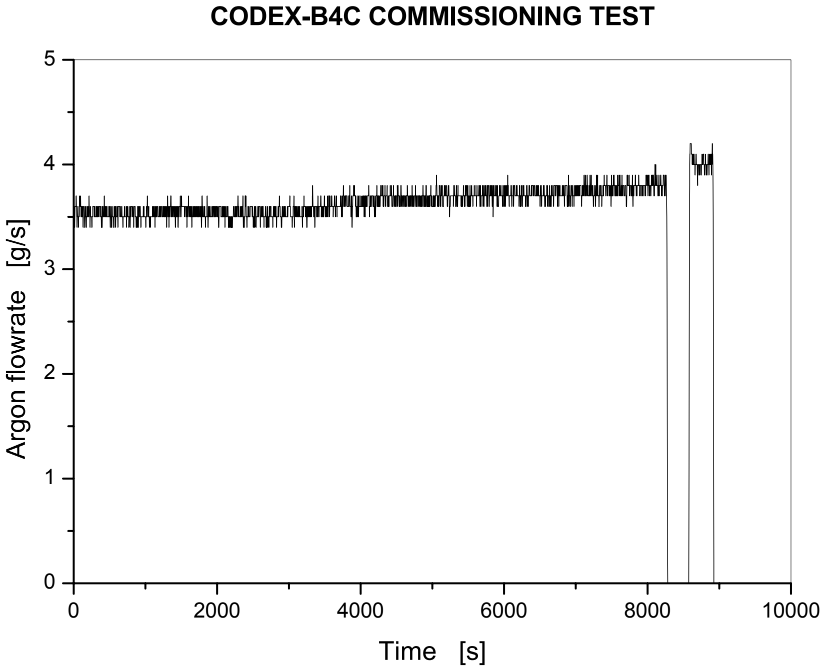

Fig. 15 Argon flowrate in the CODEX-B4C commissioning test

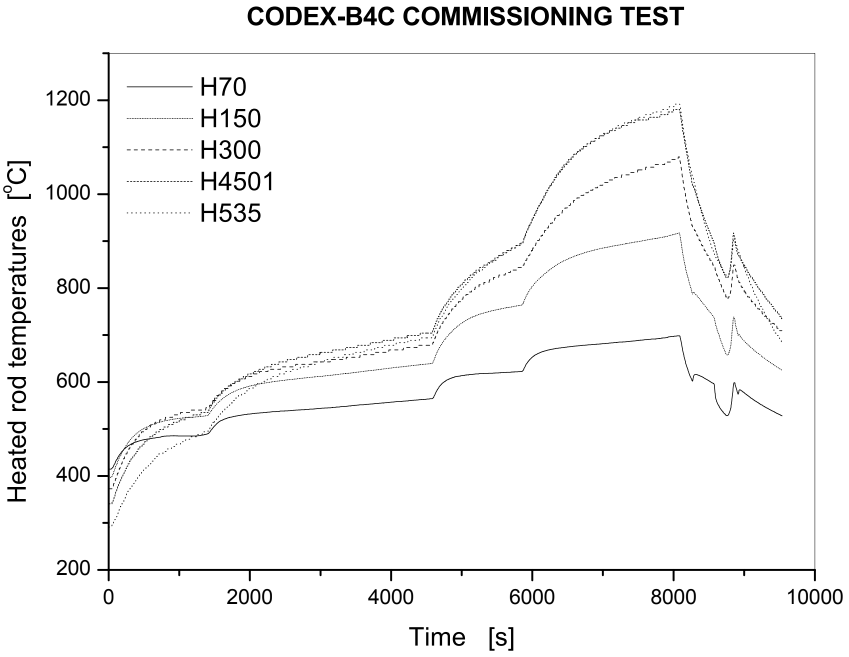

Fig. 16 Heated rod temperatures in the CODEX-B4C commissioning test

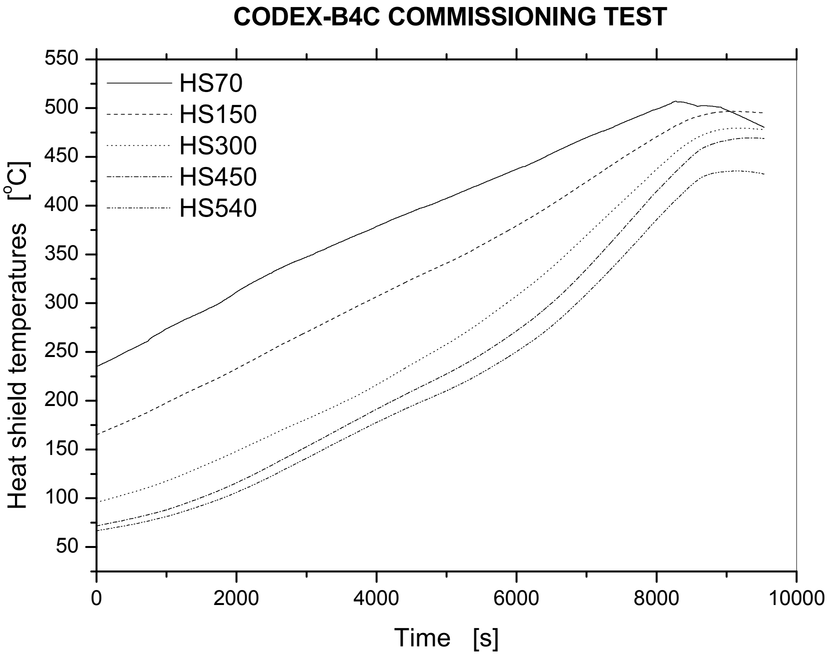

Fig. 17 Steel temperatures in the heat shield in the CODEX-B4C commissioning test

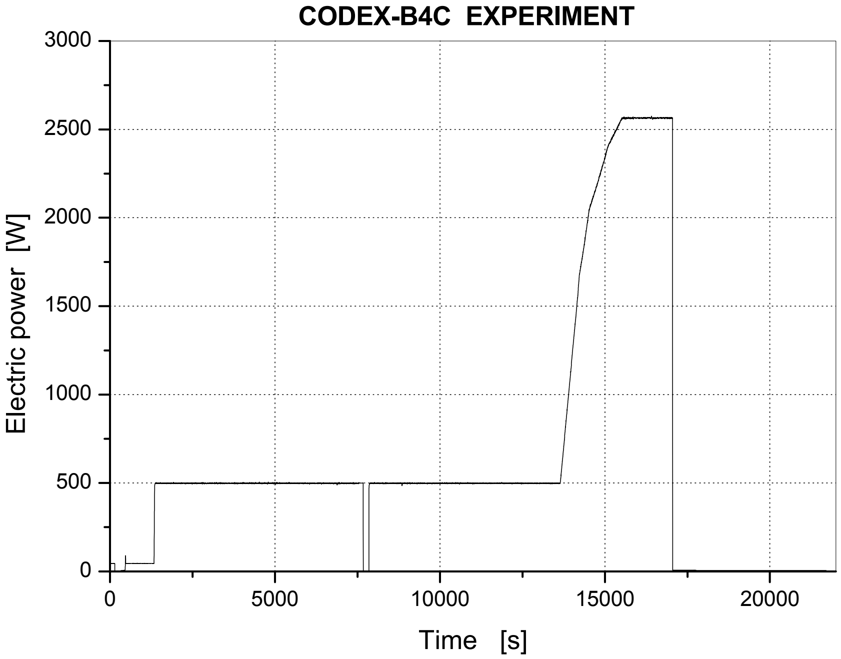

Fig. 18 Electric power during the total recorded period

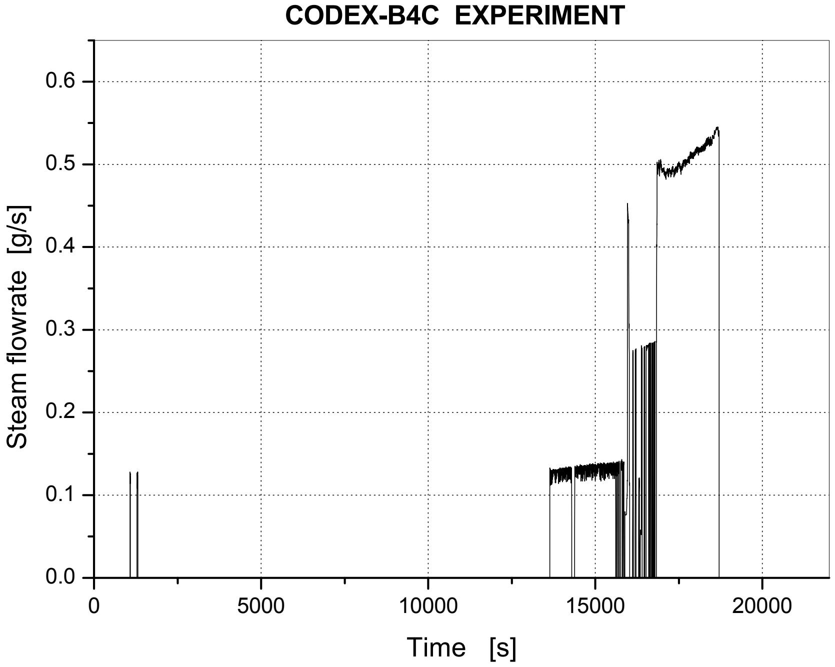

Fig. 19 Steam flowrate during the total recorded period

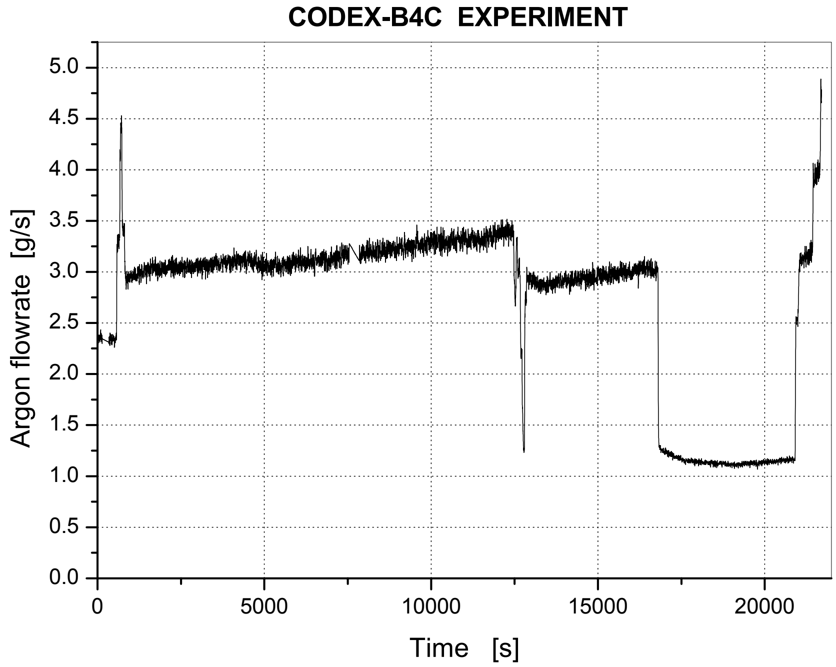

Fig. 20 Argon flowrate during the total recorded period

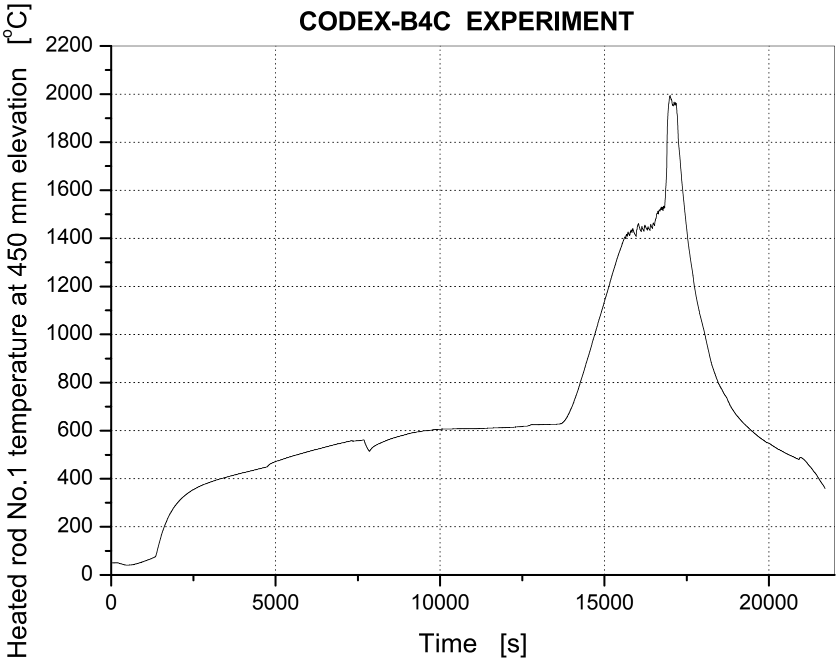

Fig. 21 Heated rod temperature during the total recorded period

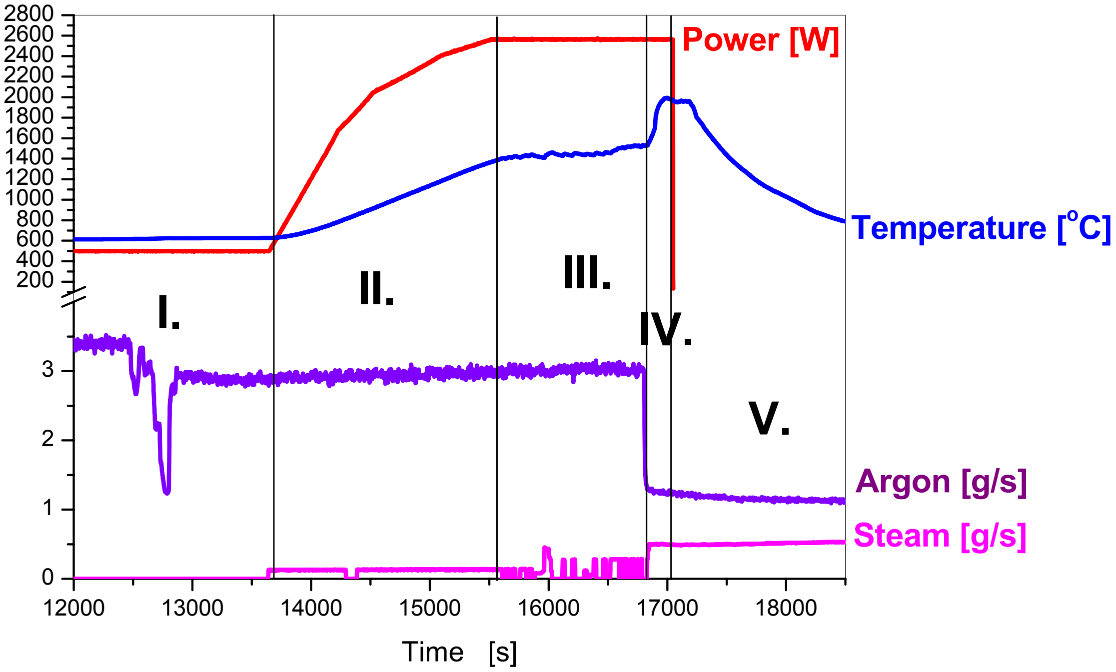

Fig. 22 Main phases of the CODEX-B4C test

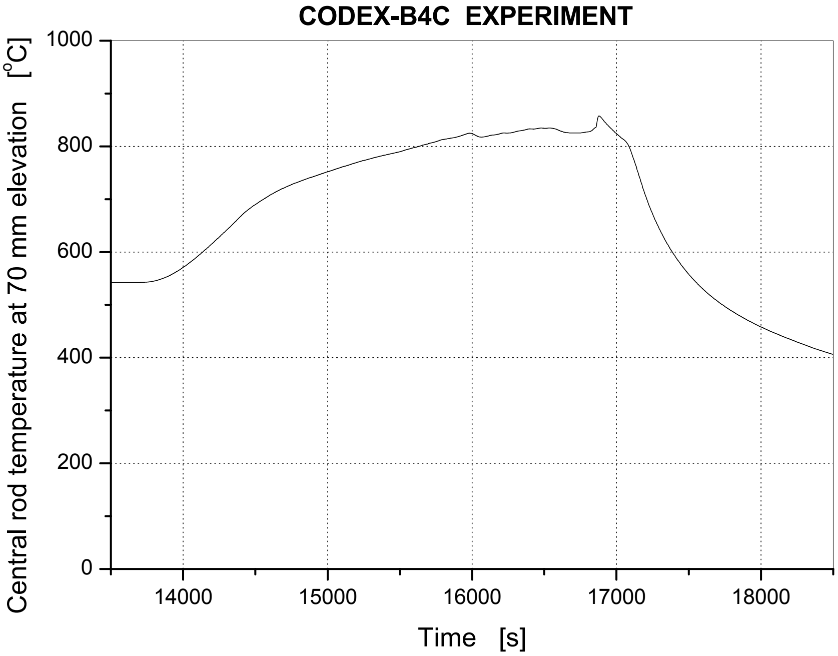

Fig. 23 C70: Central rod temperature at 70 mm

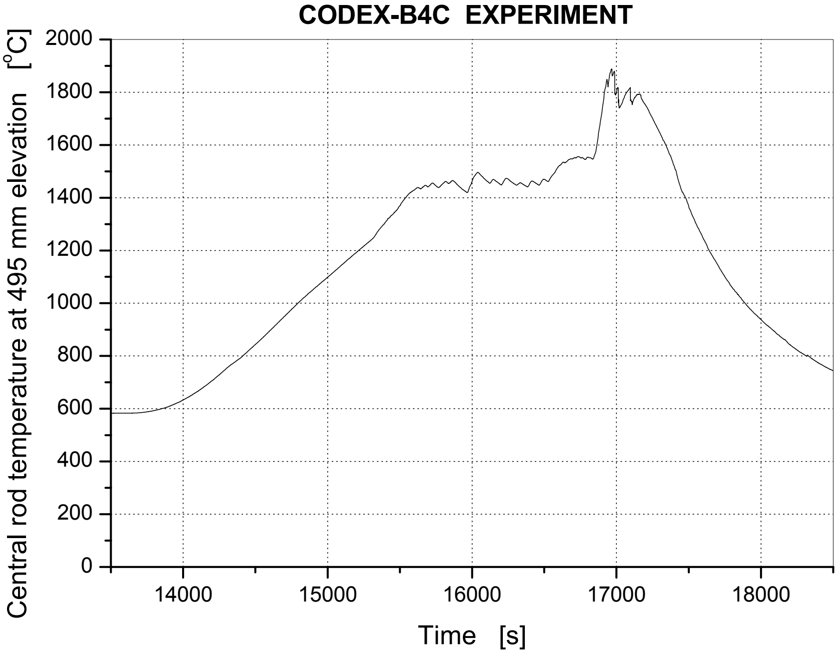

Fig. 24 C495: Central rod temperature at 495 mm

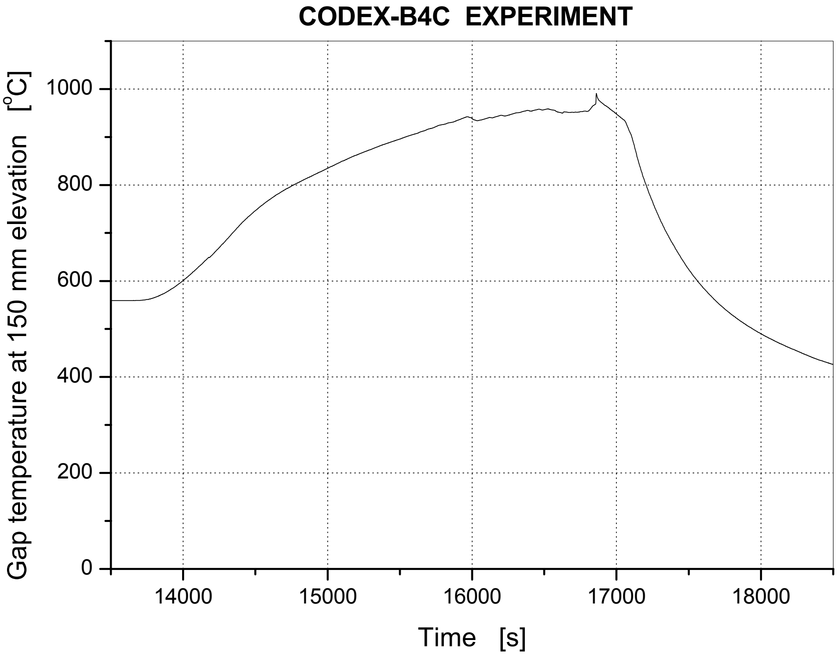

Fig. 25 GP150: Guide tube - central rod gap temperature at 150 mm

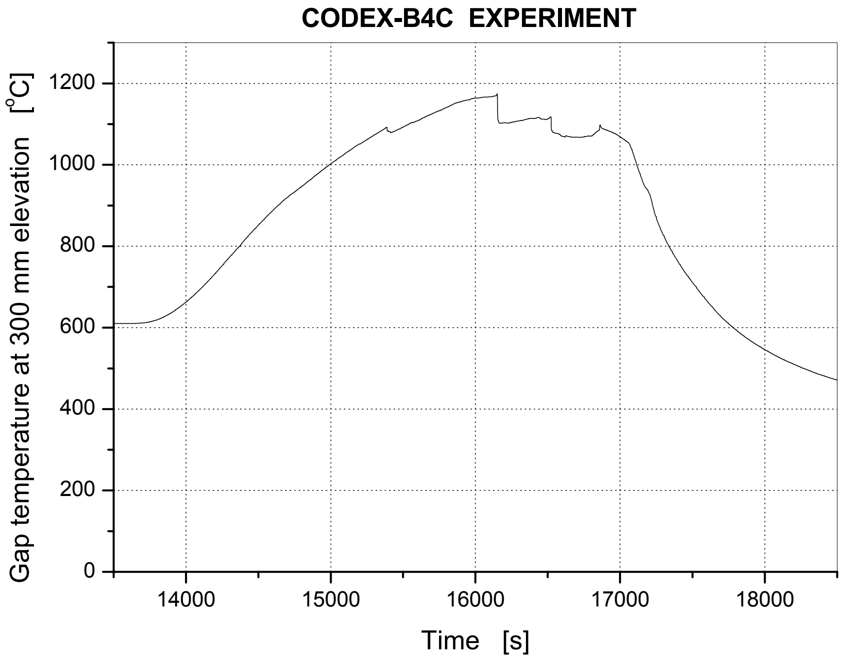

Fig. 26 GP300: Guide tube - central rod gap temperature at 300 mm

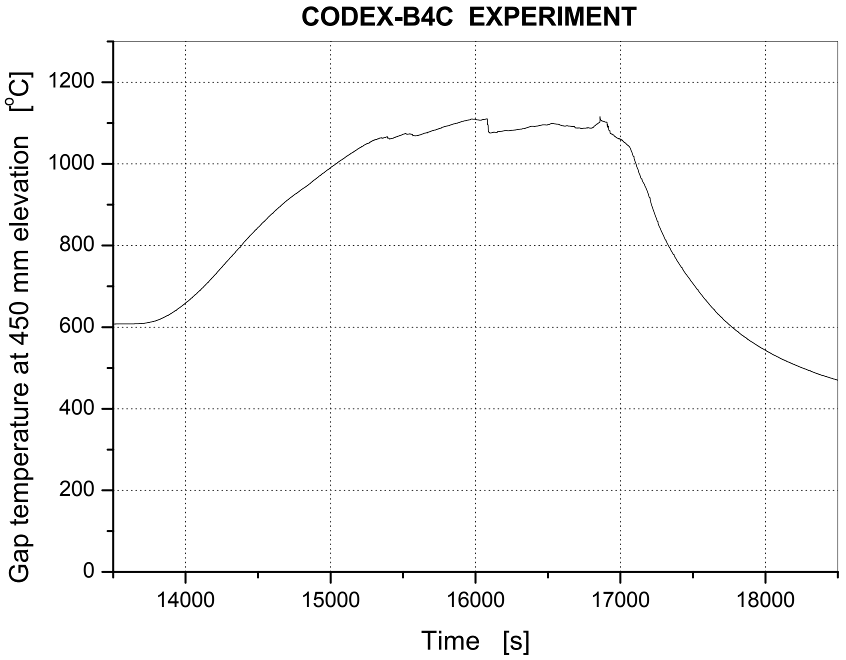

Fig. 27 GP450: Guide tube - central rod gap temperature at 450 mm

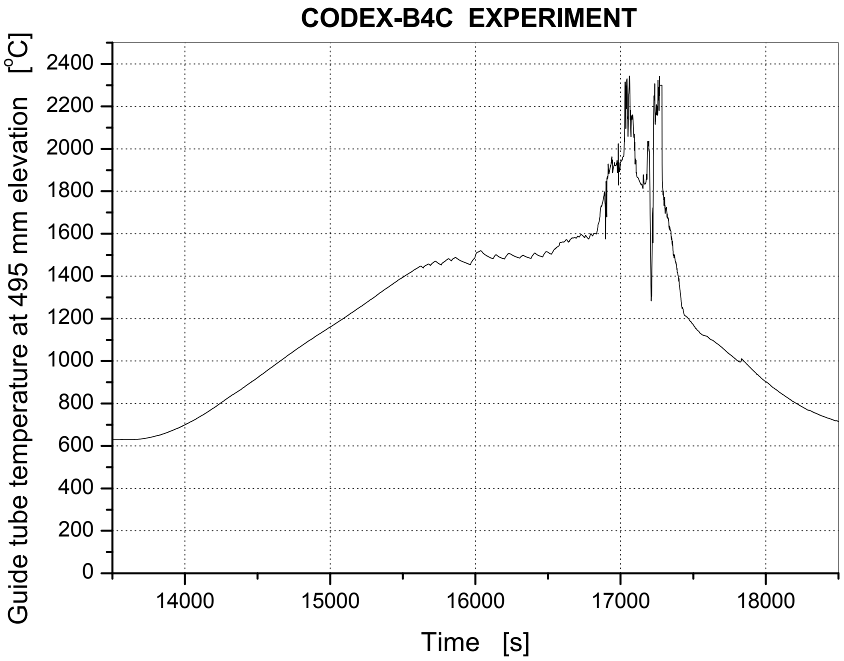

Fig. 28 GD495: Guide tube temperature at 495 mm

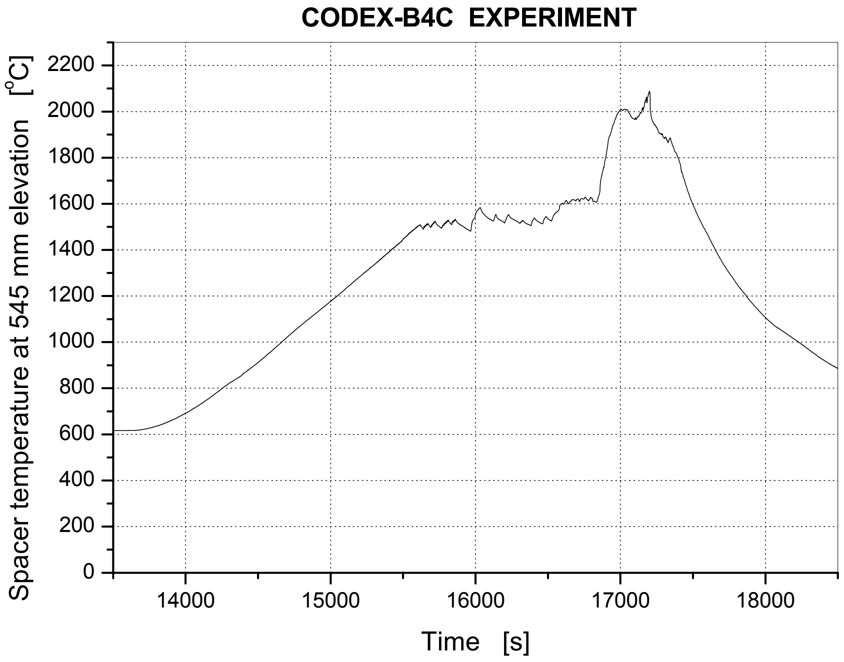

Fig. 29 SP545: Spacer temperature at 545 mm

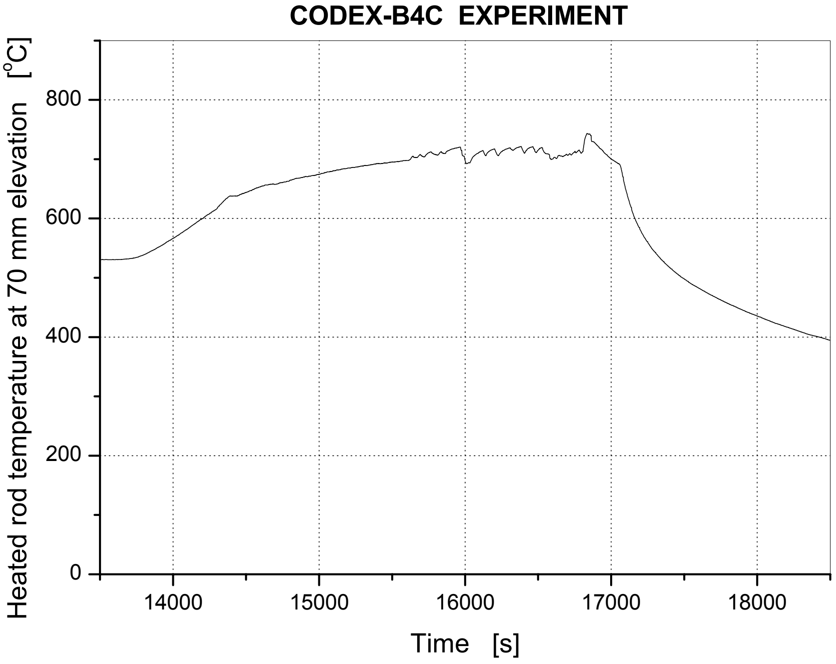

Fig. 30 H70: Heated rod temperature at 70 mm

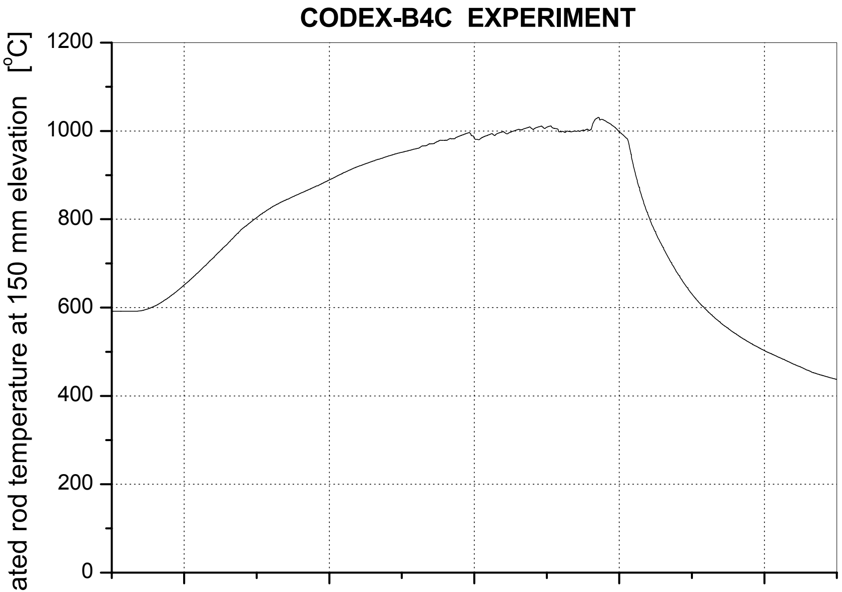

Fig. 31 H150: Heated rod temperature at 150 mm

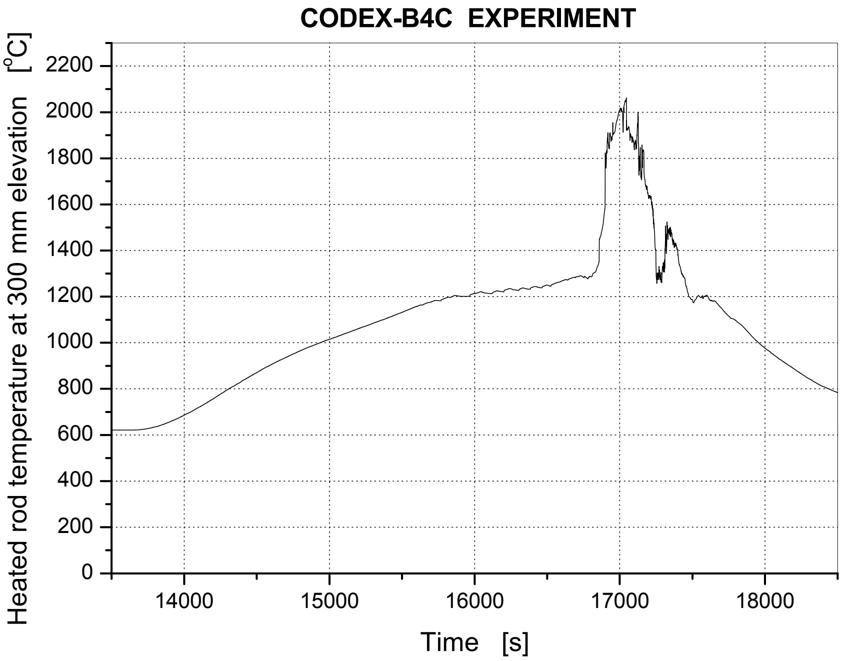

Fig. 32 H300: Heated rod temperature at 300 mm

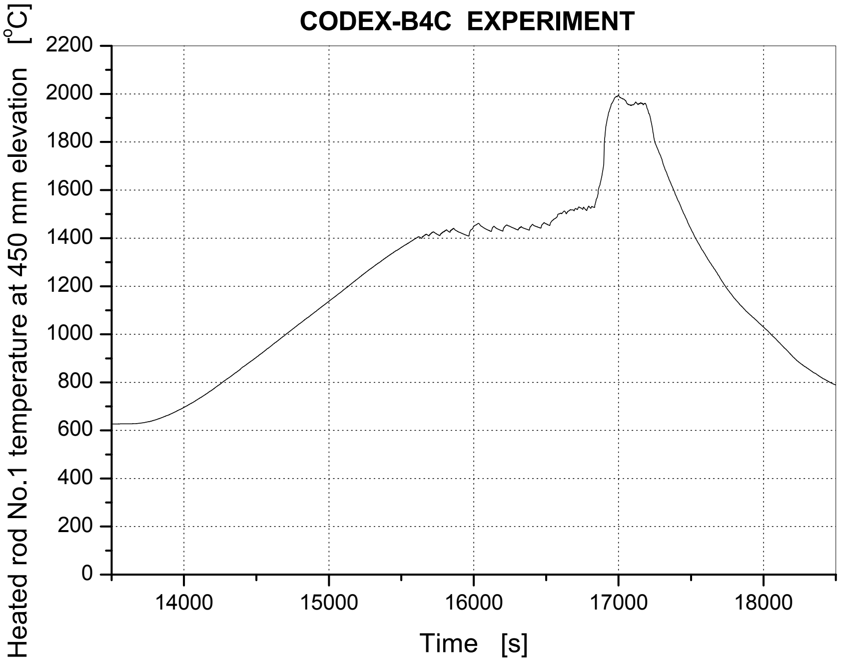

Fig. 33 H4501: Heated rod temperature at 450 mm, No. 1.

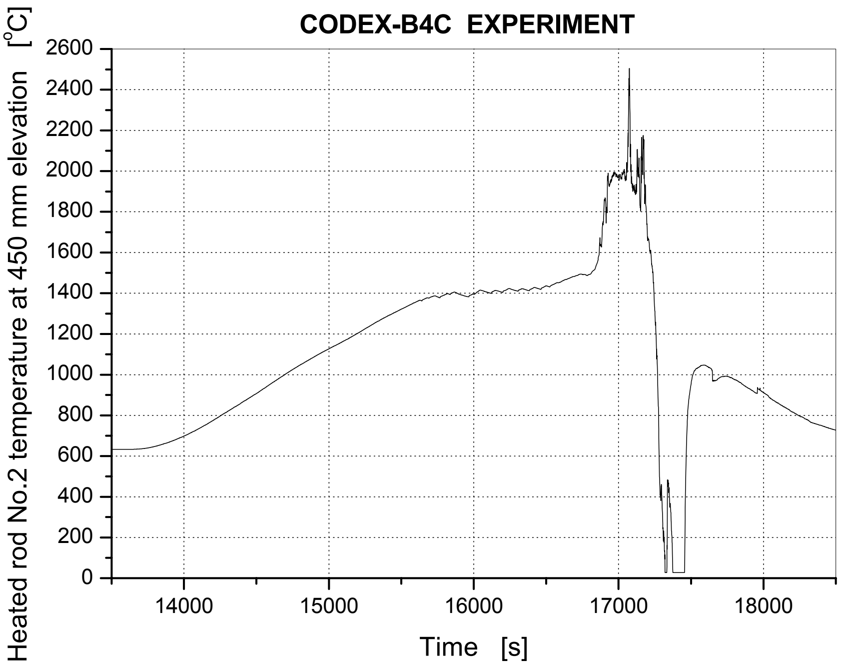

Fig. 34 H4502: Heated rod temperature at 450 mm, No. 2.

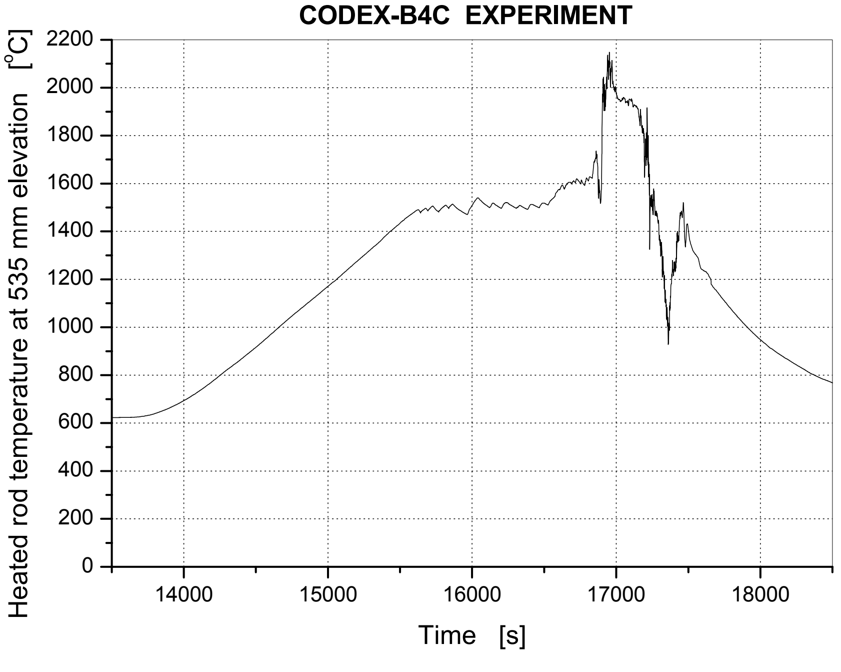

Fig. 35 H535: Heated rod temperature at 535 mm

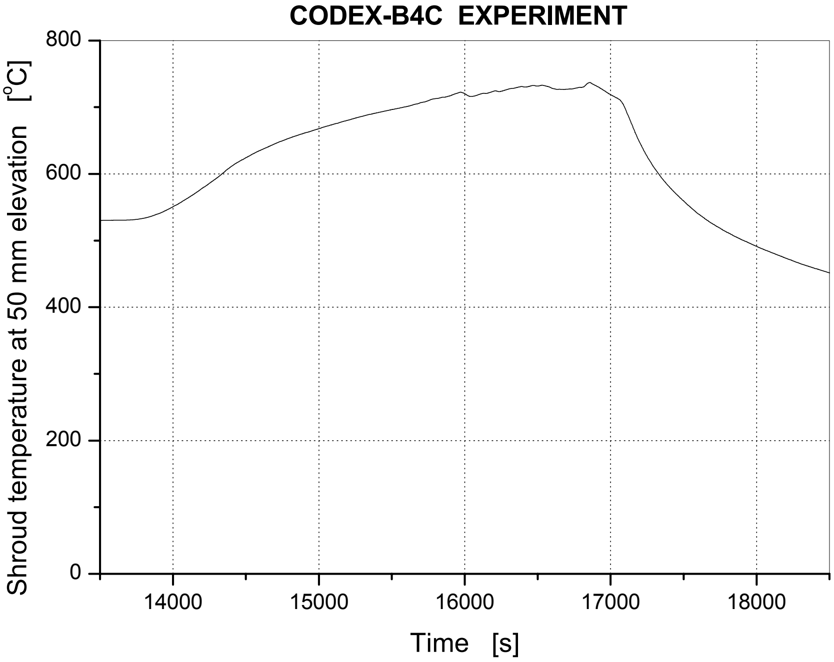

Fig. 36 SH50: Shroud temperature at 50 mm

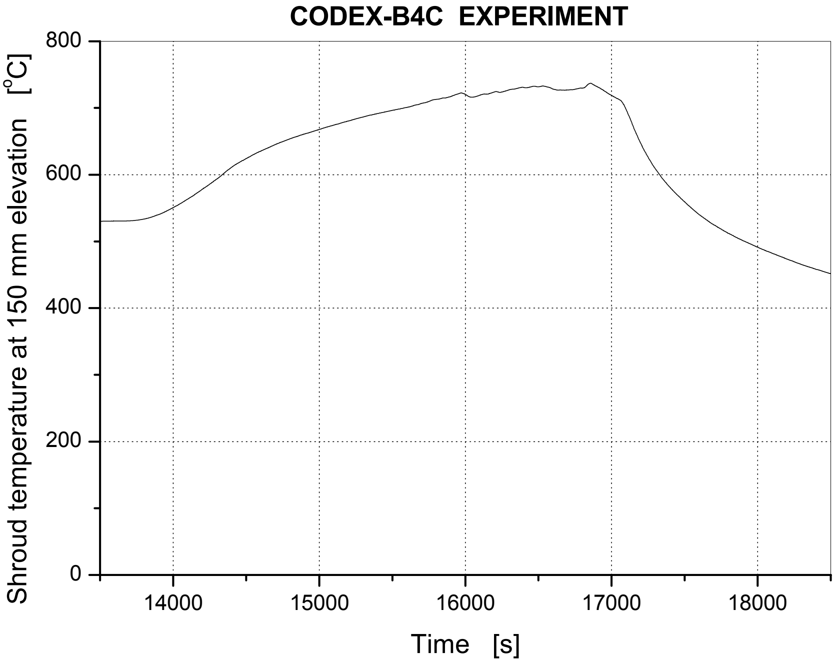

Fig. 37 SH150: Shroud temperature at 150 mm

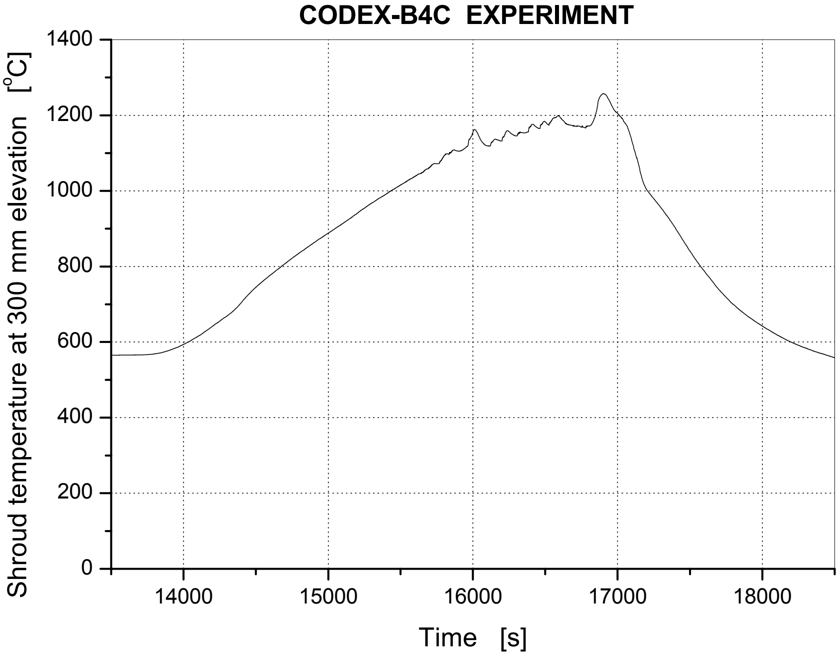

Fig. 38 SH300: Shroud temperature at 300 mm

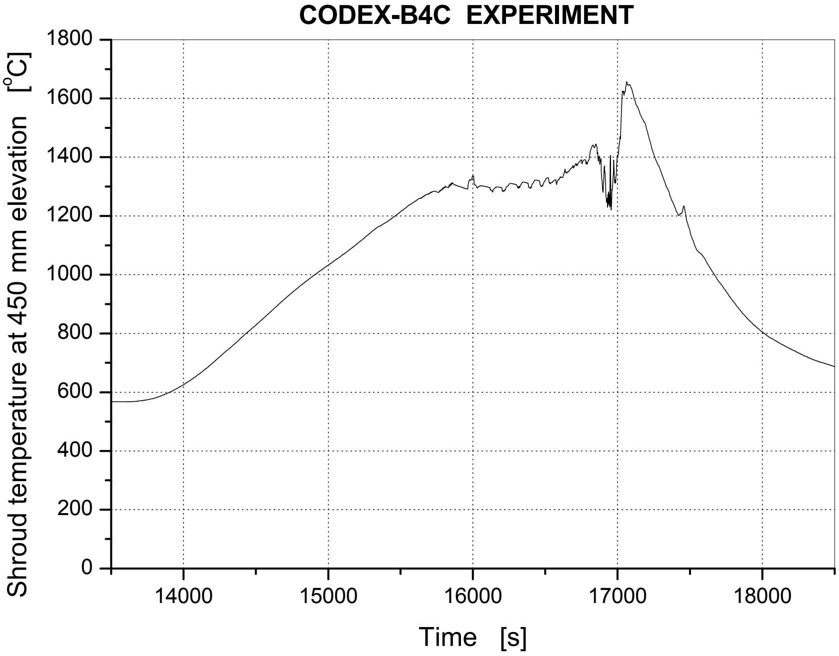

Fig. 39 SH450: Shroud temperature at 450 mm

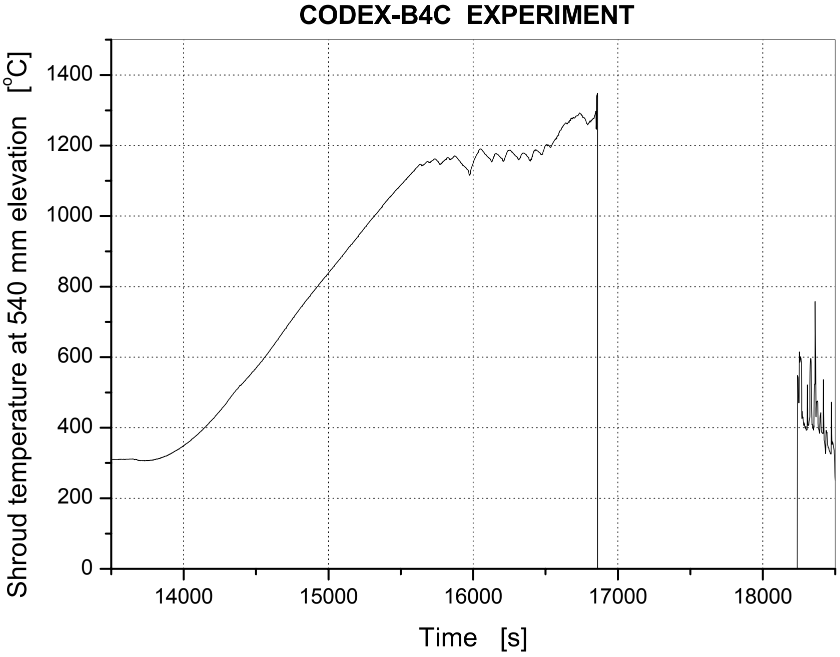

Fig. 40 SH540: Shroud temperature at 540 mm

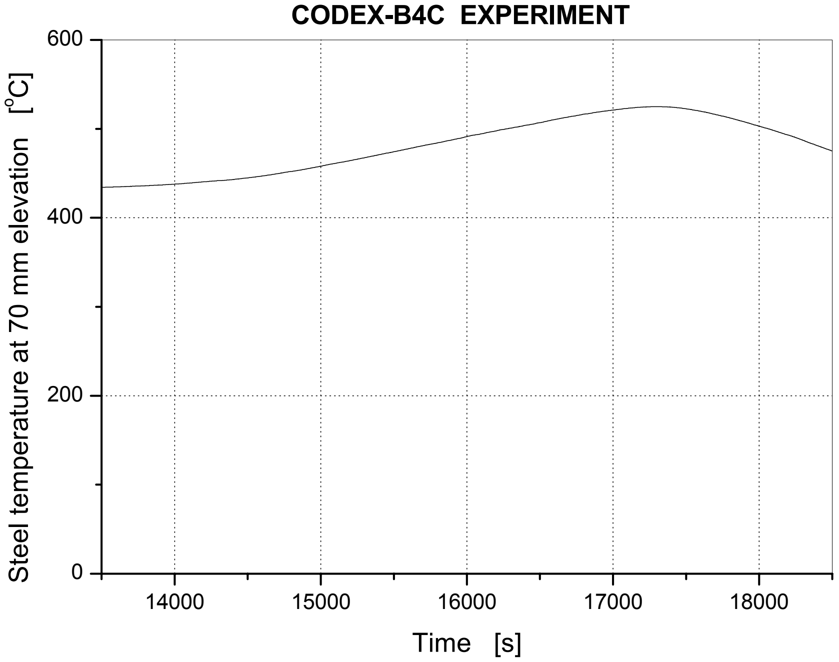

Fig. 41 HS70: Steel heat shield temperature at 70 mm

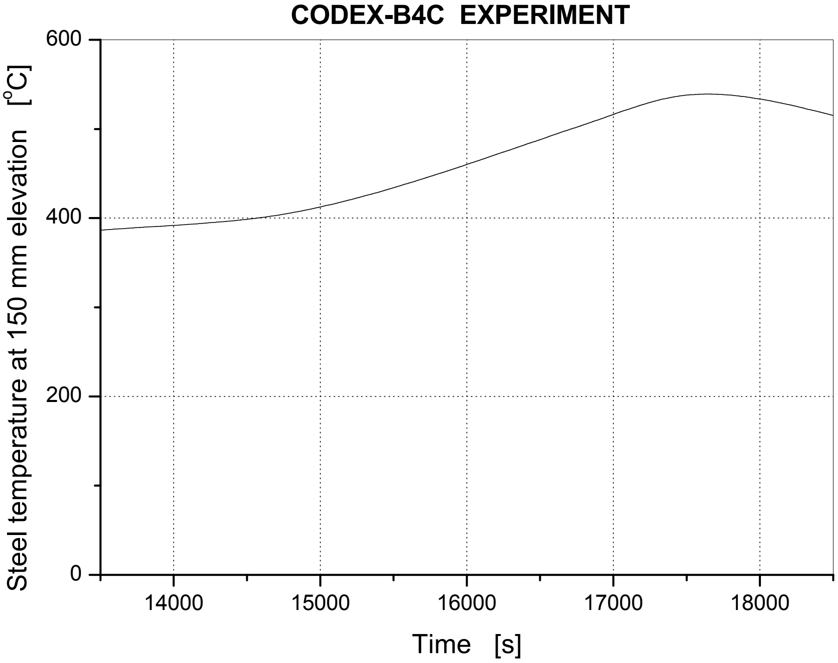

Fig. 42 HS150: Steel heat shield temperature at 150 mm

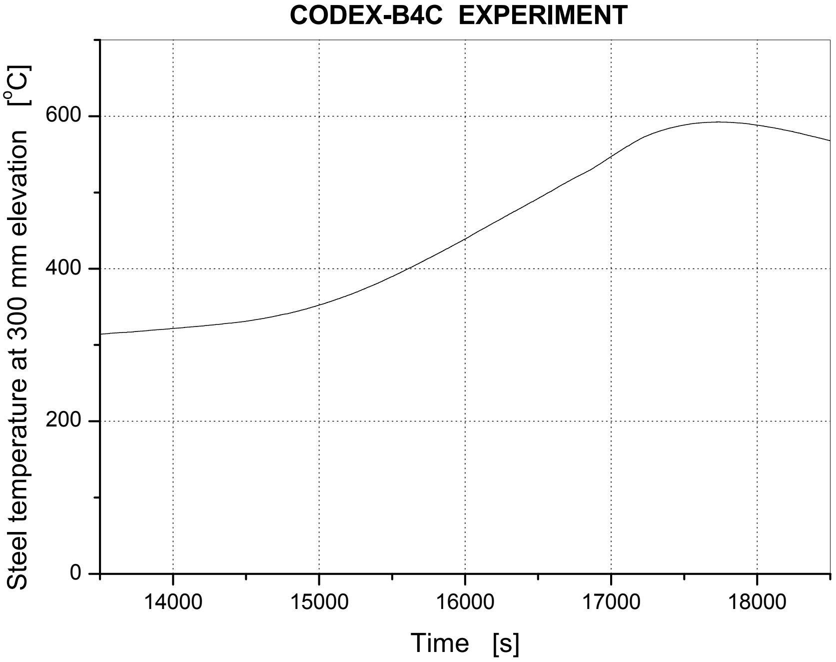

Fig. 43 HS300: Steel heat shield temperature at 300 mm

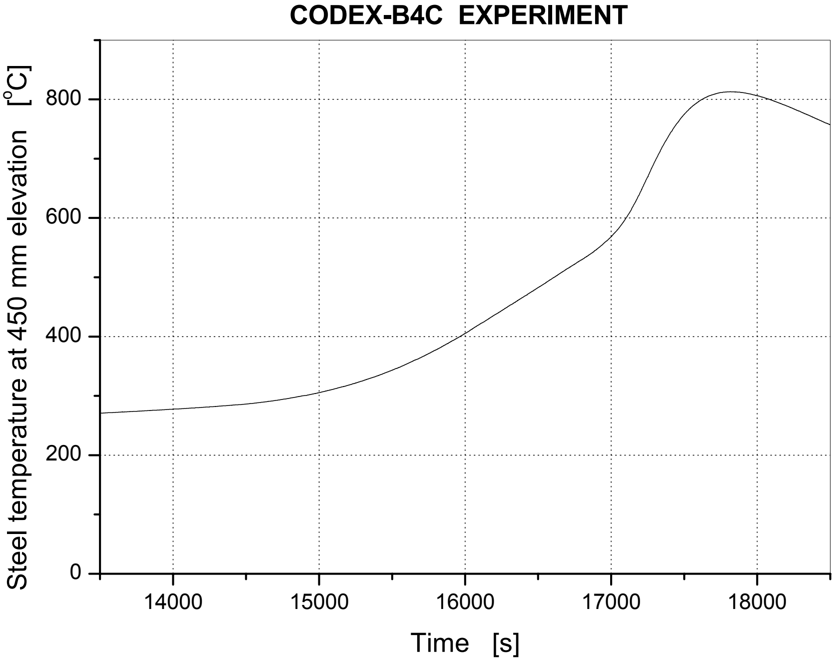

Fig. 44 HS450: Steel heat shield temperature at 450 mm

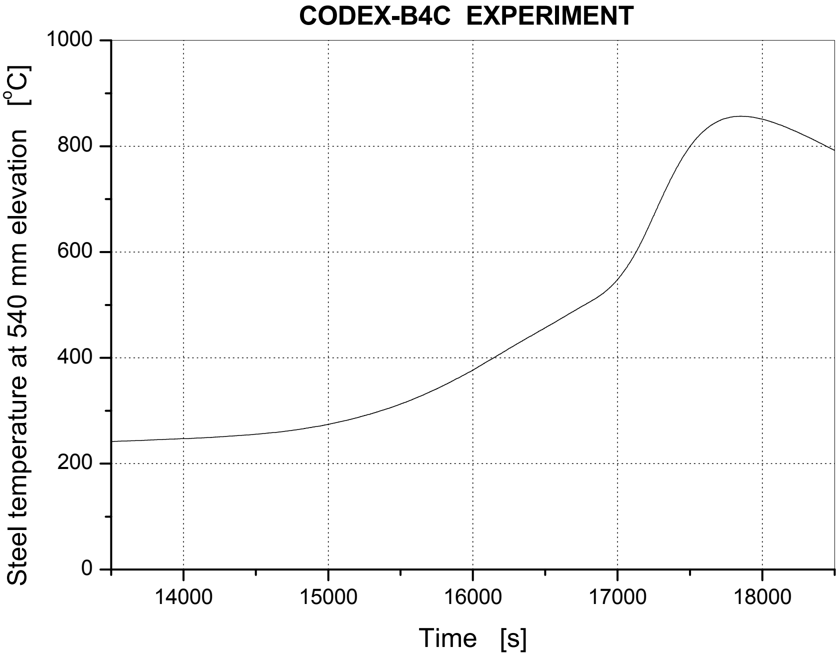

Fig. 45 HS540: Steel heat shield temperature at 540 mm

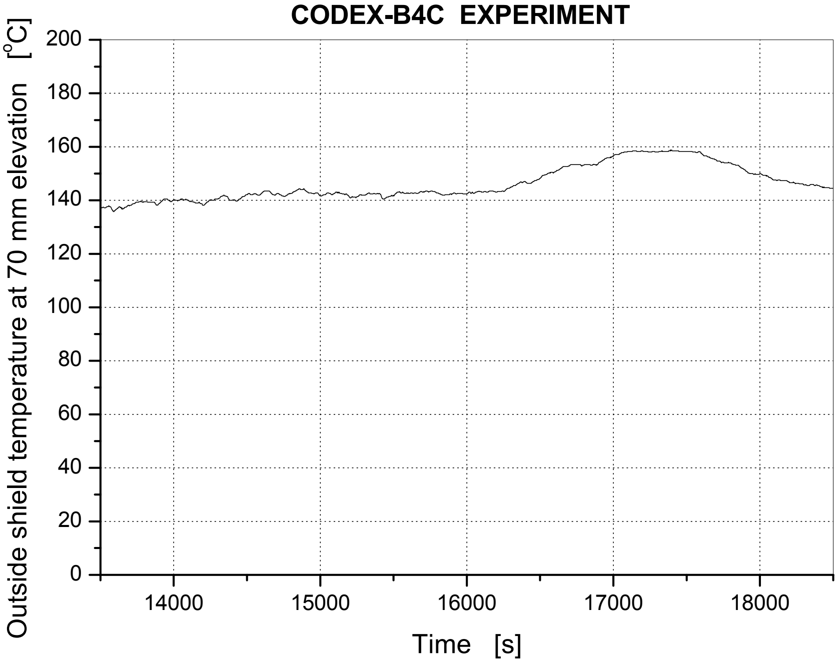

Fig. 46 OS70: Outside shield temperature at 70 mm

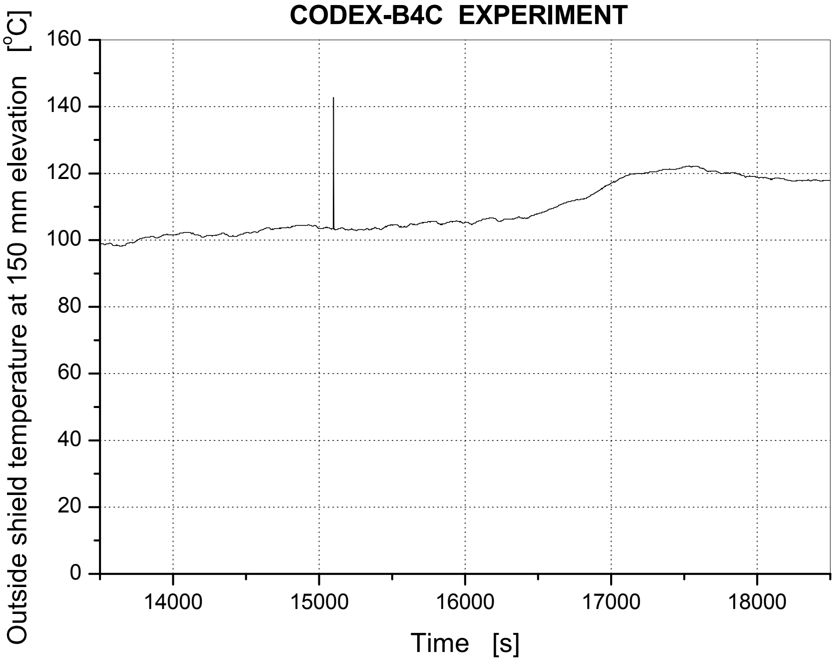

Fig. 47 OS150: Outside shield temperature at 150 mm

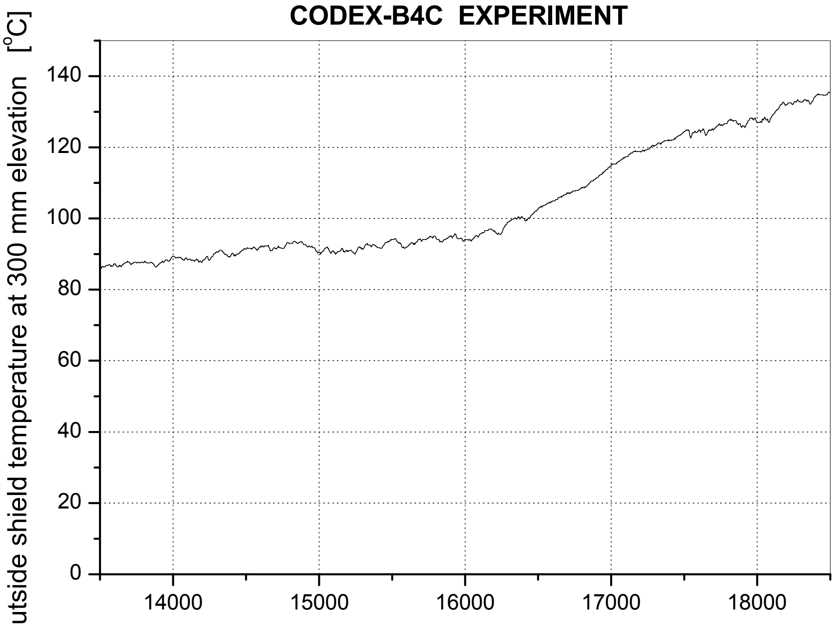

Fig. 48 OS300: Outside shield temperature at 300 mm

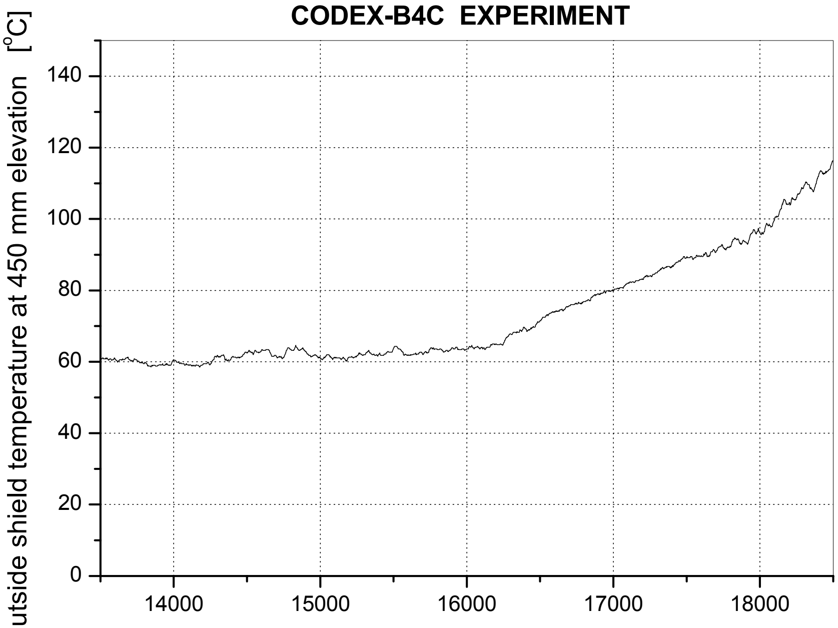

Fig. 49 OS450: Outside shield temperature at 450 mm

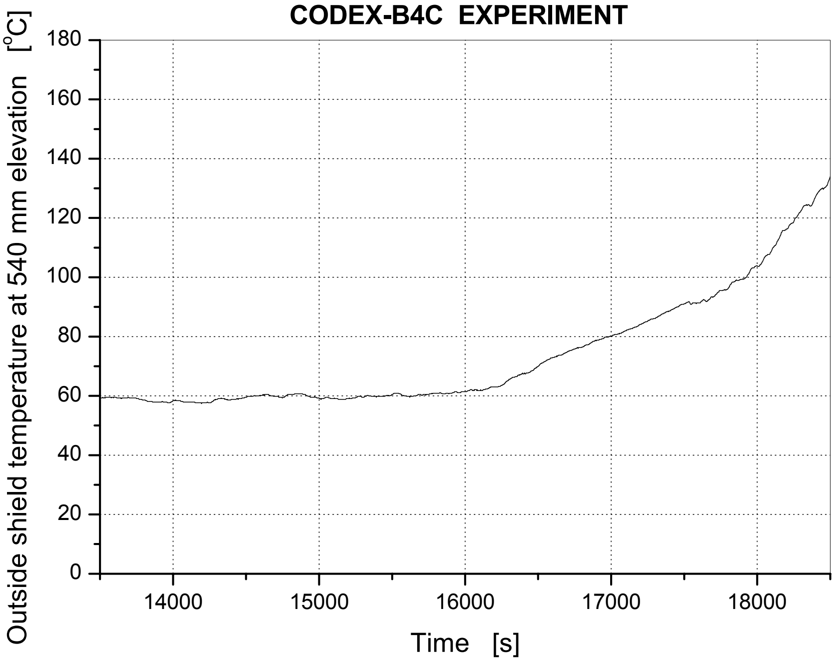

Fig. 50 OS540: Outside shield temperature at 540 mm

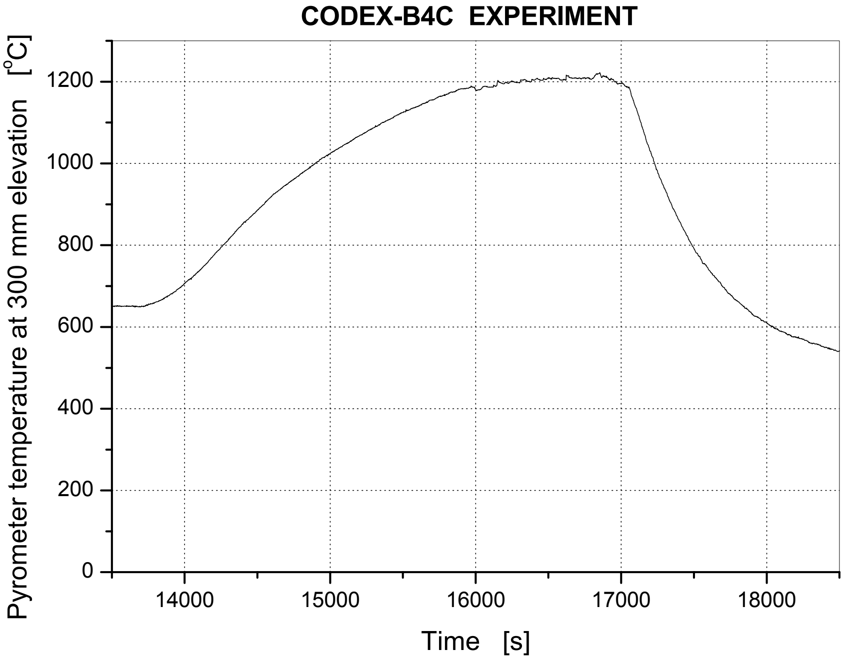

Fig. 51 PYR300: Pyrometer temperature at 300 mm

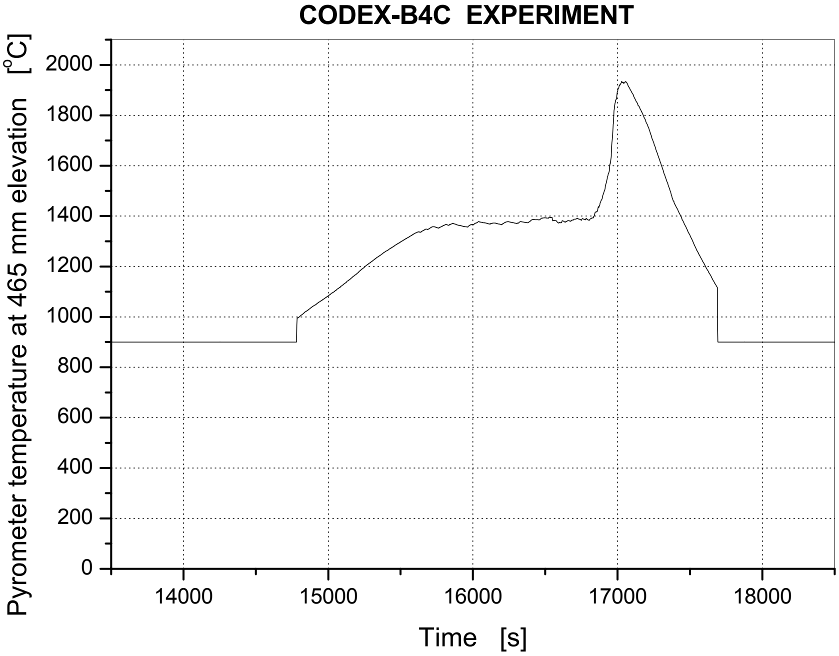

Fig. 52 PYR465: Pyrometer temperature at 465 mm

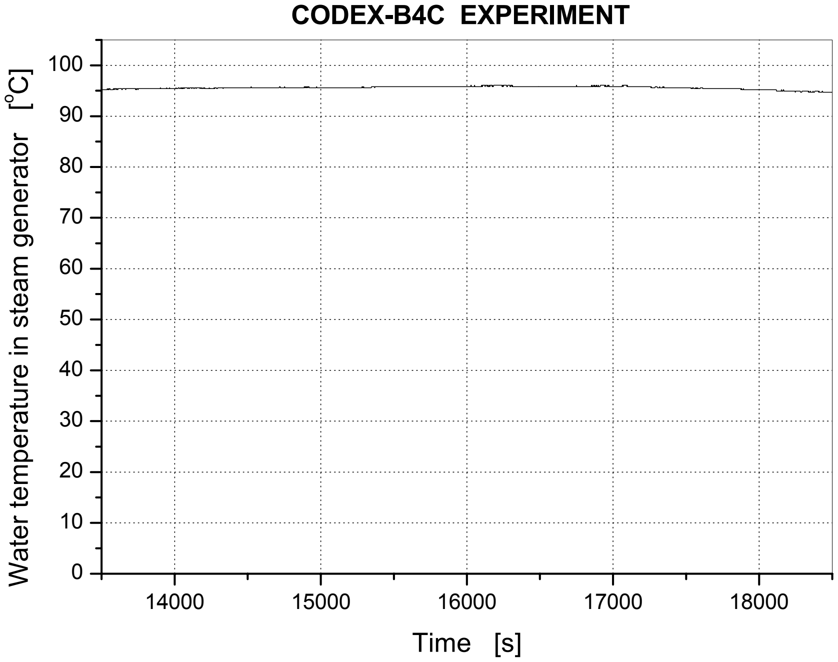

Fig. 53 TWATER: Water temperature in steam generator

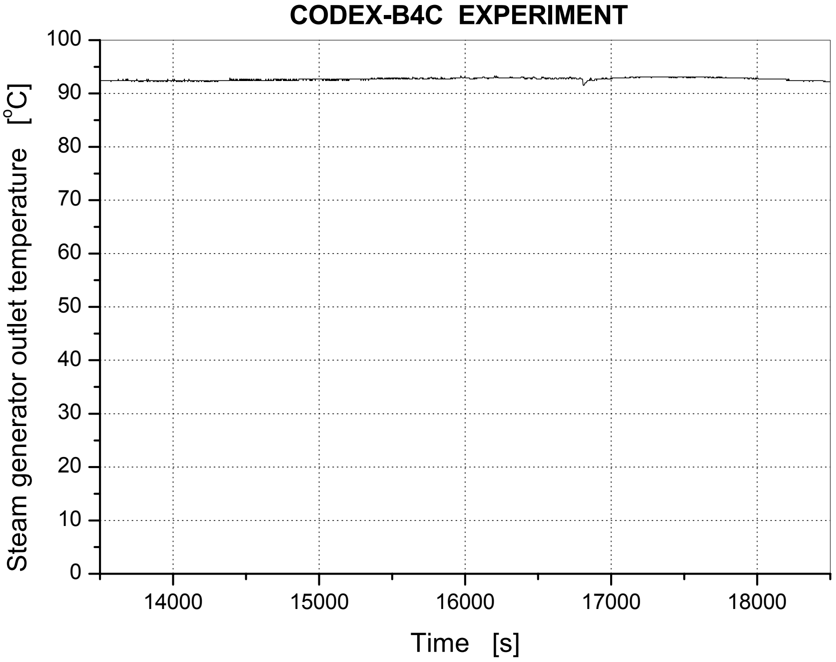

Fig. 54 TSTEAM: Steam generator outlet temperature

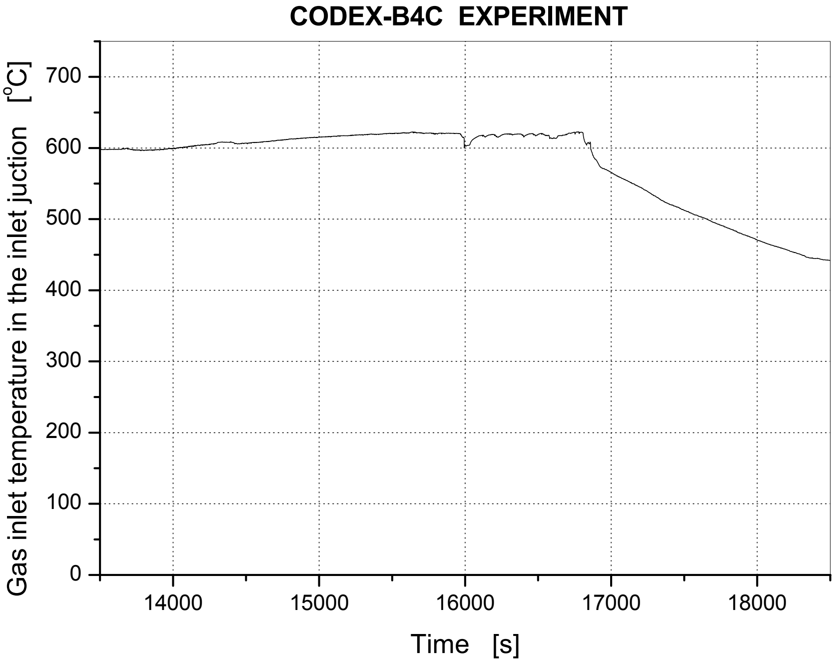

Fig. 55 TIN1: Gas inlet temperature in the inlet junction

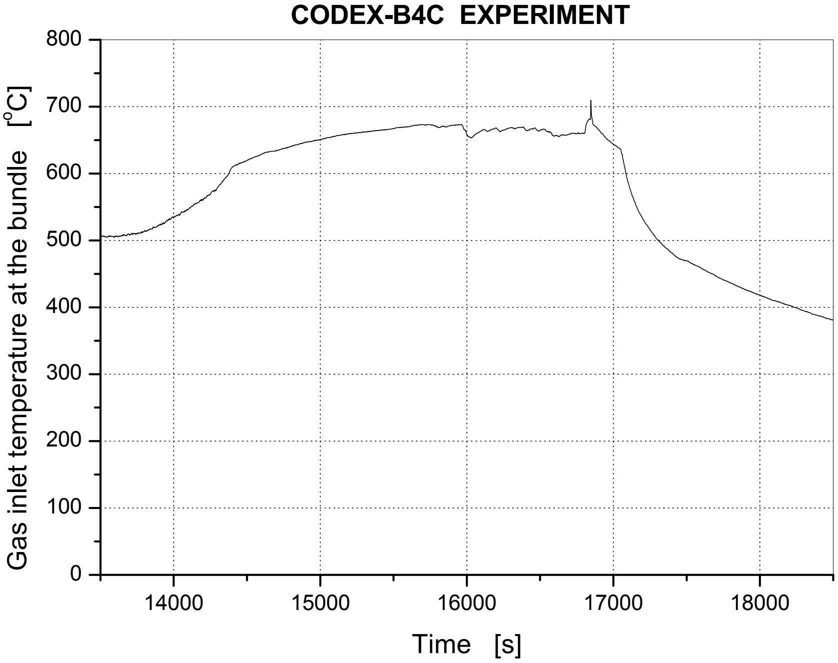

Fig. 56 TIN2: Gas inlet temperature at the bundle

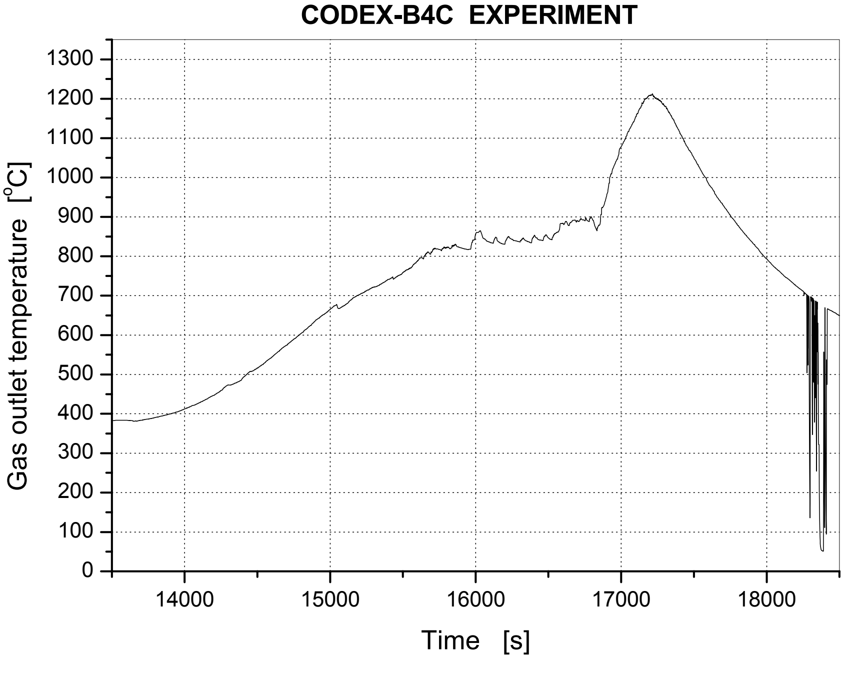

Fig. 57 TOUT1: Gas outlet temperature in the outlet junction

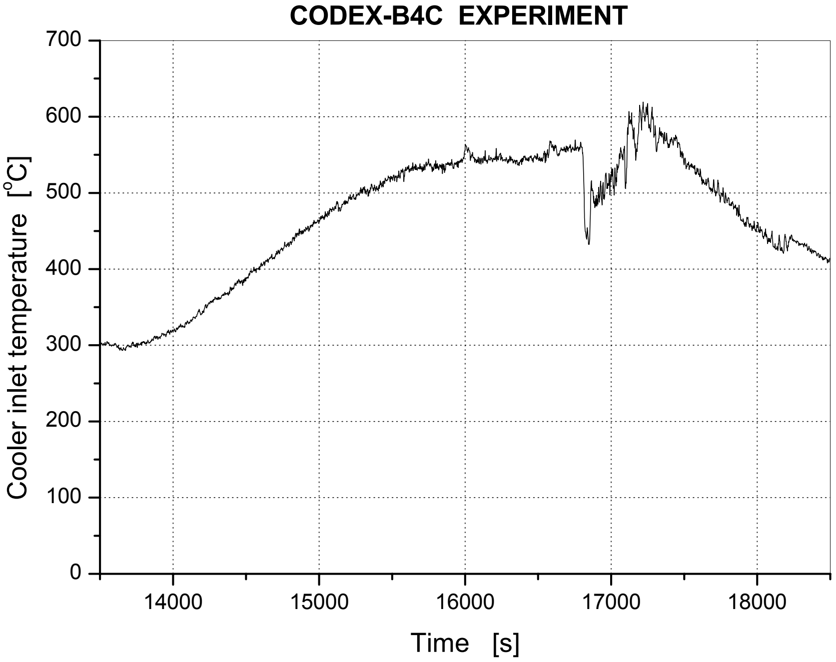

Fig. 58 TCOOL: Gas temperature at the cooler inlet

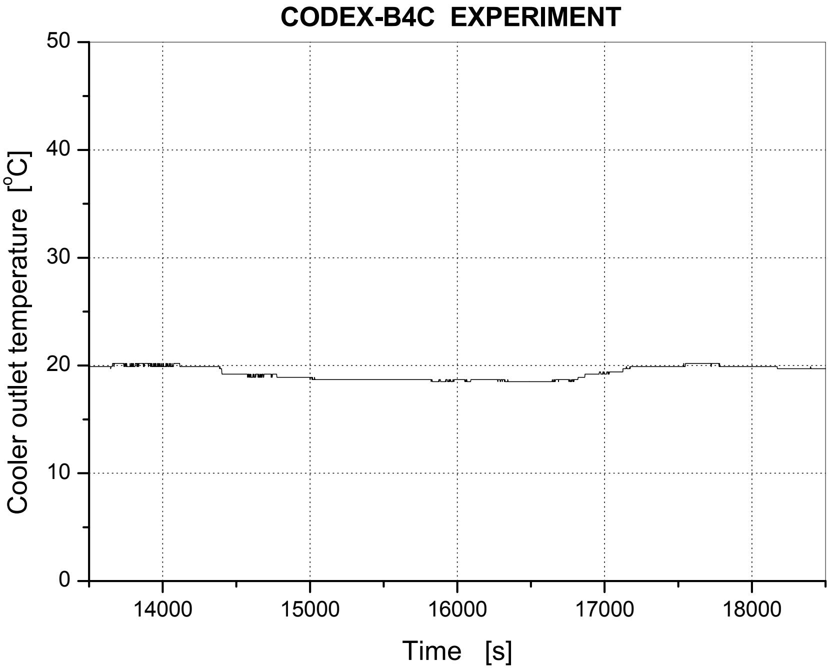

Fig. 59 TOUTC: Gas temperature at the cooler outlet

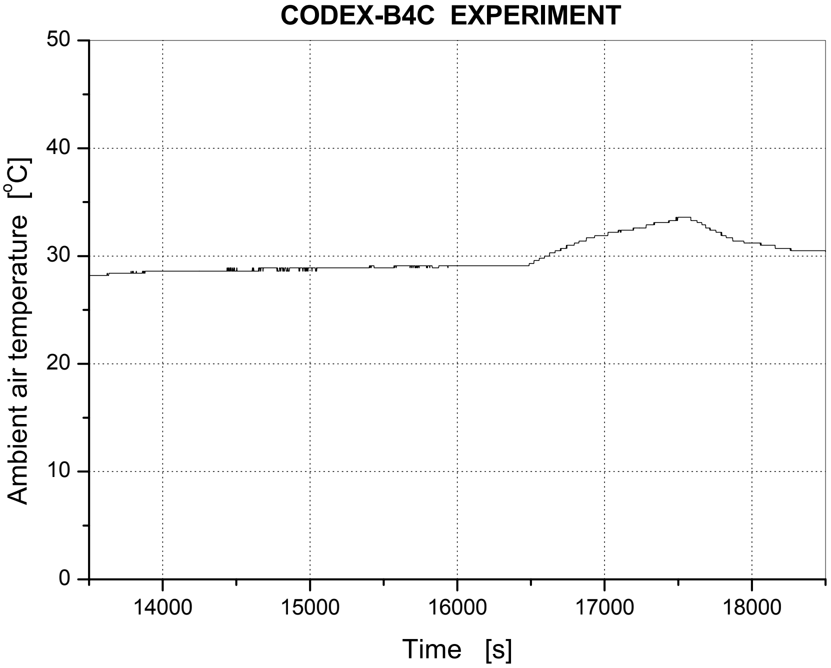

Fig. 60 TAMB: Ambient air temperature

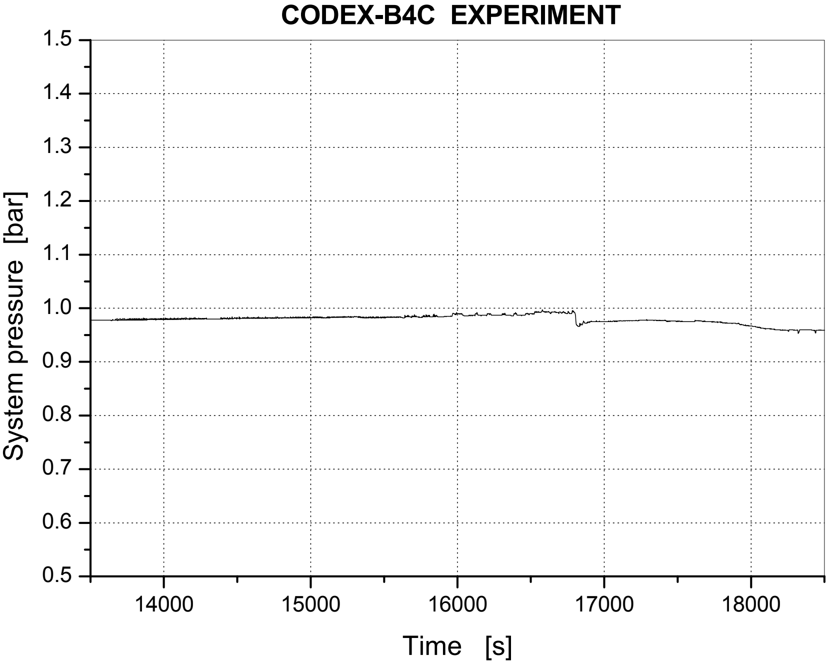

Fig. 61 PSYS: System pressure

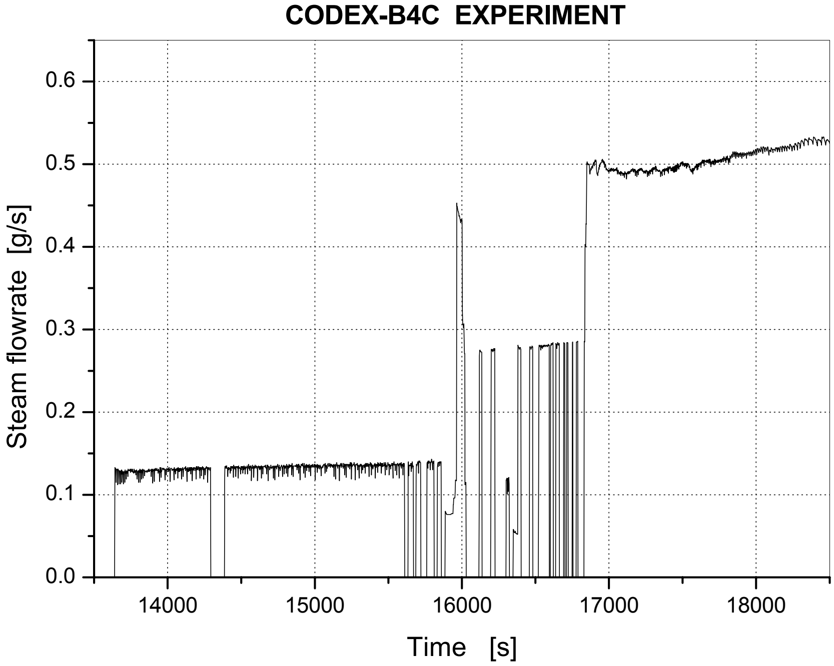

Fig. 62 STEAM: Steam flow

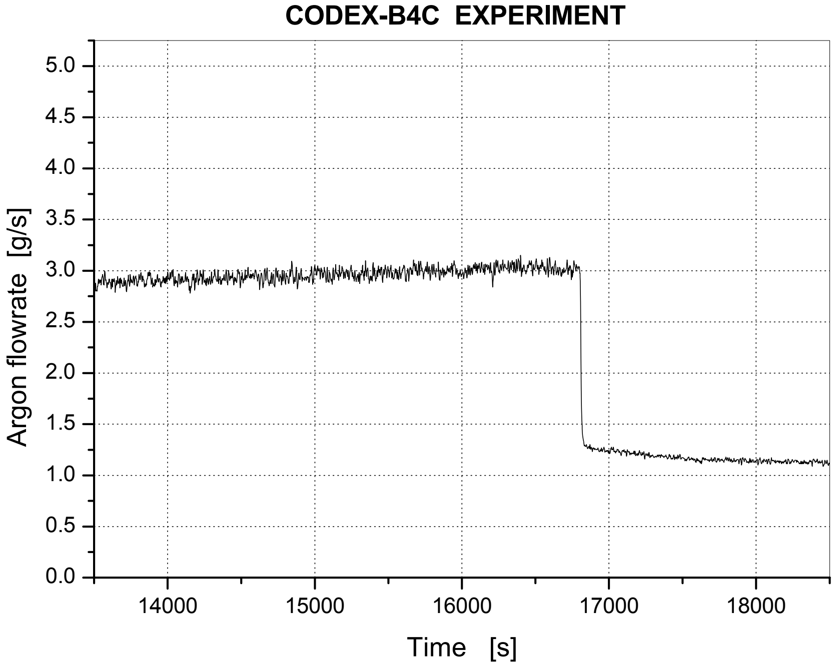

Fig. 63 ARGON: Argon flow

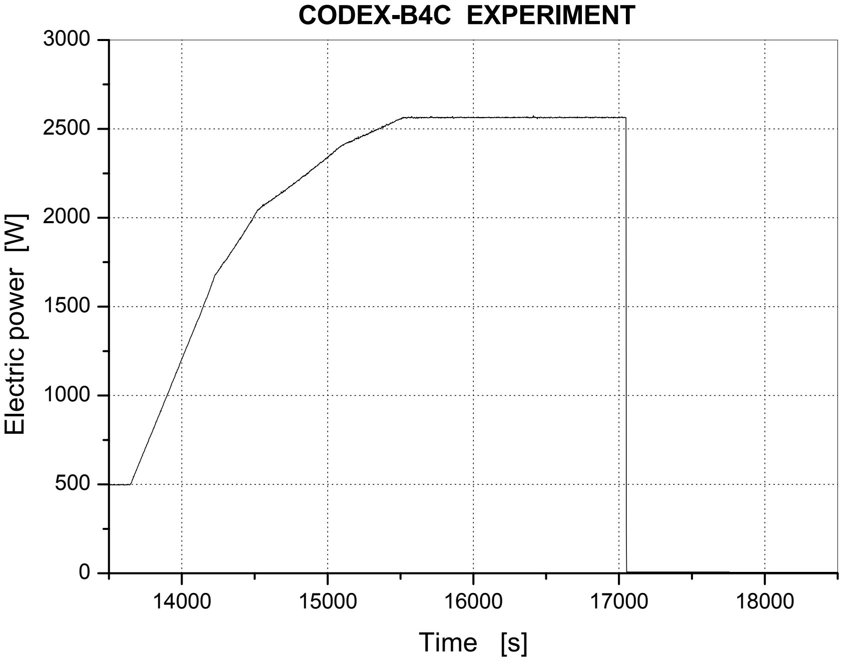

Fig. 64 POWER: Electric power

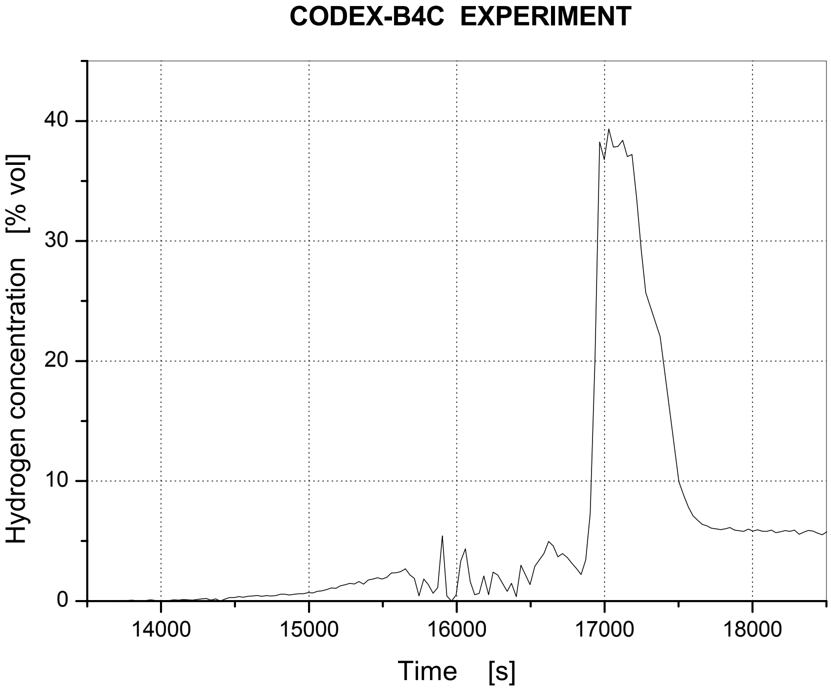

Fig. 65 H2CON: Hydrogen concentration

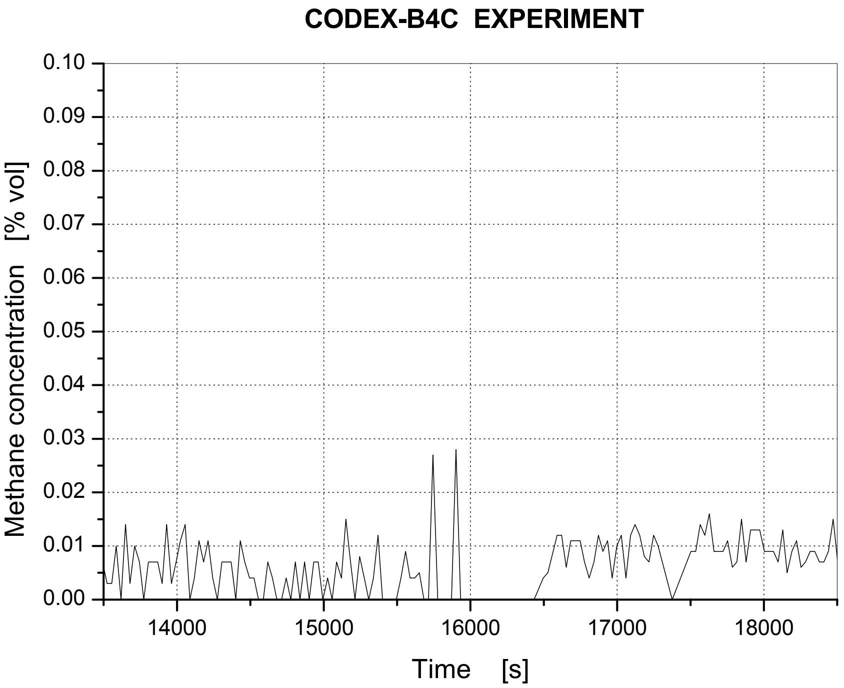

Fig. 66 CH4CON: Methane concentration

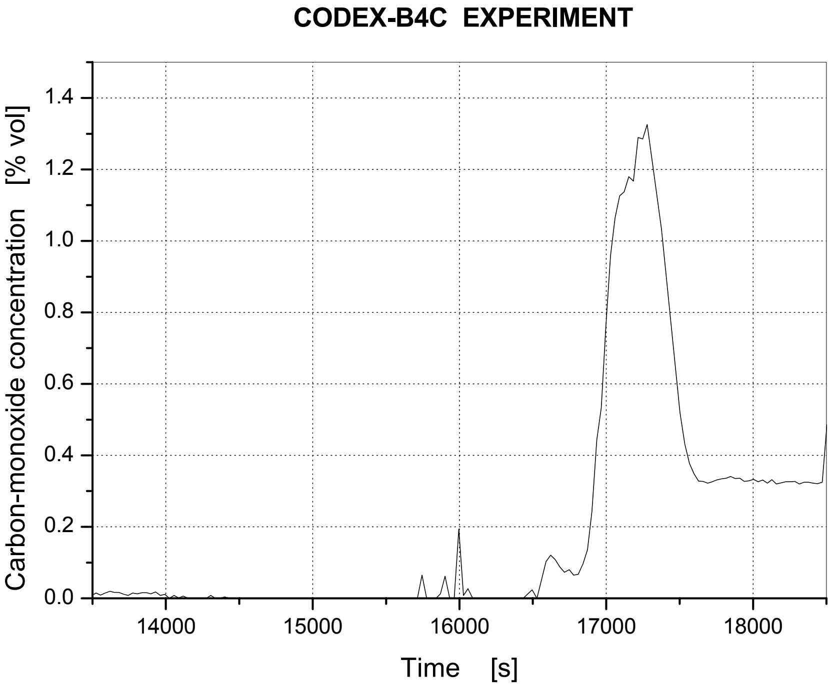

Fig. 67 COCON: Carbon-monoxide concentration

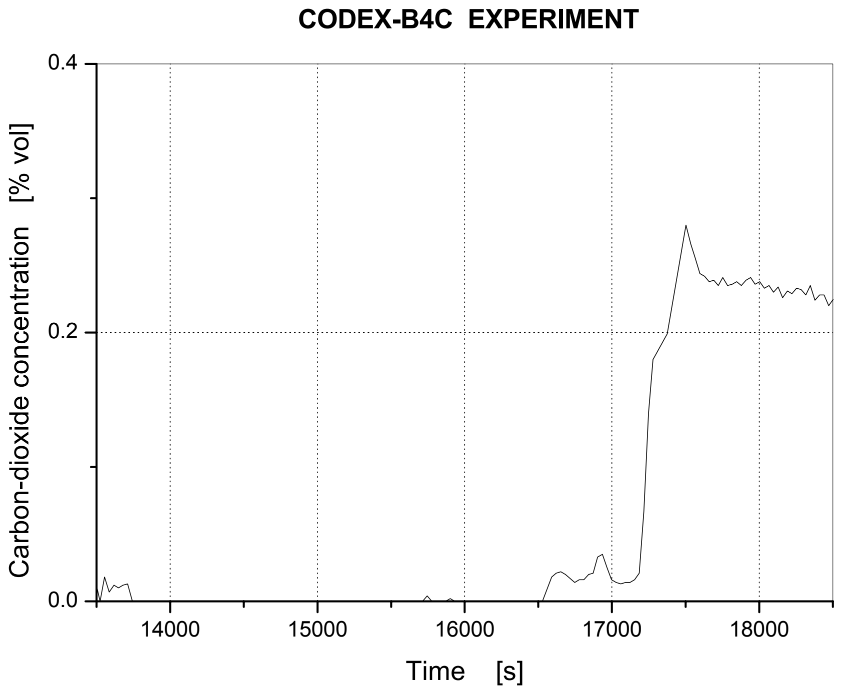

Fig. 68 CO2CON: Carbon-dioxide concentration

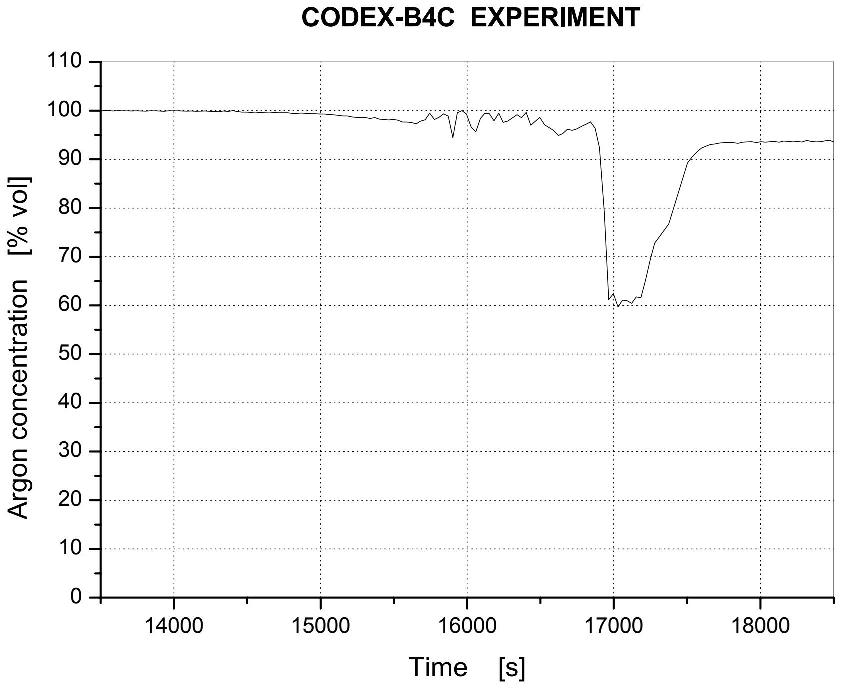

Fig. 69 ARCON: Argon concentration

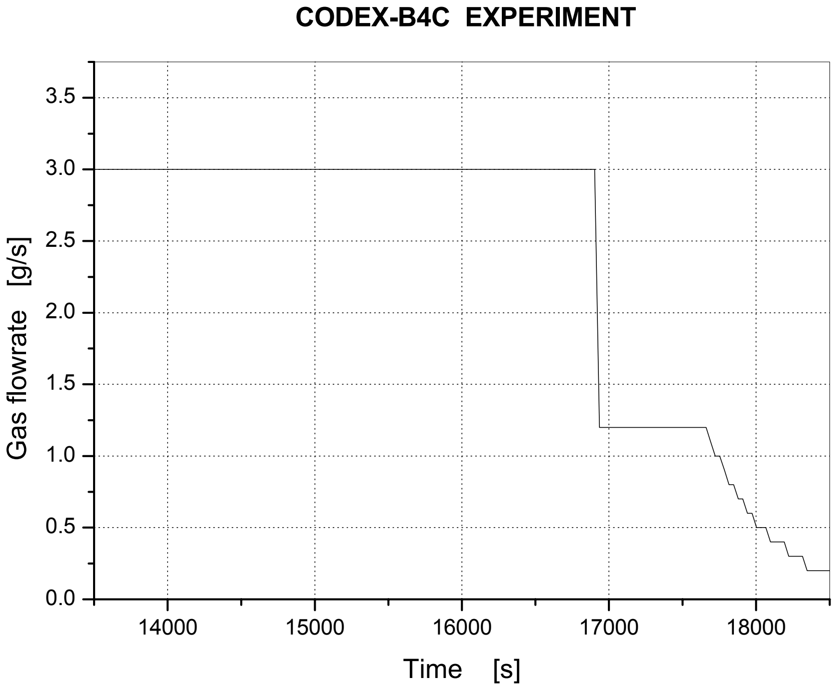

Fig. 70 MSFLOW: Mass flow at the mass spectrometer

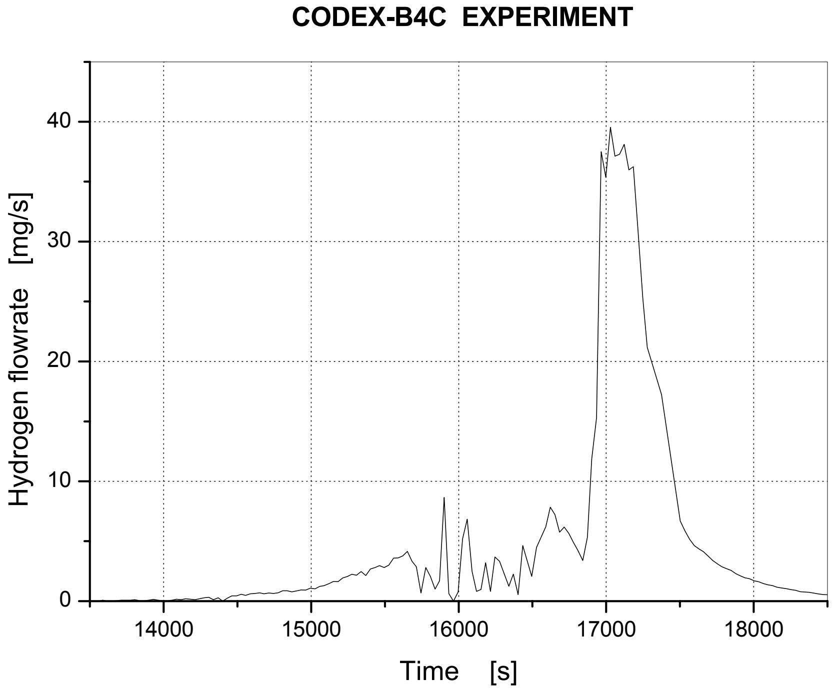

Fig. 71 H2: Hydrogen flowrate

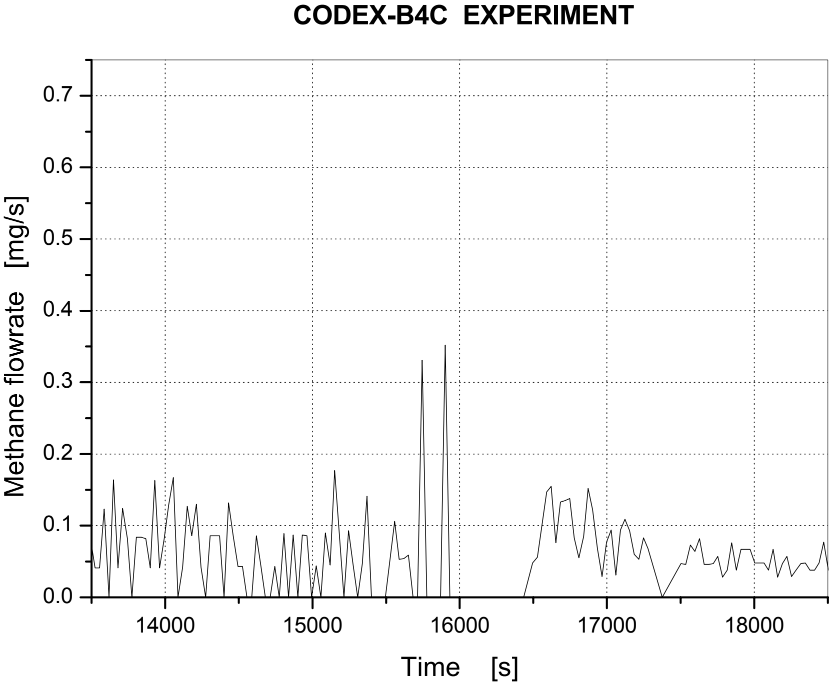

Fig. 72 CH4: Methane flowrate

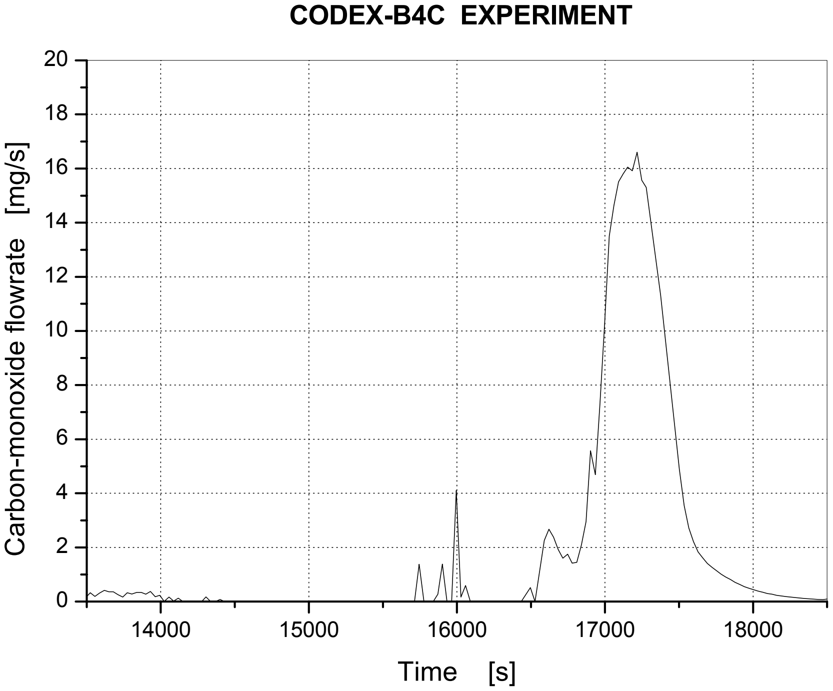

Fig. 73 CO: Carbon-monoxide flowrate

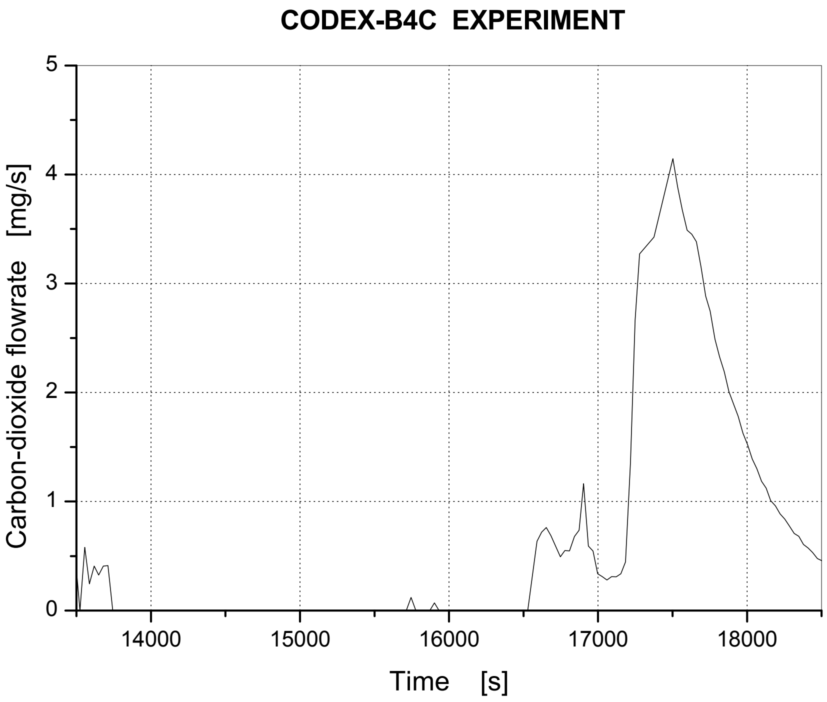

Fig. 74 CO2: Carbon-dioxide flowrate

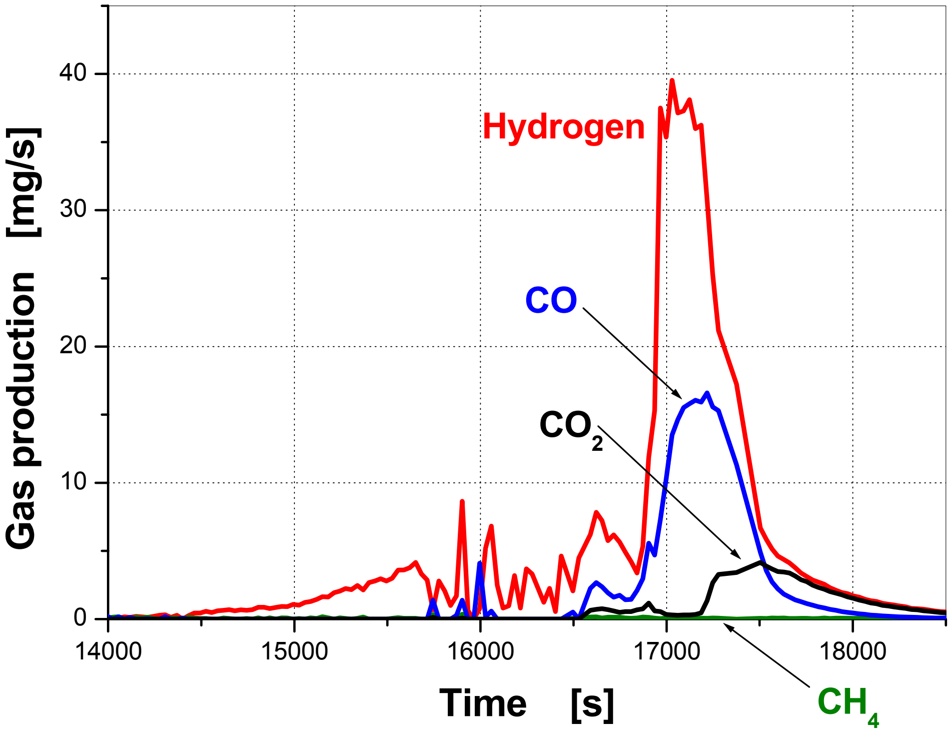

Fig. 75 Gas flowrates in the CODEX-B4C test

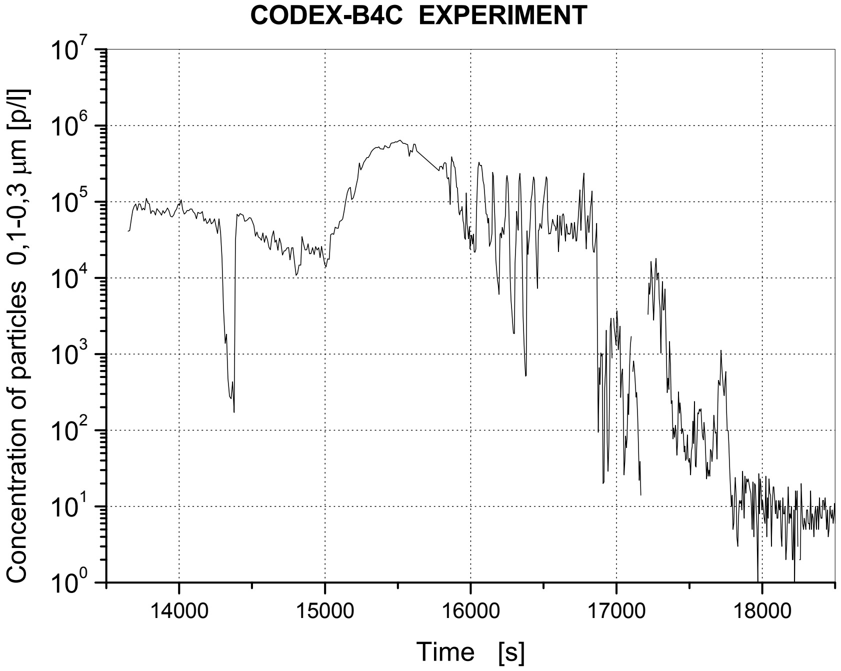

Fig. 76 API1: Concentration of 0,1-0,3 µm aerosols, internal counter

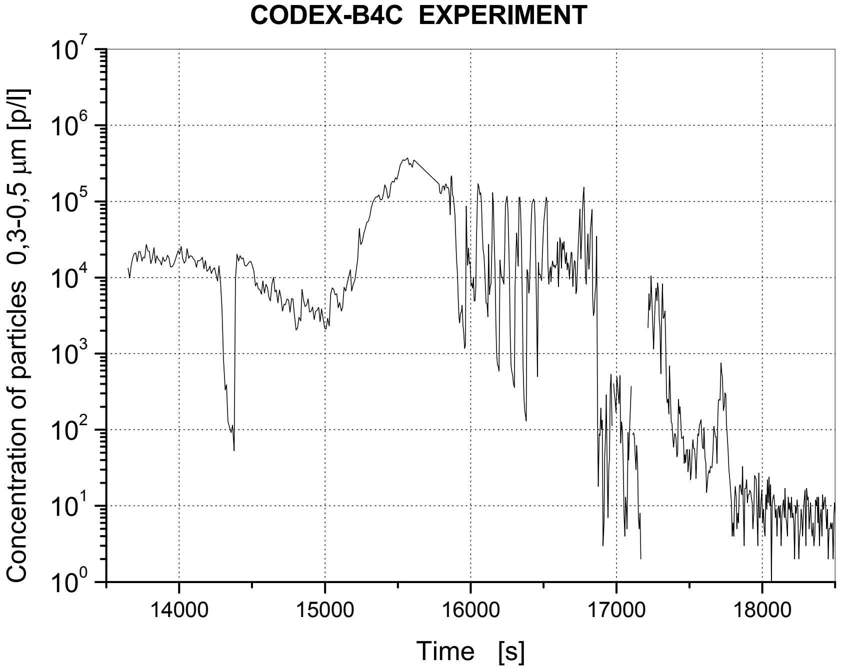

Fig. 77 API2: Concentration of 0,3-0,5 µm aerosols, internal counter

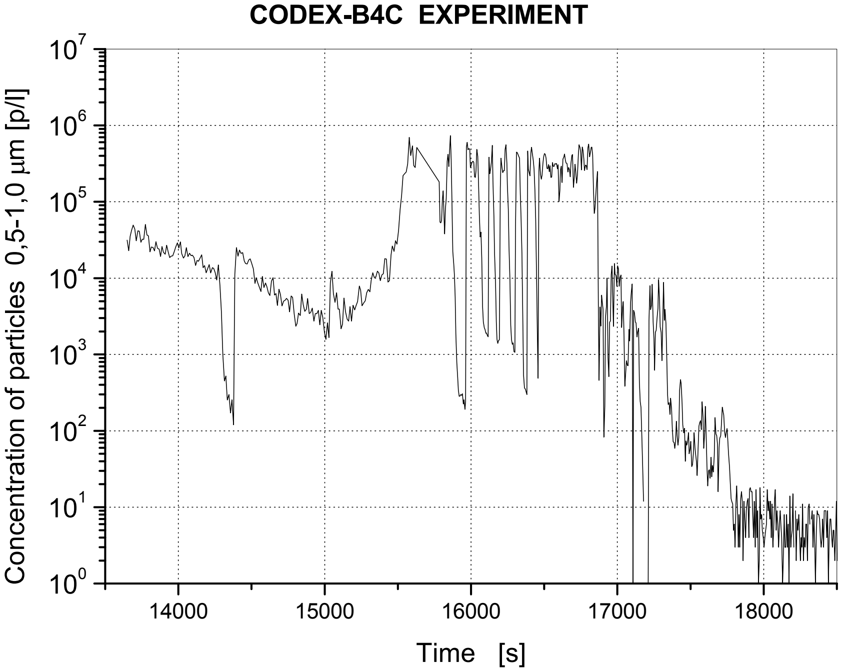

Fig. 78 API3: Concentration of 0,5-1,0 µm aerosols, internal counter

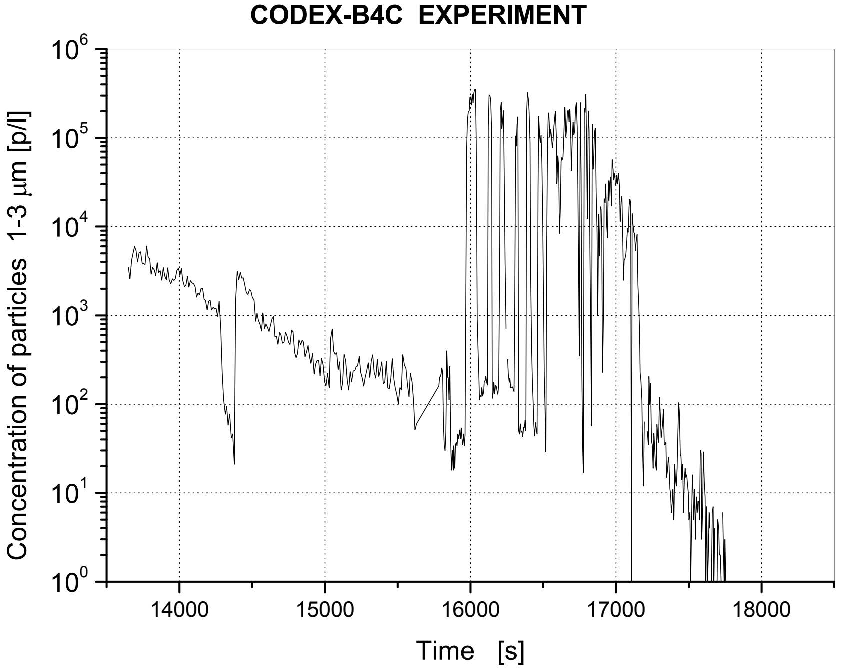

Fig. 79 API4: Concentration of 1-3 µm aerosols, internal counter

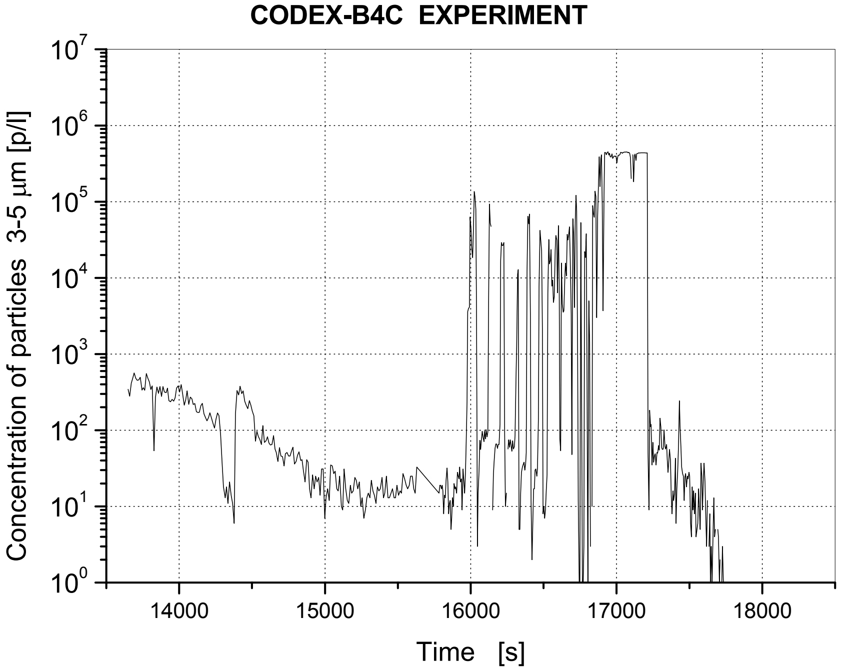

Fig. 80 API5: Concentration of 3-5 μm aerosols, internal counter

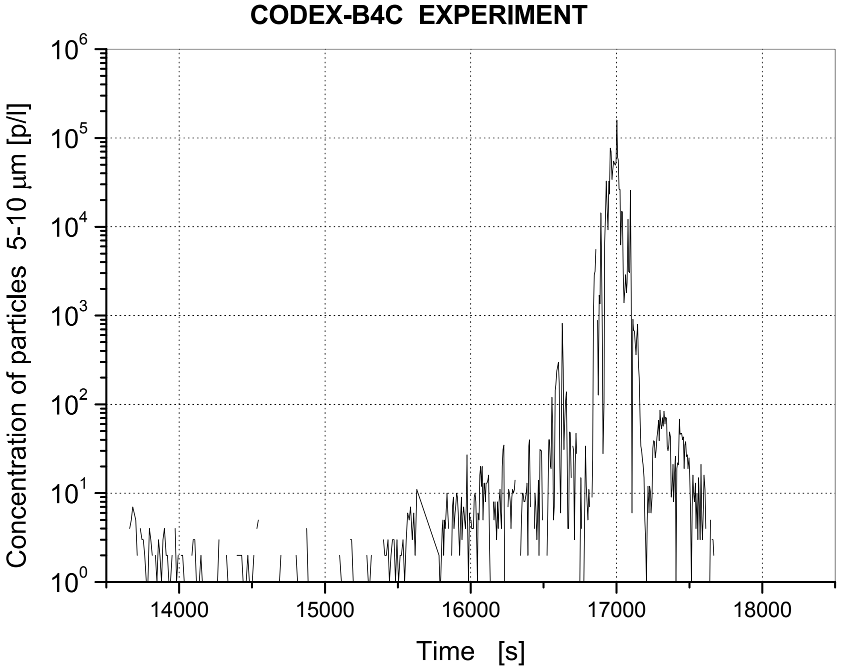

Fig. 81 API6: Concentration of 5-10 μm aerosols, internal counter

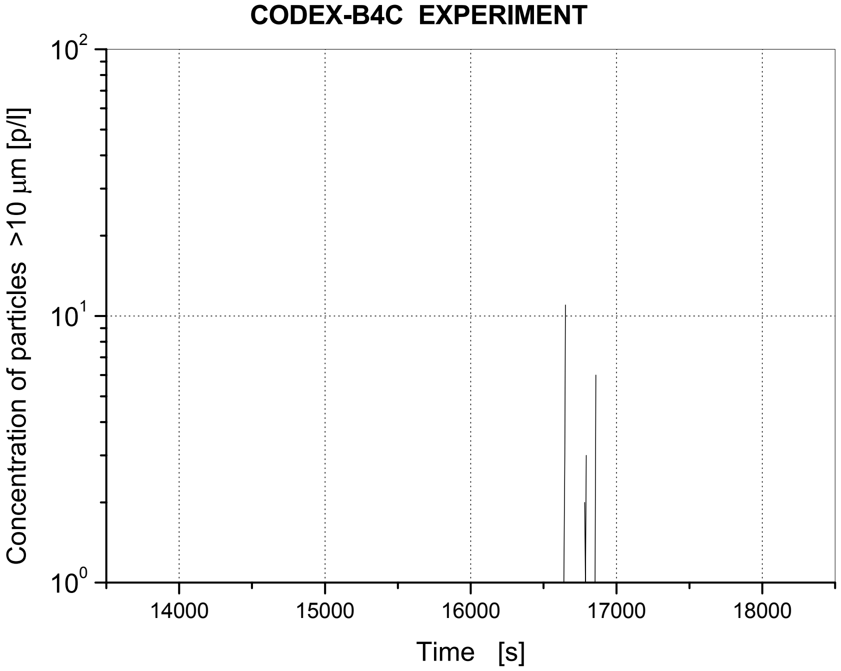

Fig. 82 API7: Concentration of >10 µm aerosols, internal counter

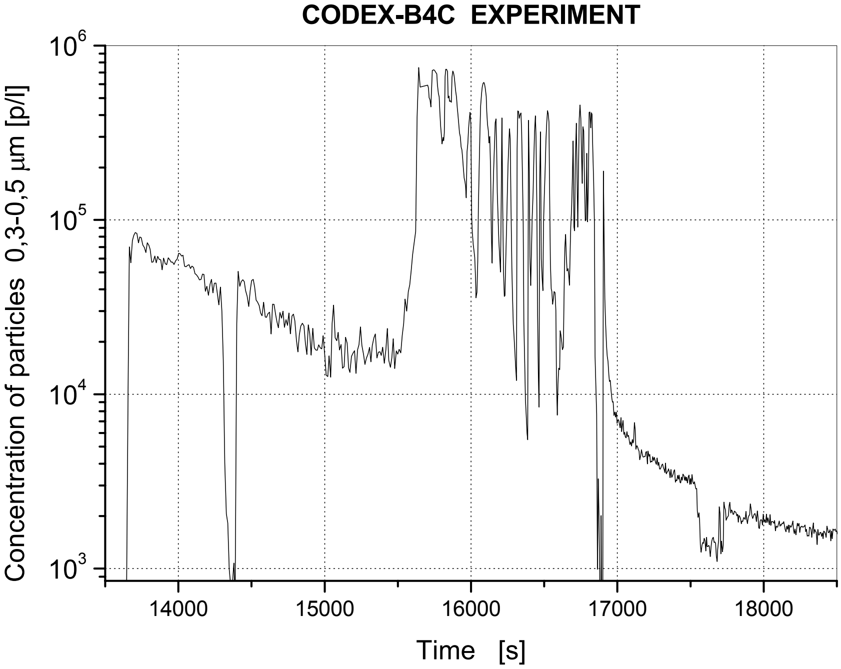

Fig. 83 APE1: Concentration of 0,3-0,5 µm aerosols, external counter

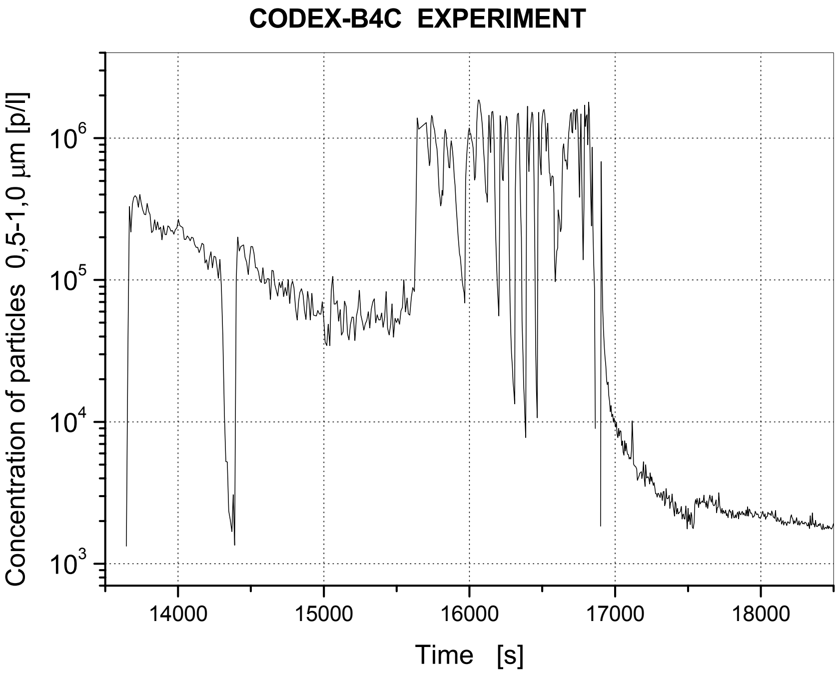

Fig. 84 APE2: Concentration of 0,5-1,0 μm aerosols, external counter

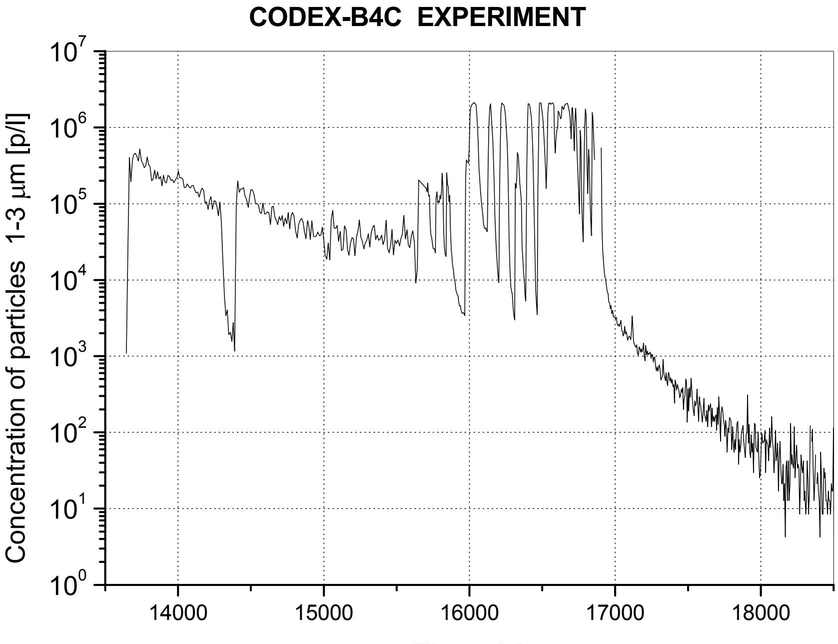

Fig. 85 APE3: Concentration of 1-3 μm aerosols, external counter

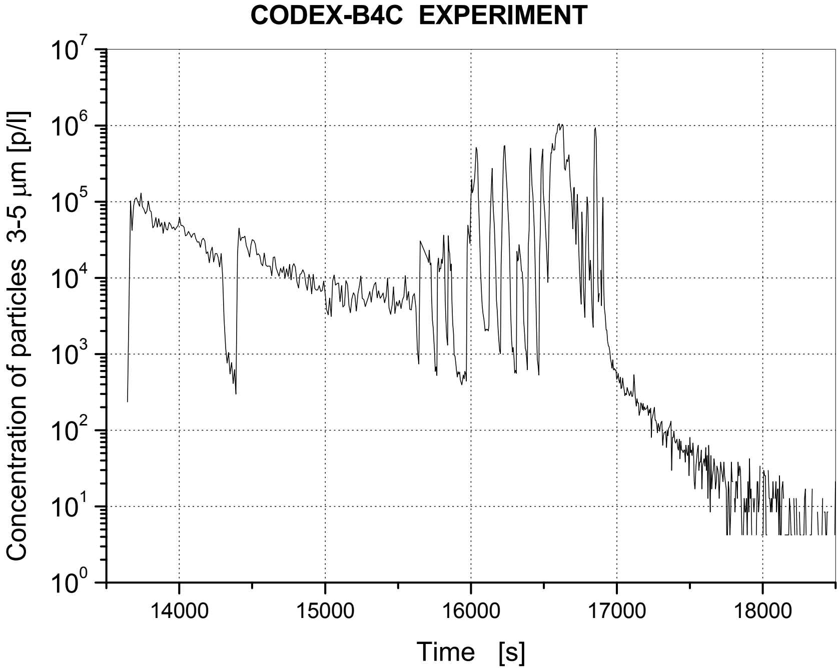

Fig. 86 APE4: Concentration of 3-5 µm aerosols, external counter

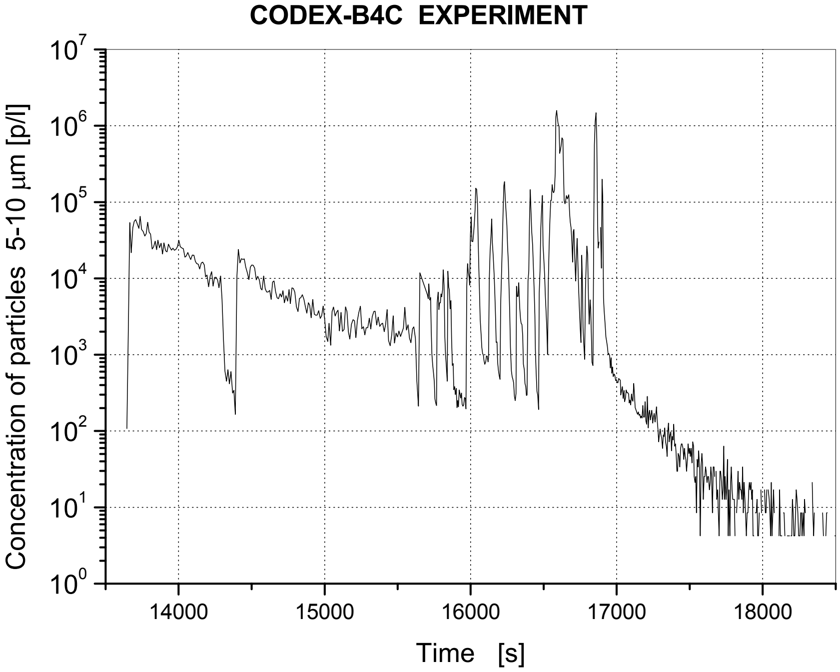

Fig. 87 APE5: Concentration of 5-10 µm aerosols, external counter

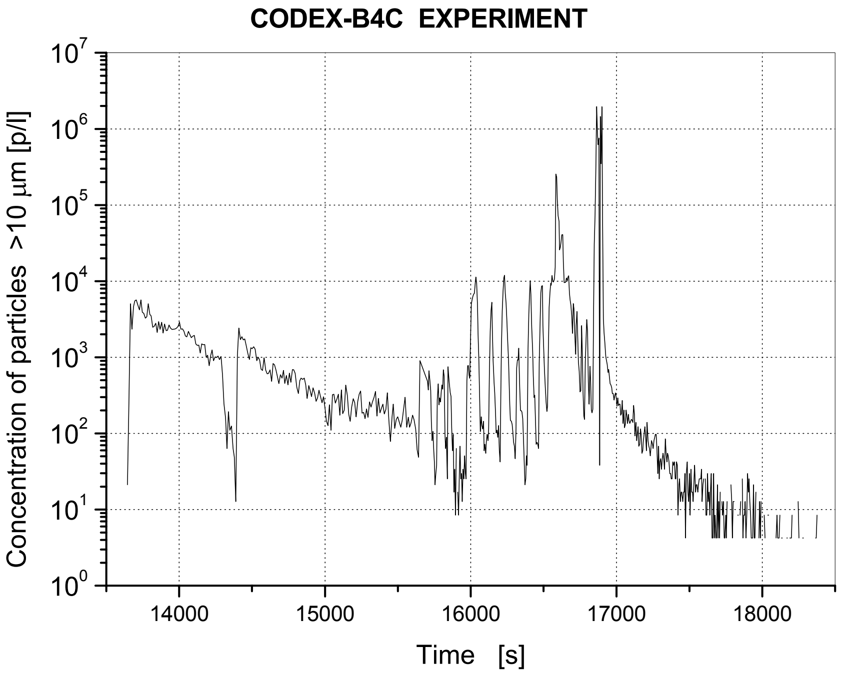

Fig. 88 APE6: Concentration of >10 µm aerosols, external counter

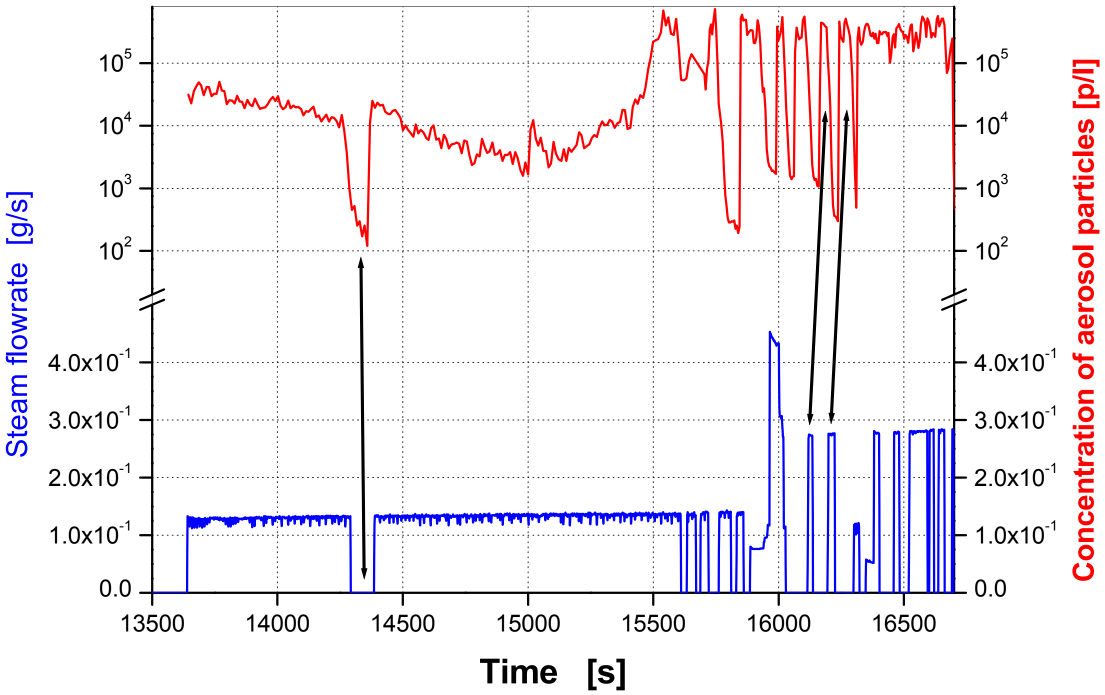

Fig. 89 Correlation between steam flowrate and aerosol particle concentration

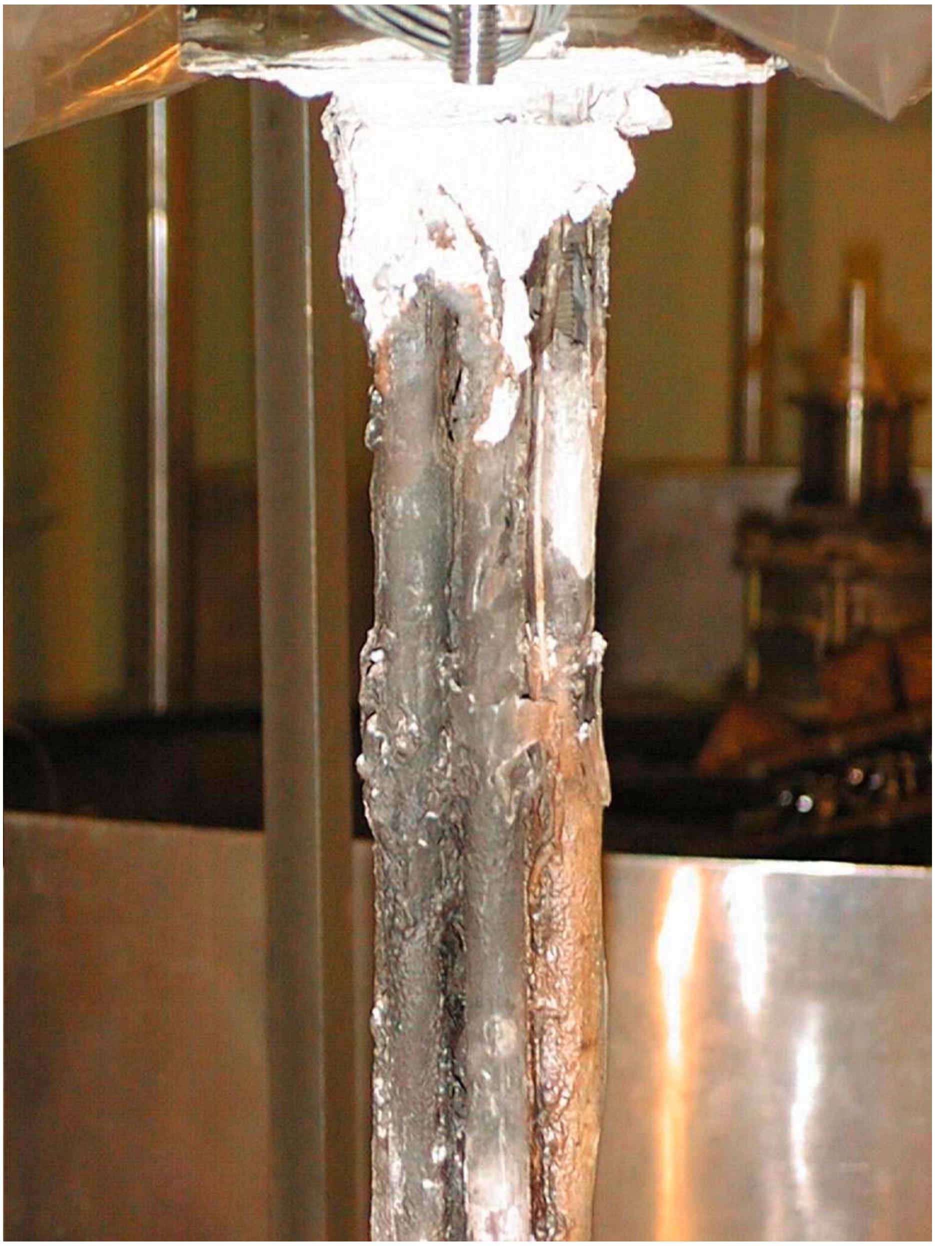

Fig. 90 View of the upper part of the CODEX-B4C bundle

Fig. 91 View of the CODEX-B4C bundle with shroud

Fig. 92 View of the CODEX-B4C bundle without shroud

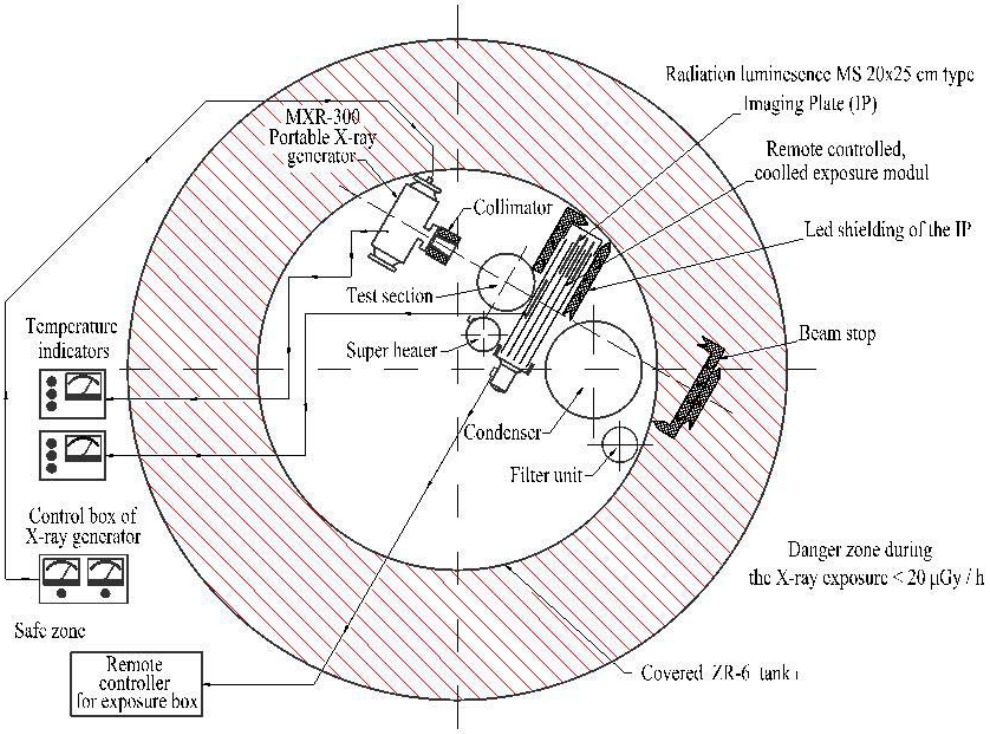

Fig. 93 Arrangement of X-ray radiography equipment during the CODEX-B4C test

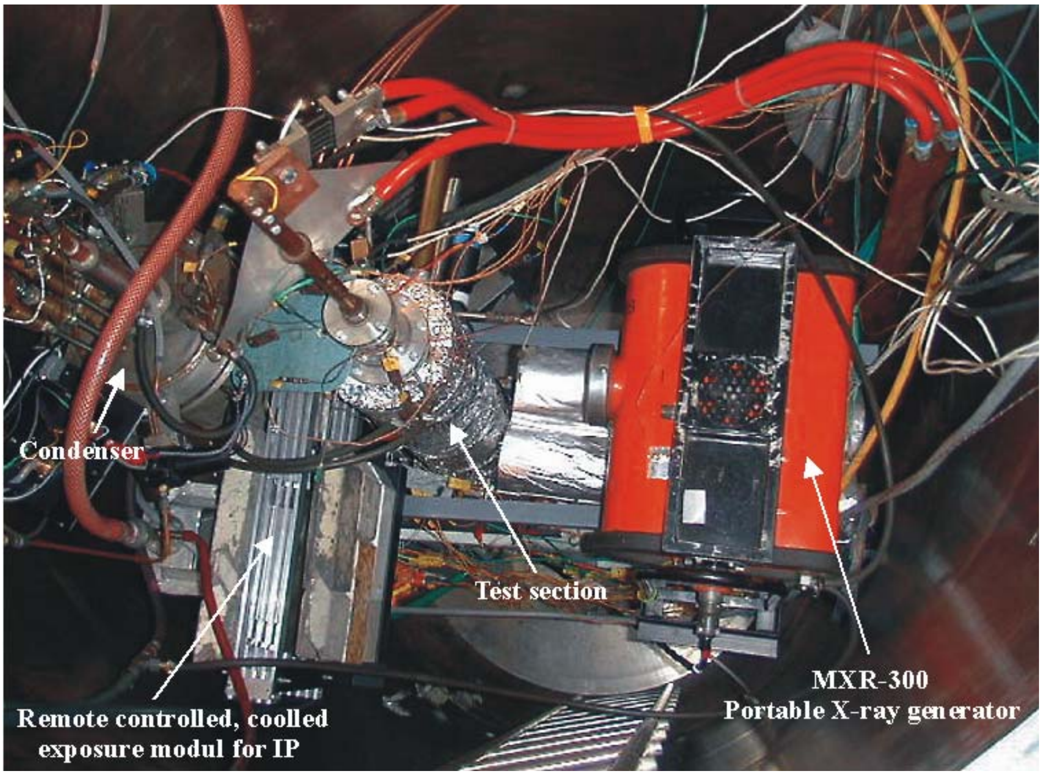

Fig. 94 View of the top of the CODEX facility with X-ray radiography equipment

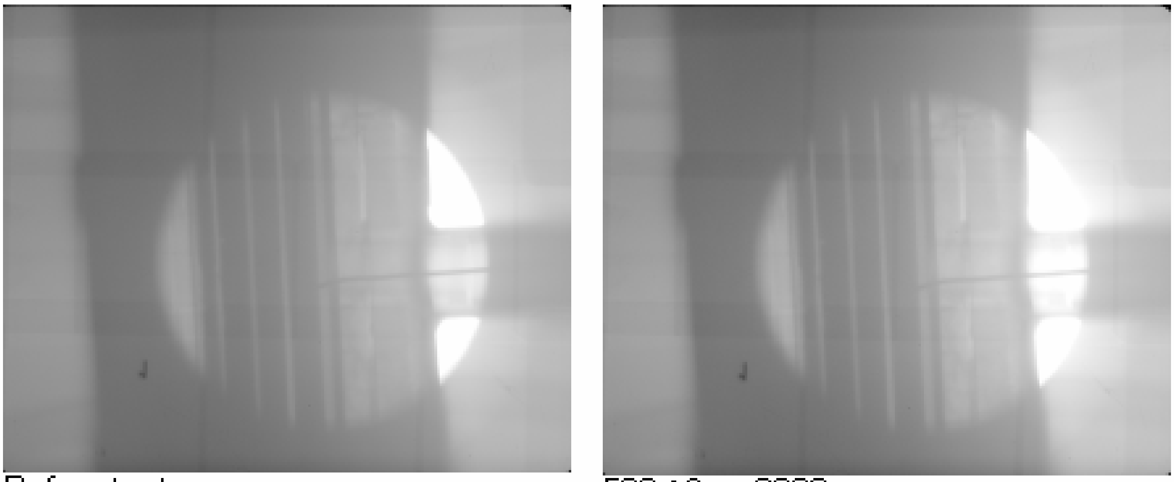

Before test

530 °C 6600 s

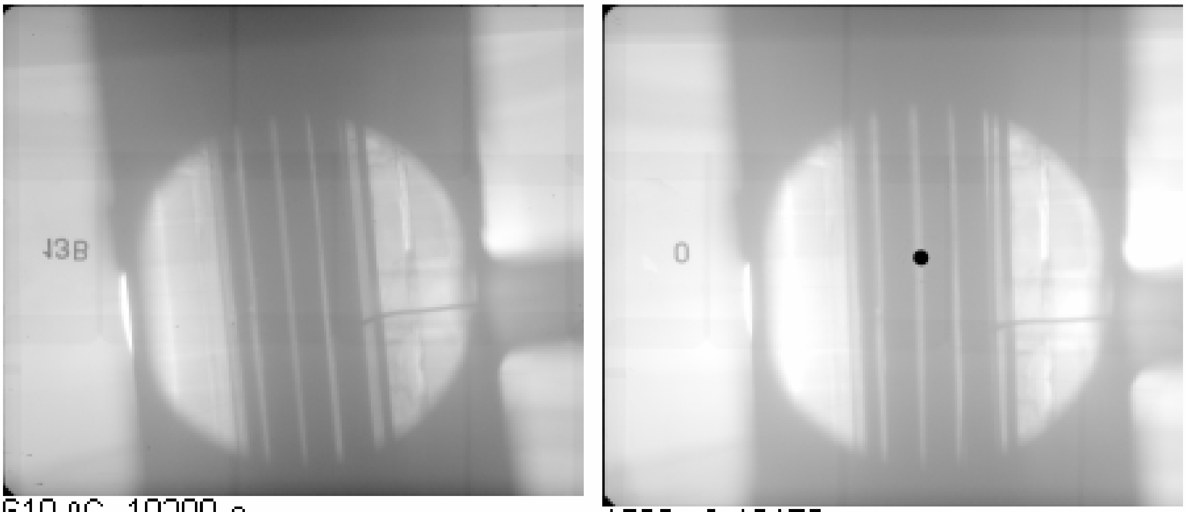

610 °C 10200 s

1530 °C 16176 s

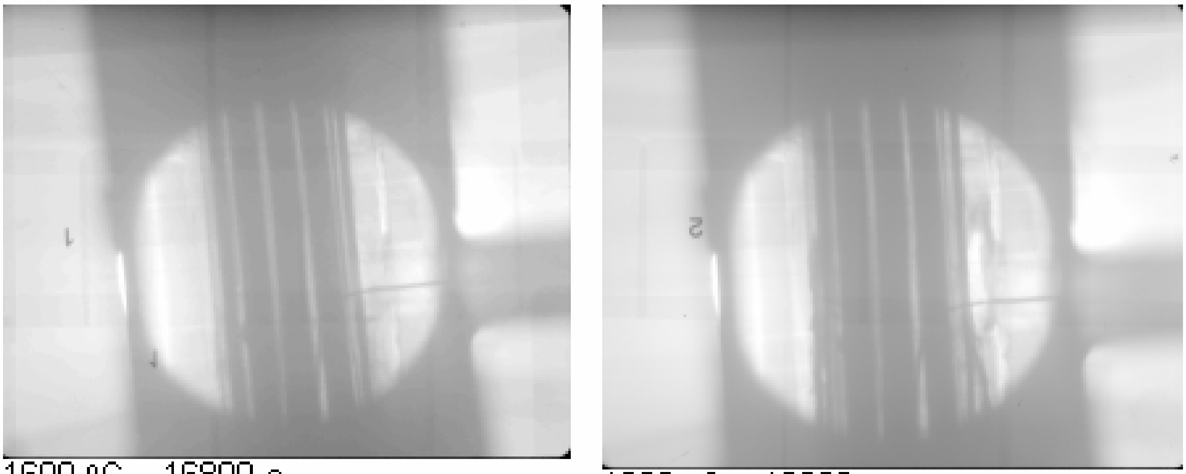

1600 °C 16800 s

1800 °C 16900 s

Fig. 95 X-ray radiography view of the upper part of the CODEX-B4C bundle at ~465 mm elevation (pictures taken before the test, at 6600 s, 10200 s, 16176 s, 16800 s and 16900 s)

2000 °C 17000 s

590 °C 20400 s

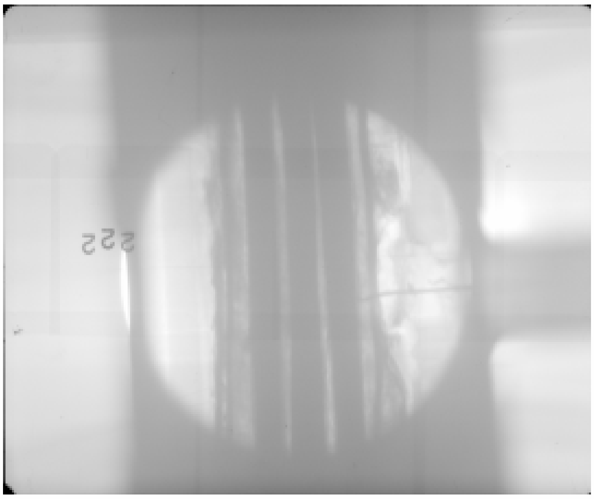

after test

Fig. 96 X-ray radiography view of the upper part of the CODEX-B4C bundle at ~465 mm elevation (pictures taken at 17000 s, 20400 s and after the test)

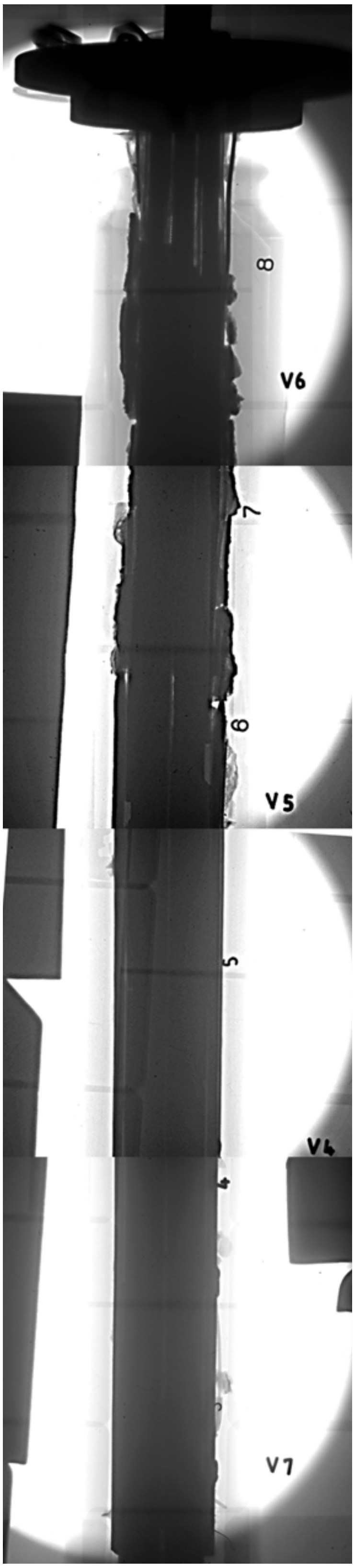

Fig. 97 X-ray radiography of the CODEX-B4C bundle after the experiment

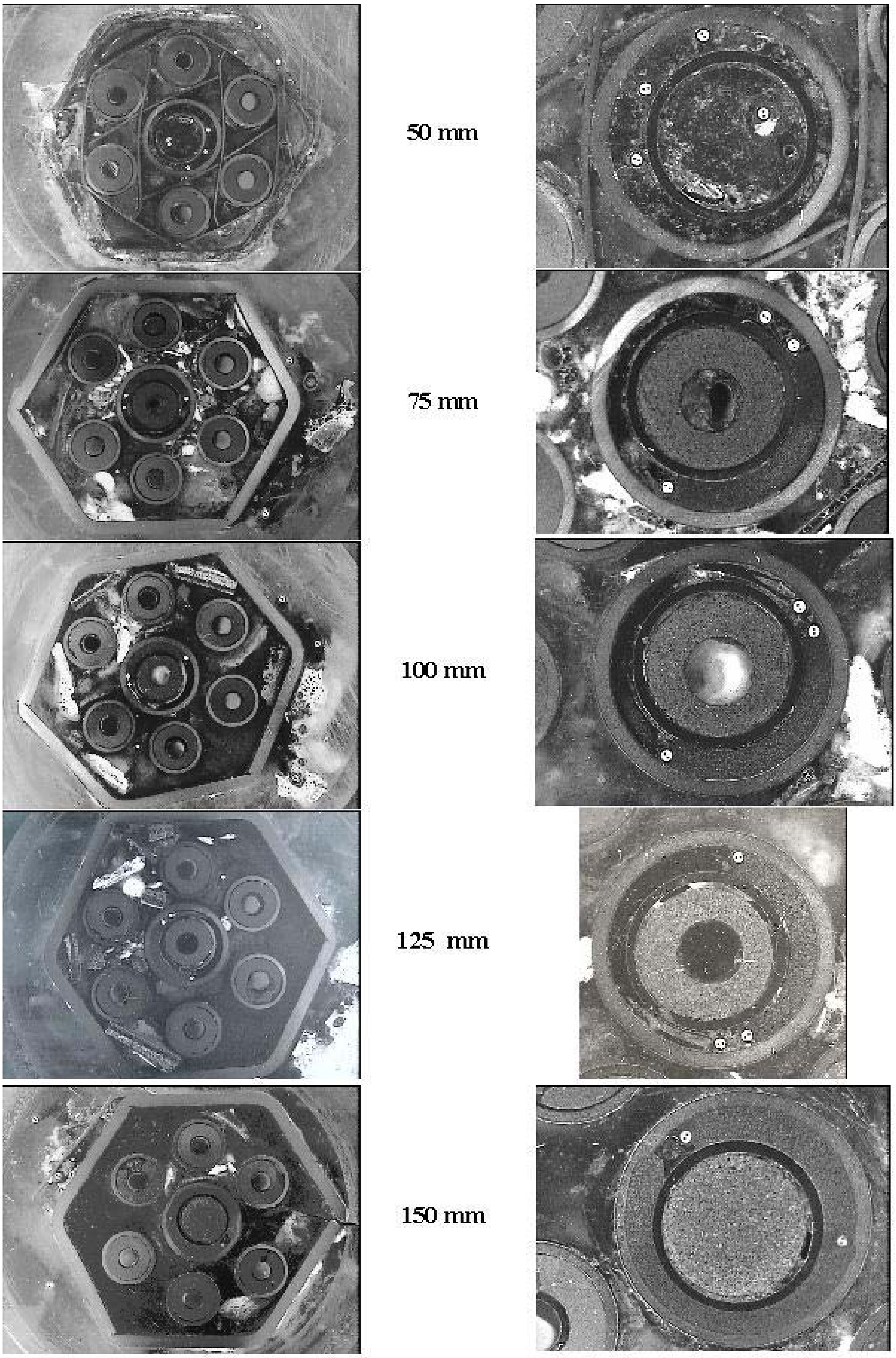

Fig. 98 Bundle cross sections (left column) and view of the control rod (right column) at elevations 50 mm, 75 mm, 100 mm, 125 mm, 150 mm

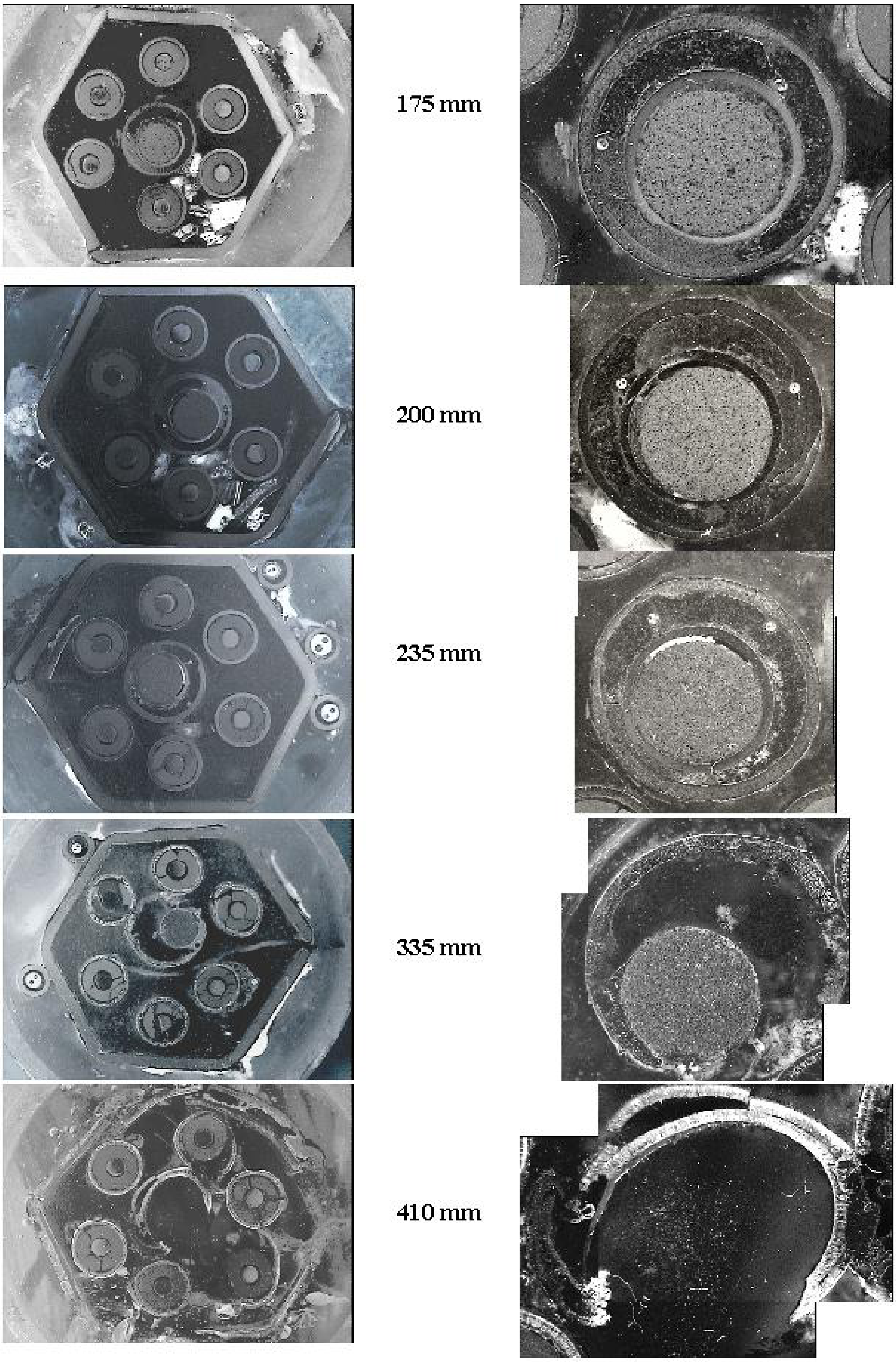

Fig. 99 Bundle cross sections (left column) and view of the control rod (right column) at elevations 175 mm, 200 mm, 235 mm, 335 mm, 410 mm

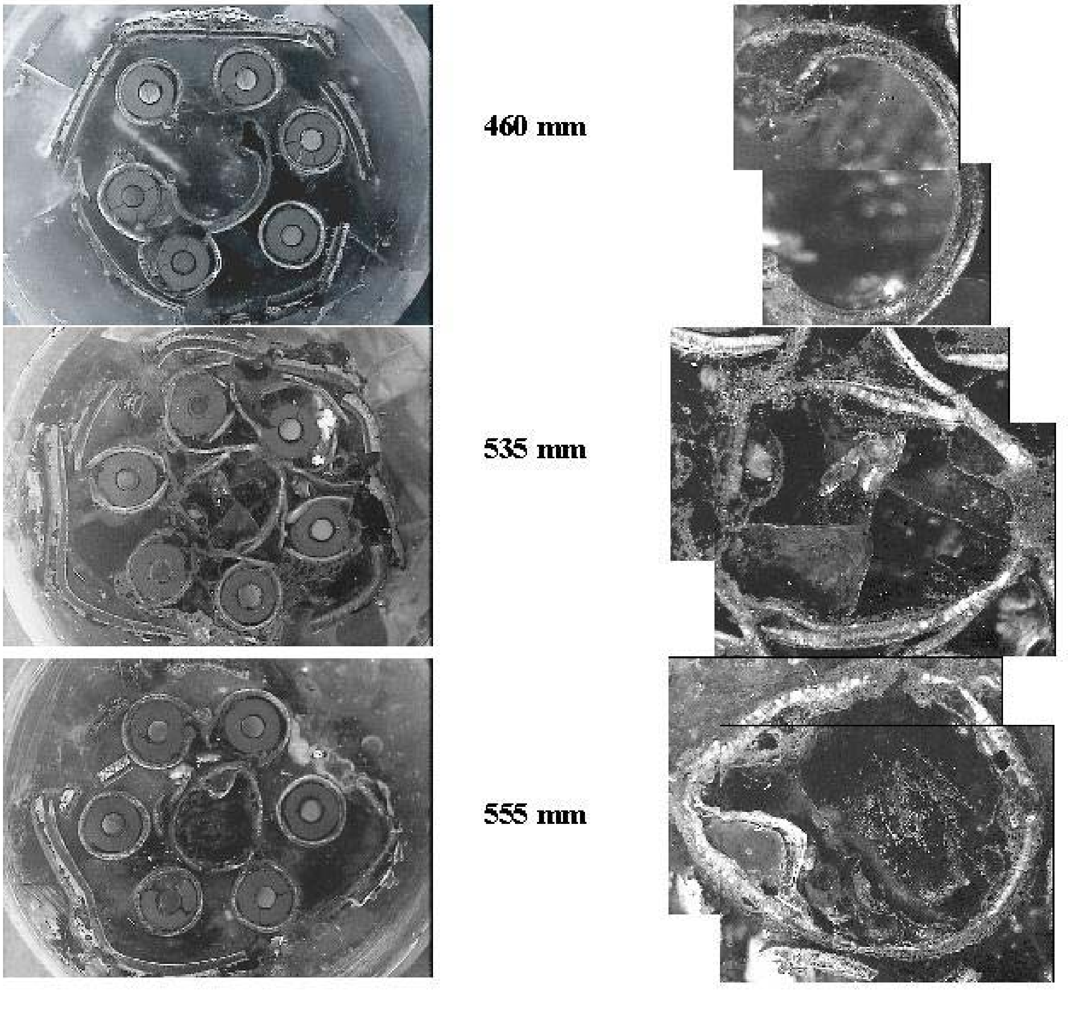

Fig. 100 Bundle cross sections (left column) and view of the control rod (right column) at elevations 460 mm, 535 mm, 555 mm

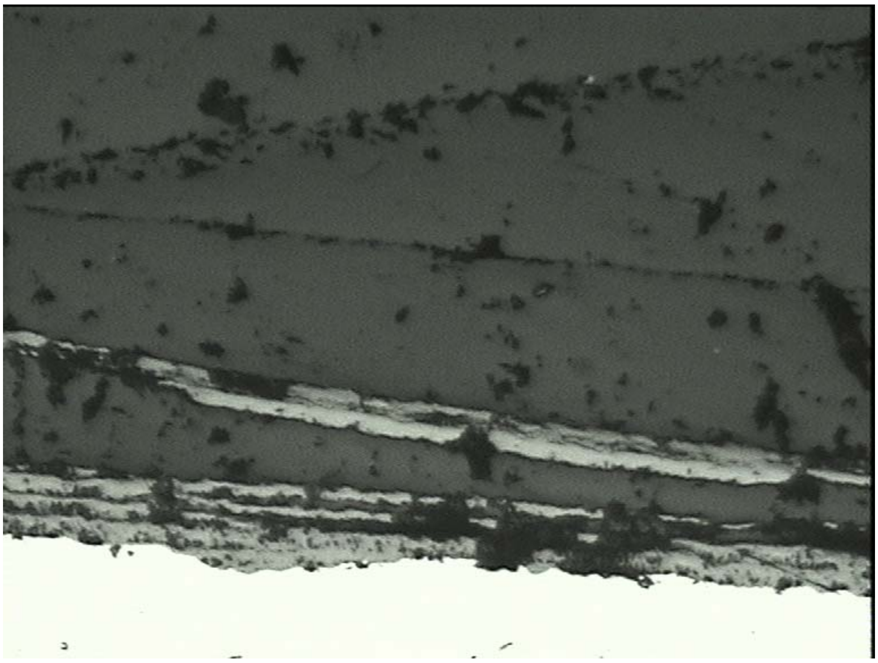

Fig. 101 Layered oxide scale on heated rod No.4 at 125 mm elevation.

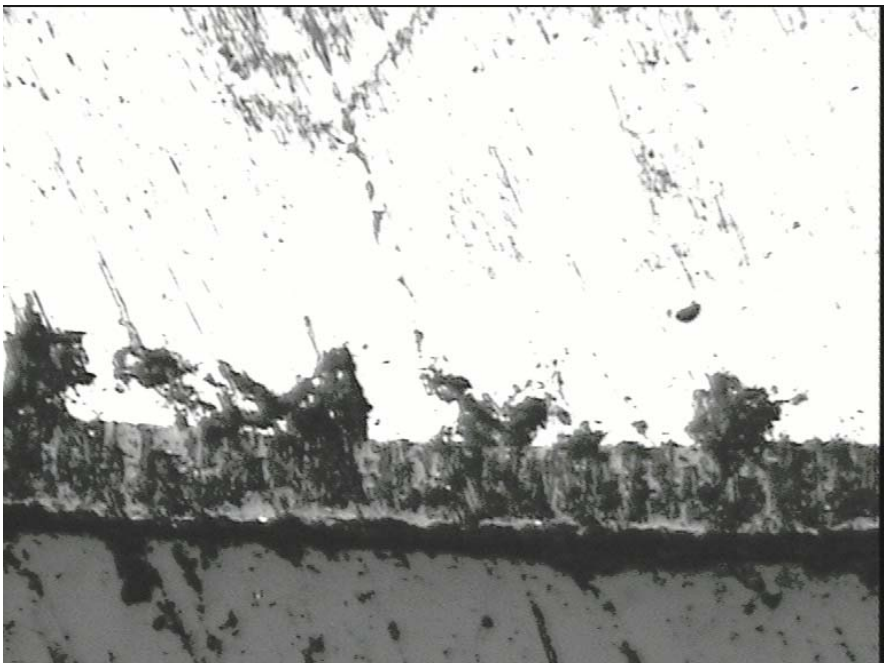

Fig. 102 Oxide layer on heated rod Nr.6 at 175 mm elevation

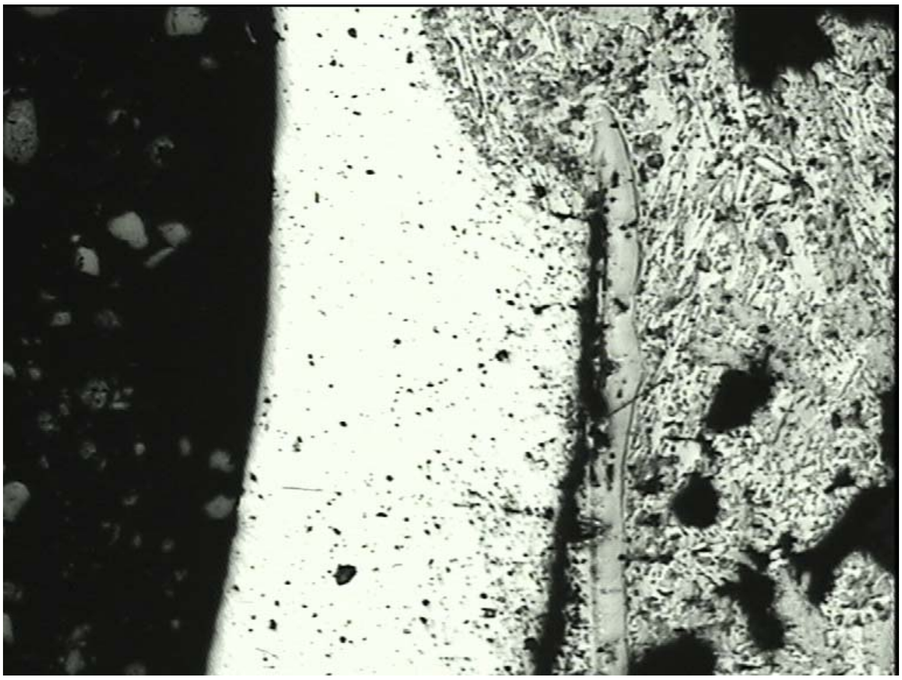

Fig. 103 Thinning of stainless steel cladding of B_4C at 200 mm elevation

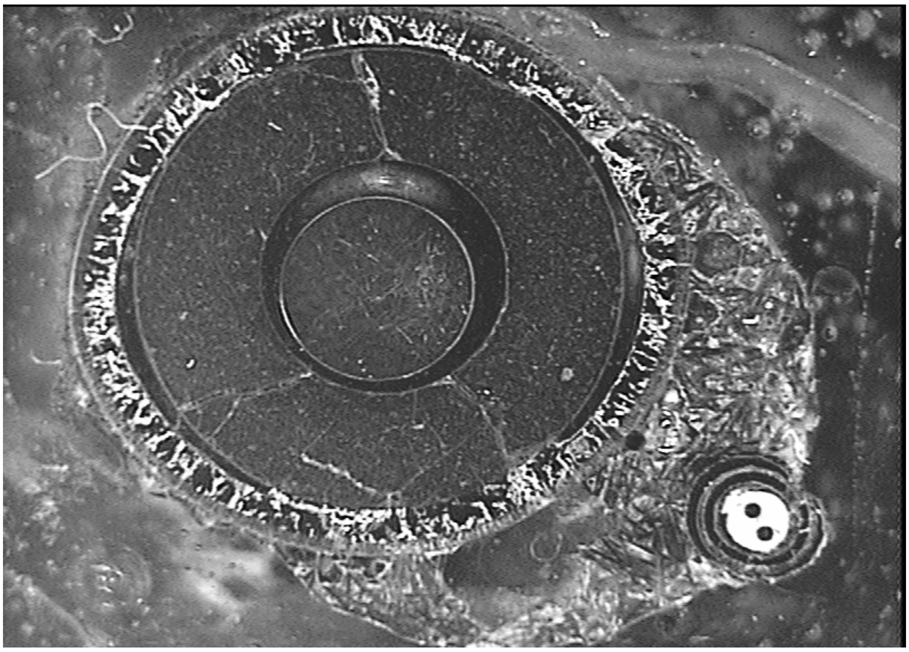

Fig. 104 A heated rod cut at 335 mm elevation. (No.3.)

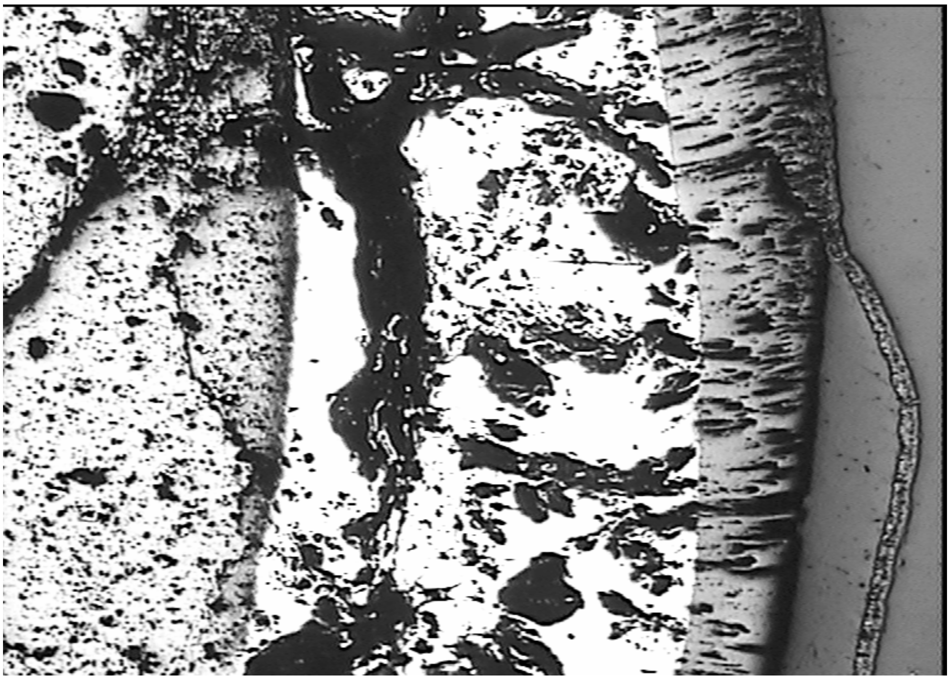

Fig. 105 A heated rod cut at 335 mm elevation. (No.6.)

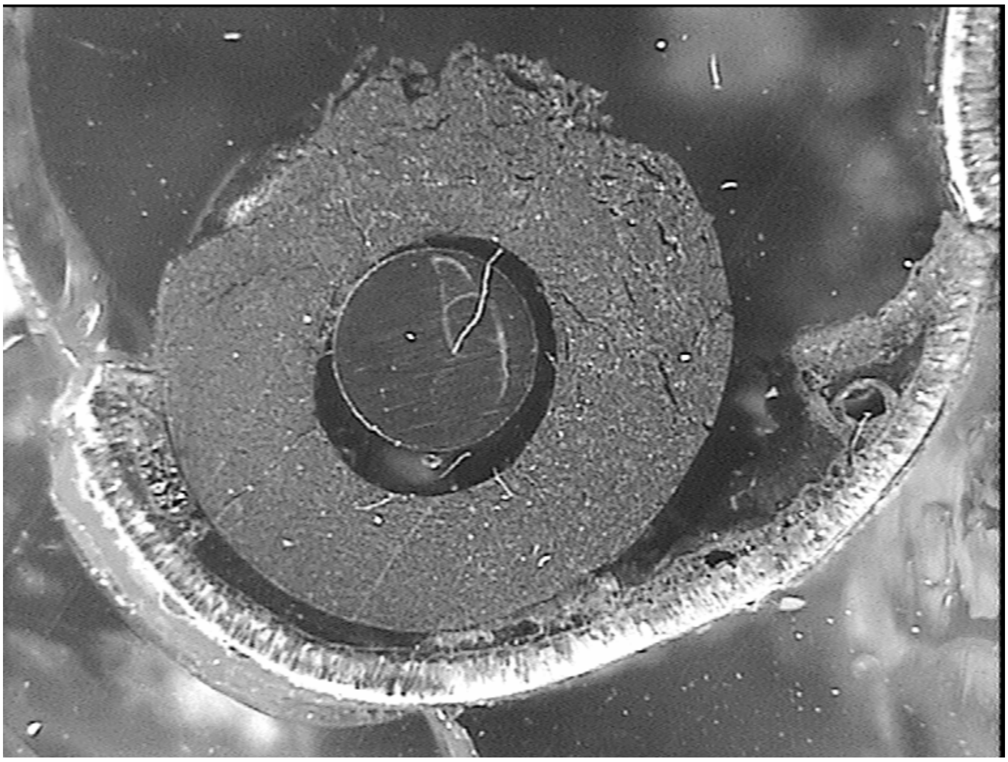

Fig. 106 Partly oxidized pellet at 410 mm elevation (Rod No.4.)

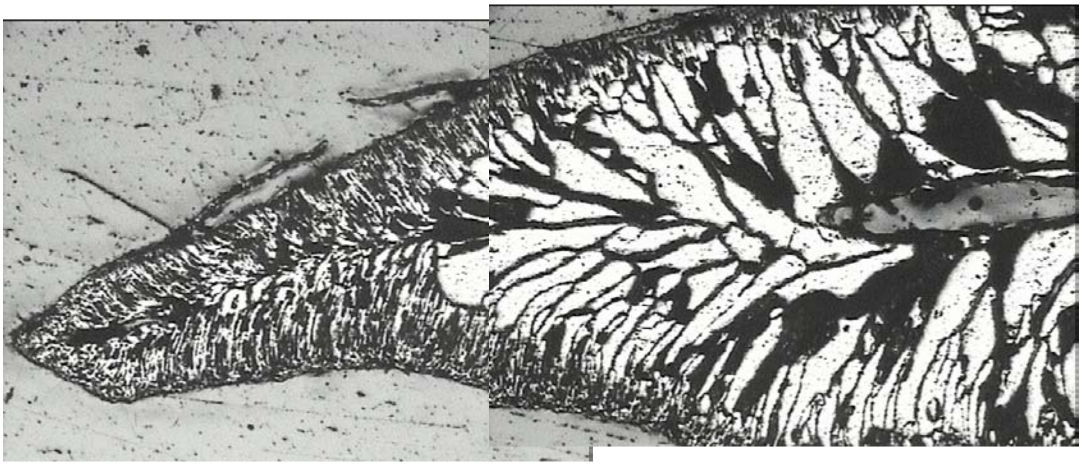

Fig. 107 Oxidized control rod guide tube at 410 mm elevation.

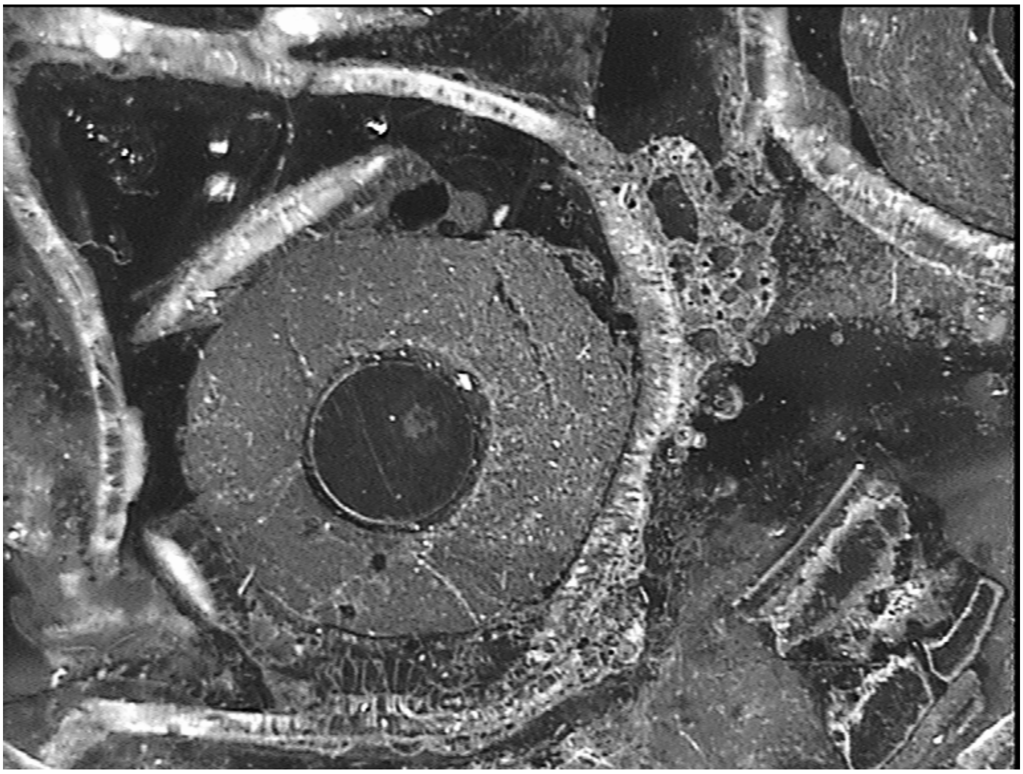

Fig. 108 Heated rod No.3 at 535 mm elevation

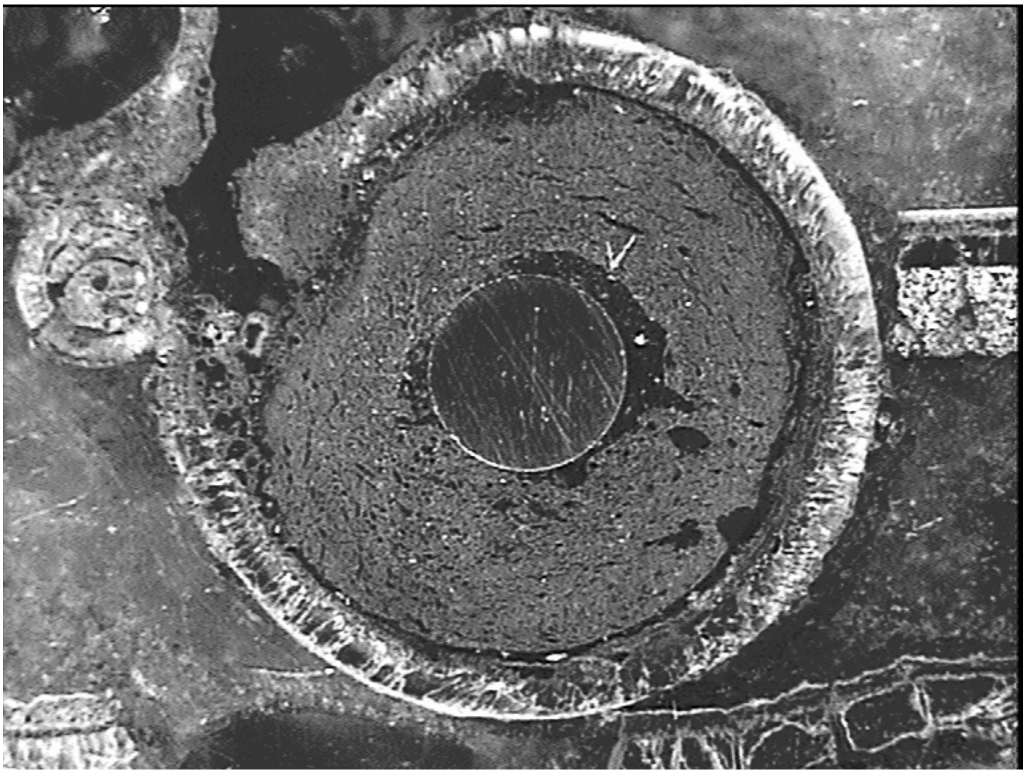

Fig. 109 Chemical interactions between cladding, pellet and thermocouple inlet metal shielding at 555 mm elevation

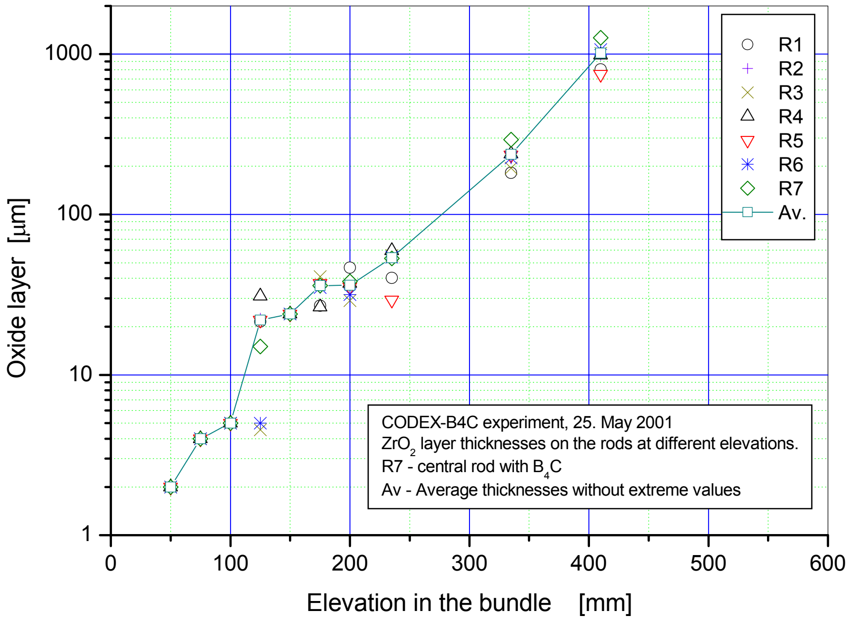

Fig. 110 Rod average oxide layer thickness on zirconium cladding as function of bundle elevation

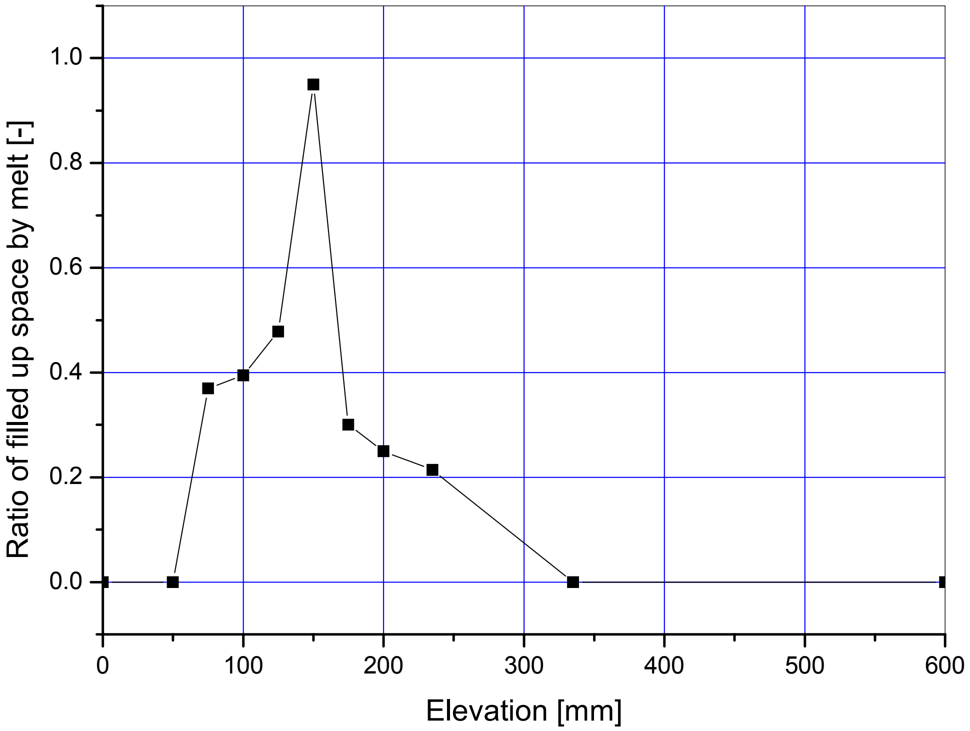

Fig. 111 Ratio of the molten material volume to the total volume of the gap in the guide tube as function of bundle elevation

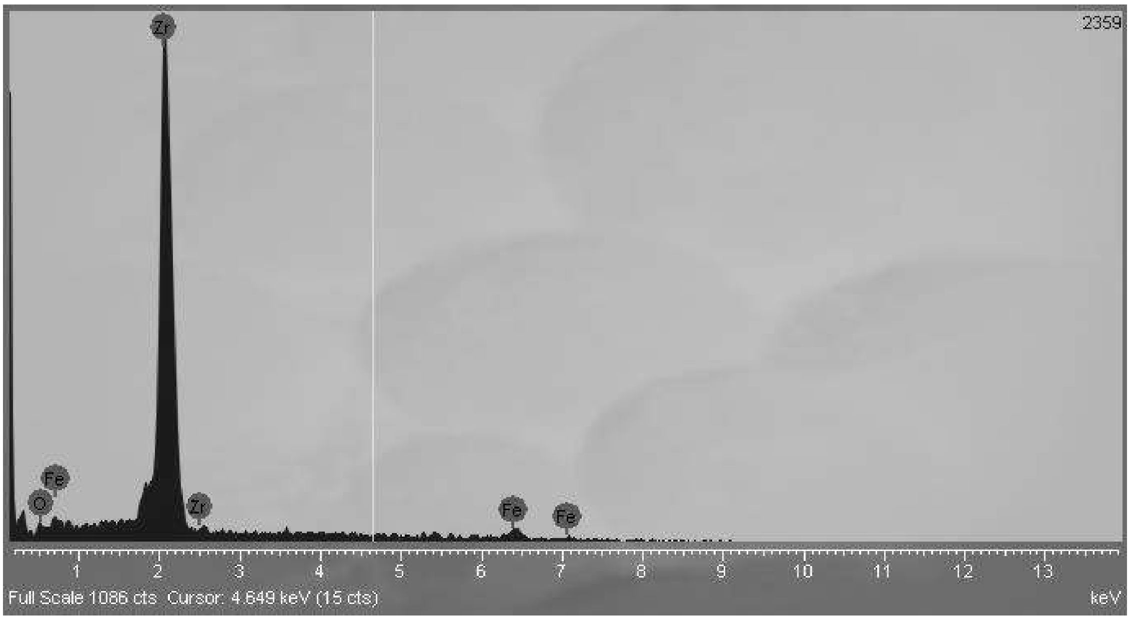

Fig. 112 EDX spectrum taken from the molten metall between the guide tube and control rod cladding at 235 mm elevation

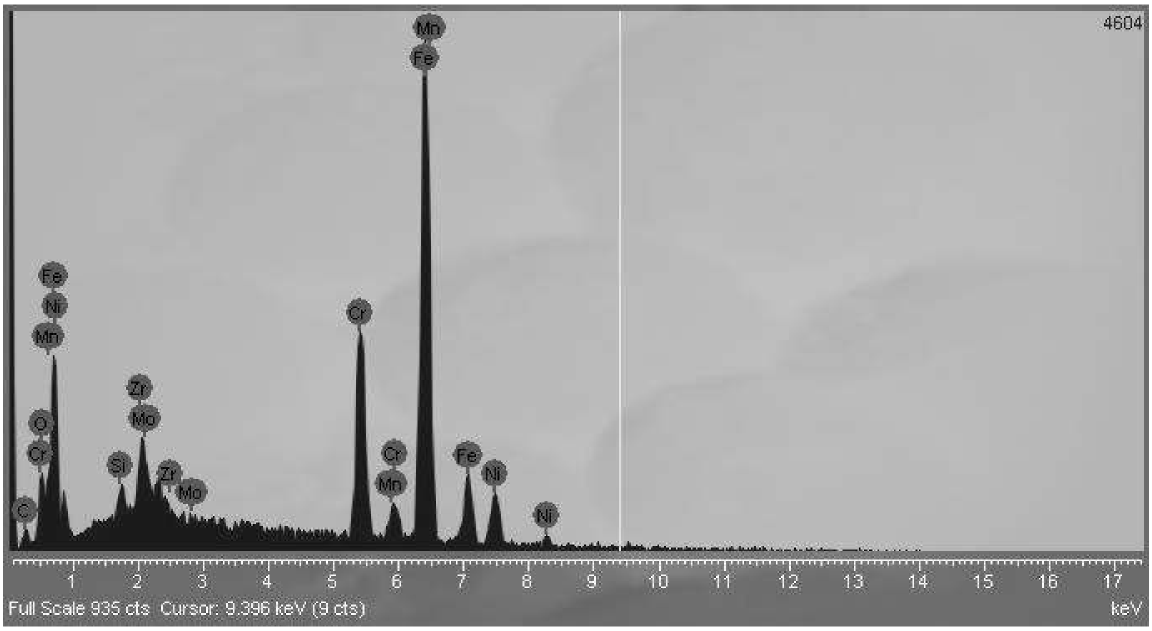

Fig. 113 EDX spectrum for Fe-Cr-Ni rich aggregate at 460 mm elevation

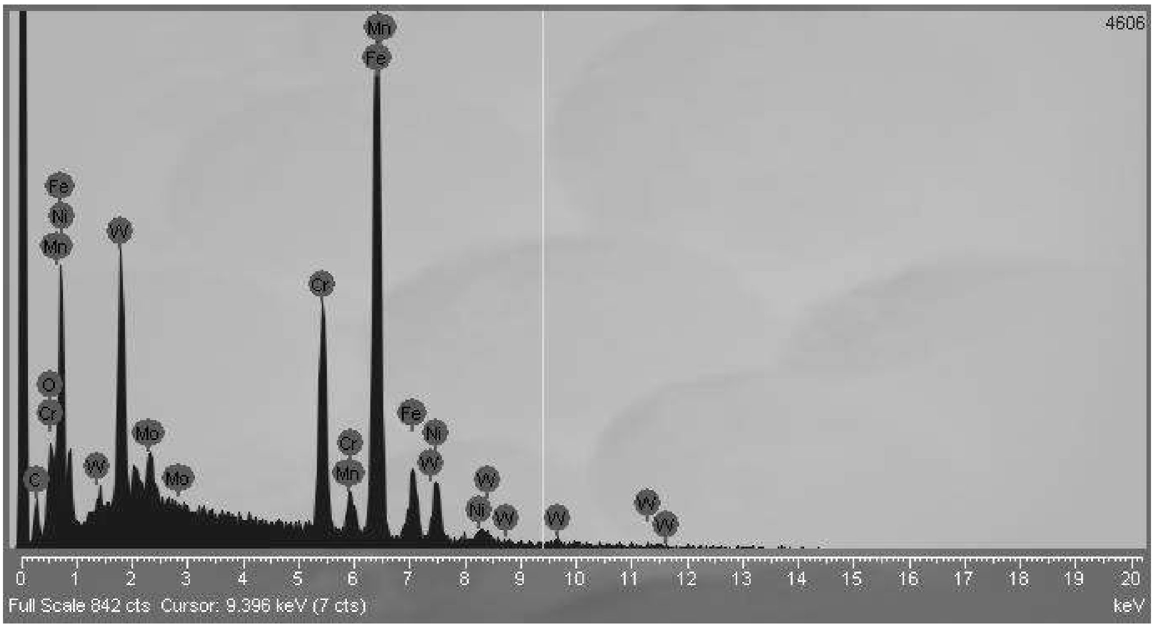

Fig. 114 EDX spectrum for an aggregate with steel components and W at 460 mm elevation

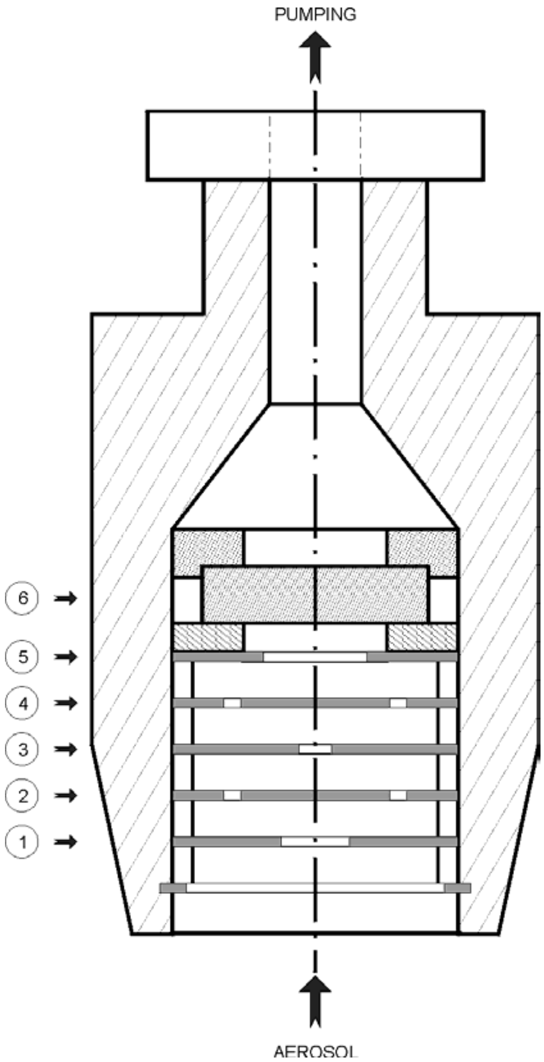

6 – quartz fiber filter
5 – stream limiter
4 – 2nd collector (sample D)
3 – 2nd nozzle
2 – 1st collector (sample B)
1 – 1st nozzle

Fig. 115 Scheme of impactor sampler

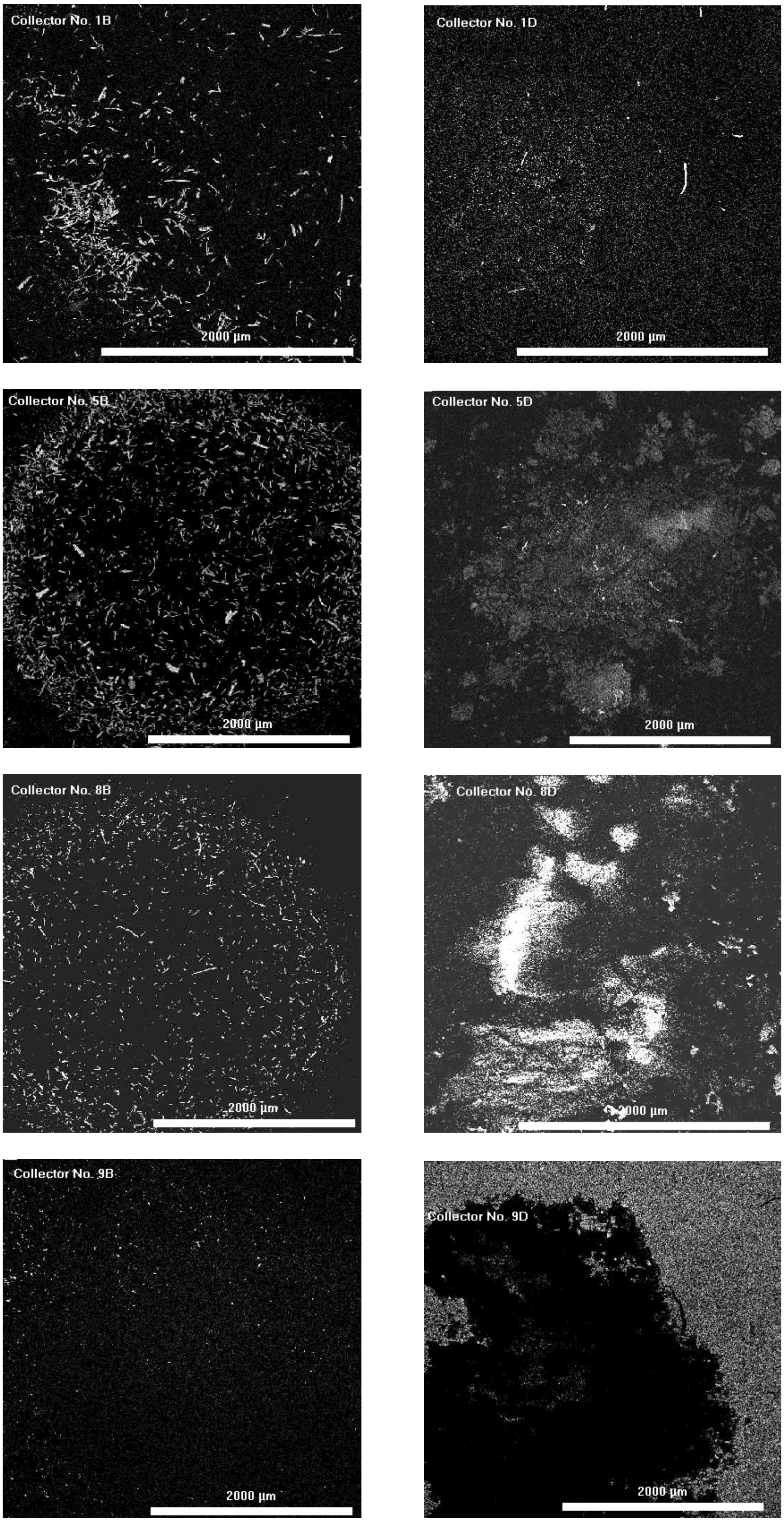

Fig. 116 Digital SEM images of various collectors at small magnification

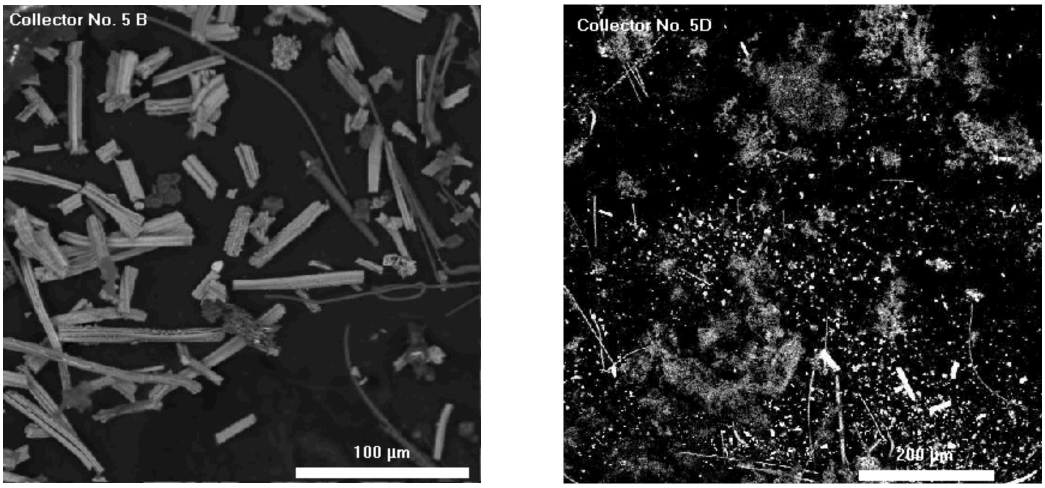

Fig. 117 Digital SEM images for two collector samples No. 5B and 5D, resp.

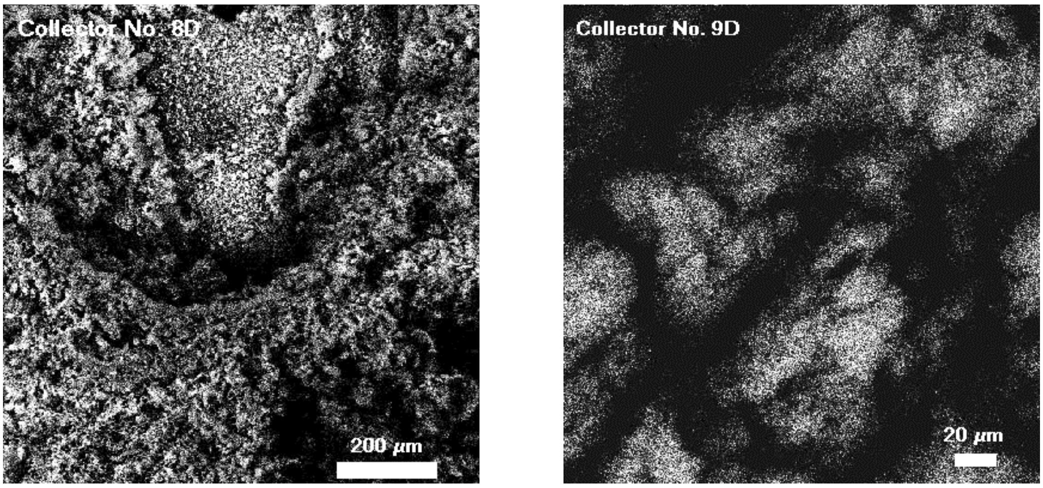

Fig. 118 Digital SEM images of aerosols settled on collectors No. 8D (left image) and 9D (right image).

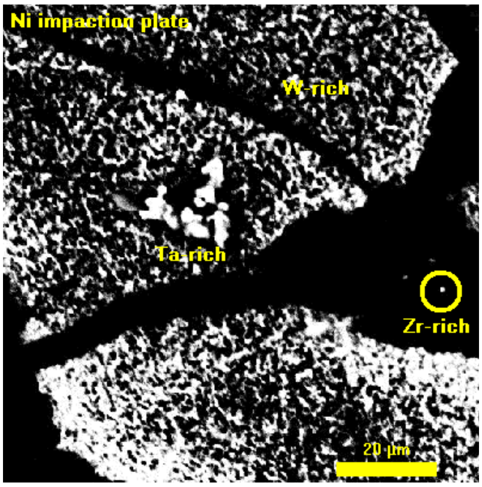

Fig. 119 Typical digital SEM image of the aerosol collected by the Ni impaction plate

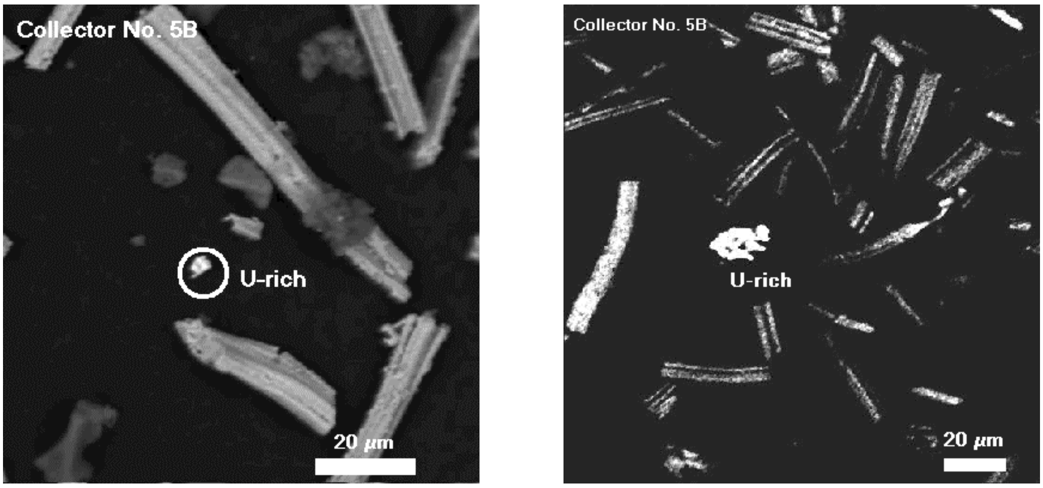

Fig. 120 U-rich particles (smaller and larger ones) detected on collector No. 5B.

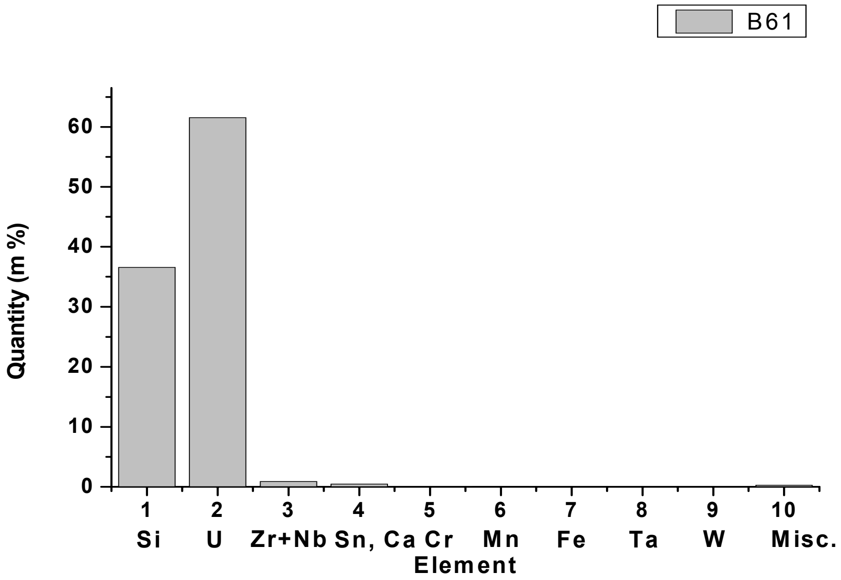

Fig. 121 Results of the standardless EDS analysis of U-rich particle settled on collector No. 6B.

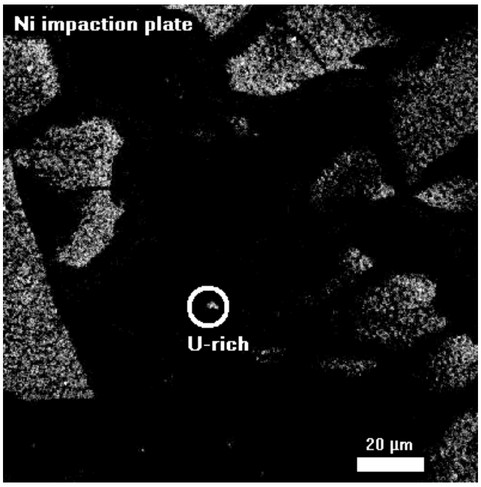

Fig. 122 Typical example for U-rich aerosol particle settled on the Ni impaction plate

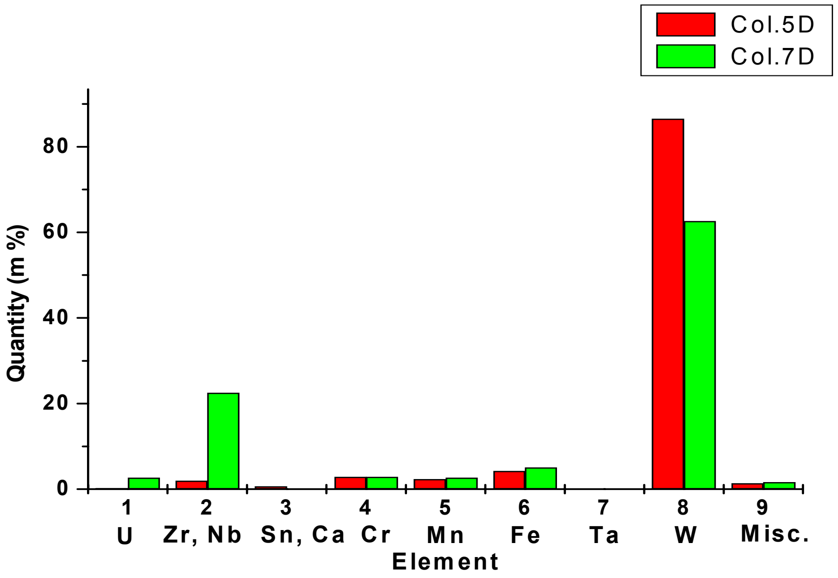

Fig. 123 Results of the standardless EDS analysis of typical W-rich aerosol particles settled on collector plates No. 5D and 7D, respectively

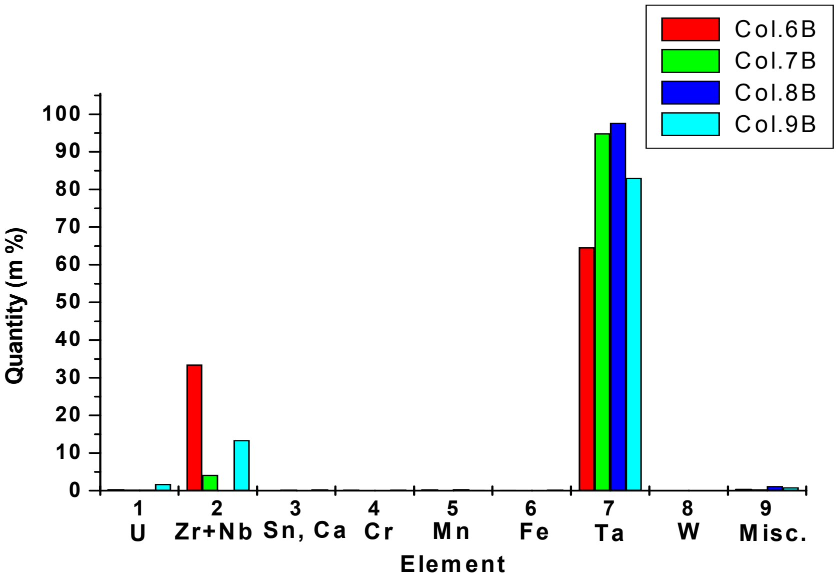

Fig. 124 Typical results of standardless EDS analysis for various aerosol particles settled on collectors No. 6B, 7B, 8B and 9B.

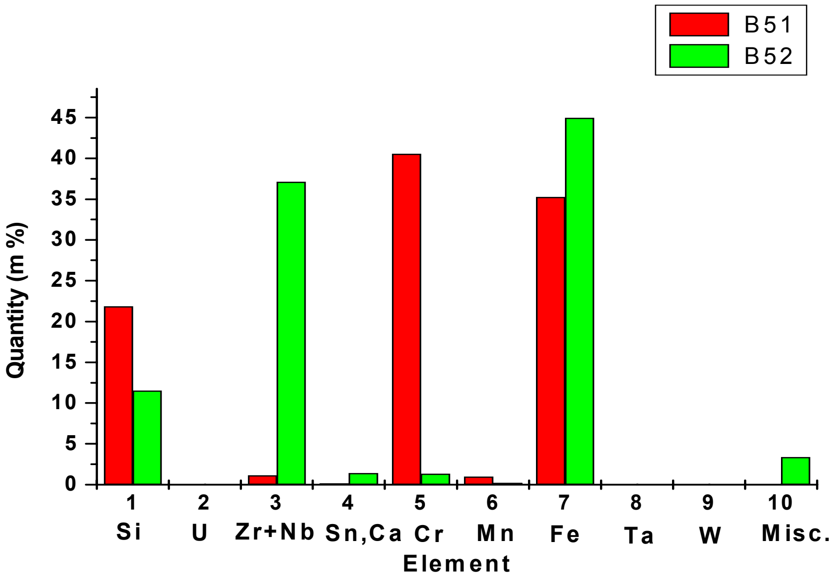

Fig. 125 Results of the standardless EDS analysis for typical Fe-Cr-Mn containing aerosol particles

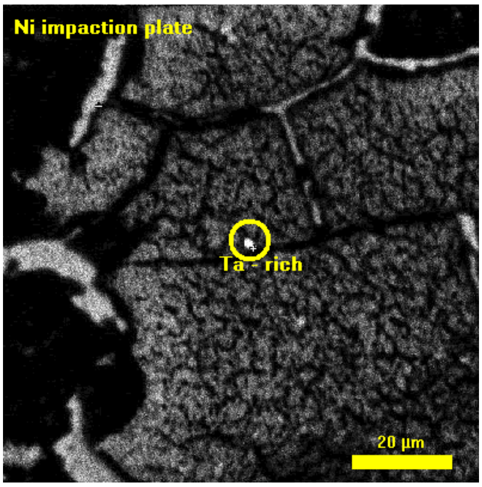

Fig. 126 Typical digital BE image taken from the Ni impaction plate showing enrichment of Ta

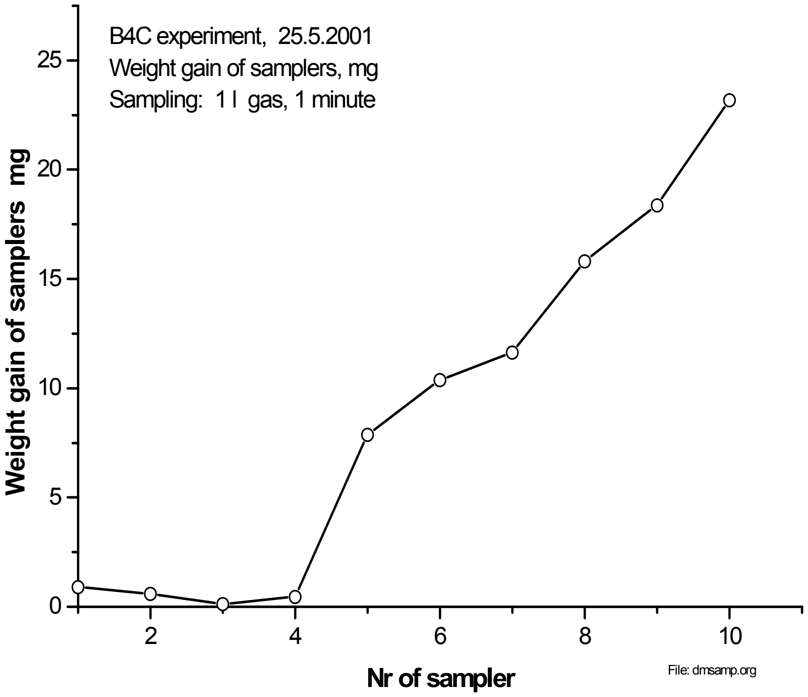

Fig. 127 Mass increase of impactors during the sampling